Towards Intelligent Tire and Self-Powered Sensing Systems

by

Hassan Askari

A thesis
presented to the University of Waterloo
in fulfillment of the
thesis requirement for the degree of
Doctor of Philosophy
in
Mechanical and Mechatronics Engineering

Waterloo, Ontario, Canada, 2019

Examining Committee Membership

The following served on the Examining Committee for this thesis. The decision of the Examining Committee is by majority vote.

External Examiner: Siamak Arzanpour
Professor, Mechatronic Systems Engineering Dept.,
Simon Fraser University

Supervisor(s): Amir Khajepour, and Mir Behrad Khamesee
Professor, Dept. of Mechanical and Mechatronics Engineering,
University of Waterloo

Internal Member: Patricia Nieva
Professor, Dept. of Mechanical and Mechatronics Engineering,
University of Waterloo

Internal Member: Grzegorz Glinka
Professor, Dept. of Mechanical and Mechatronics Engineering,
University of Waterloo

Internal-External Member: Eihab Abdel-Rahman
Professor, Dept. Systems Design Engineering,
University of Waterloo

Abstract

Tires are the interface between a vehicle and the ground providing forces and isolation to the vehicle. For vehicle safety, stability, maintenance, and performance, it is vital to estimate or measure tire forces, inflation pressure, and contact friction coefficient. Estimation methods can predict tire forces to some extent however; they fail in harsh maneuvers and are dependent on road surface conditions for which there is no robust estimation method. Measurement devices for tire forces exist for vehicle testing but at the cost of tens of thousands of dollars. Tire pressure-monitoring sensors (TPMS) are the only sensors available in newer and higher end vehicles to provide tire pressure, but there are no sensors to measure road surface condition or tire forces for production vehicles.

With the prospect of autonomous driving on roads in near future, it is paramount to make the vehicles safe on any driving and road condition. This is only possible by additional sensors to make up for the drivers cognitive and sensory system. Measuring road condition and tire forces especially in autonomous vehicles are vital in their safety, reliability, and public confidence in automated driving. Real time measurement of road condition and tire forces in buses and trucks can significantly improve the safety of road transportation system, and in miming/construction and off-road vehicles can improve performance, tire life and reduce operational costs.

In this thesis, five different types of sensors are designed, modelled, optimized and fabricated with the objective of developing an intelligent tire. In order to design these sensors, both electromagnetic generator (EMG) and triboelectric nanogenerators (TENG) are used. In the first two initial designed sensors, with the combination of EMG and TENG into a single package, two hybridized sensors are fabricated with promising potential for self-powered sensing. The potential of developed sensors are investigated for tire-condition monitoring system (TCMS). Considering the impressive properties of TENG units of the developed hybridized devices, three different flexible nanogenerators, only based on this newly developed technology, are developed for TCMS. The design, modelling, working mechanism, fabrication procedure, and experimental results of these TENG sensors are fully presented for applications in TCMS. Among these three fabricated sensors, one of them shows an excellent capability for TCMS because of its high flexibility, stable and high electrical output,and an encapsulated structure. The high flexibility of developed TENG sensor is a very appealing feature for TCMS, which cannot be found in any available commercial sensor. The fabricated TENG sensors are used for developing an intelligent tire module to be eventually used for road testing. Several laboratory and road tests are performed to study the capability of this newly developed TENG-based sensor for tire-condition monitoring system. However the development of this sensor is in its early stage, it shows a promising potential for installation into the hostile environment of tires and measuring tire-road interacting forces. A comparative studies are provided with respect to Michigan Scientific transducer to investigate the potential of this flexible nanogenerator for TCMS. It is worth mentioning that this PhD thesis presents one of the earliest works on the application of TENG-based sensor for a real-life system.

Also, the potential of commercially available thermally and mechanically durable Micro Fiber Composite (MFC) sensor is experimentally investigated for TCMS with fabricating another set of intelligent tire. Several testing scenarios are performed to examine the potential of these sensors for TCMS taking into account a simultaneous measurement from Michigan Scientific transducer. Although both flexibility and the cost of this sensor is not comparable with the fabricated TENG device, they have shown a considerable and reliable performance for online measuring of tire dynamical parameters in different testing scenarios, as they can be used for both energy harvesting and sensing application in TCMS. The extensive road testing results based on the MFC sensors provide a valuable set of data for future research in TCMS. It is experimentally shown that MFC sensor can generate up to 1.4 μW electrical power at the speed of 28 $[kph]$. This electrical output shows the high capability of this sensor for self-powered sensing application in TCMS. Results of this thesis can be used as a framework by researchers towards self-powered sensing system for real-world applications such as intelligent tires.

Acknowledgements

First and foremost, I would like to express my deepest and sincerest gratitude to my PhD supervisors, Prof. Amir Khajepour and Prof. Mir Behrad Khamesee, because of their great support and guidance for my research and education during my studies at the University of Waterloo. Their tolerance as a supervisor and never-ending energy for bringing novel technical ideas, and discussing the results of my works should be highly appreciated. Their attitudes towards developing novel scientific works have been a source of inspiration for me to work harder on my PhD research. Working with them taught me engineering vision, ethical values and professional academic skills. The valuable experience of working under their supervision would play a significant role in my future career. Without their supervision, I would have never been able to pursue my education at the University of Waterloo.

I would like to express my gratitude to my internal members of my dissertation committee, Professors G. Glinka and P. Nieva, from Mechanical Engineering Department, Professor E. Abdel-Rahman from System Design Department. Each has been a great source of input and constructive comments. I highly appreciate my external examiner, Prof. Arzanpour because of his valuable comments and ideas.

Also, I would like to express my sincere appreciation to Prof. Z.L. Wang, for his encouragement and valuable comments about my projects during his visit at the MVS-Lab and the University of Waterloo. I am also thankful to my dear friend, Zia Saadatnia, for his endless friendship and encouragement from the beginning of my undergraduate studies until the last day of my PhD. I also appreciate my friends Masoud Mousapour and Faramarz Dorani. My colleagues and friends at Waterloo have been a valuable source of encouragement, assistance, affection, and friendship. I highly appreciate my friends including Moslem Sadeghi, Ehsan Asadi, Hamed Jamshidifar, Mohammad Al Mashaqbeh, Thamir Al Dulaimi, Xiaodong Zhang, and Heng Zhang at the University of Waterloo.

I heartily appreciate my Wife Rosa for all of her encouragement, support and true love during my PhD studies. She has been really involved in every step of my PhD studies at the University of Waterloo with her emotional support and encouraging words.

Last but not least, I would like to thank my parents, Iraj and Asieh, my sister, Helena, and my uncle, Mehdi for their boundless emotional support and endless love.

Dedication

To my Wife and Parents

Table of Contents

List of Tables

List of Figures

Nomenclature

Chapter 2

α	lateral slip angle $[rad]$
θ	angular displacement $[rad]$
F_x	longitudinal force [N]
F_y	lateral force [N]
F_z	normal force [N]
k	longitudinal slip
M_z	aligning moment $[N.m]$

Chapter 3

δ	mechanical strain
ϵ	induced electromotive force (EMF)[V]
Φ	the magnetic flux $[T.m^2]$
ρ	electric charge density $[\frac{c}{m^3}]$
σ_m	mechanical stress $[\frac{N}{m^2}]$
ε	dielectric constant of the piezoelectric material
B	magnetic flux density [T]
B_r	remnant magnetic flux density $[T]$

D	electric flux density $[\frac{c}{m^3}]$
d	piezoelectric strain coefficient
E	electric field $[\frac{V}{m}]$
H	magnetic field strength $[\frac{A}{m}]$
h_{pm}	length of permanent magnet $[m]$
i	induced current $[A]$
J	current density $[\frac{A}{m^2}]$
L	length of the coil [m]
l	an infinitesimal vector element of the coils wire
L_{coil}	inductance of the coil $[H]$
n	number of turns per unit length
P	electrical power $[W]$
P_e	regenerated power of the coil $[W]$
R_{coil}	resistance of the coil $[\Omega]$
R_{ext}	resistance of external load $[\Omega]$
R_{load}	load resistance $[\Omega]$
R_{pm}	radius of permanent magnet $[m]$
t	time $[s]$
v	velocity $[\frac{m}{s}]$
V_{AC}	AC voltage $[V]$
V_{emf}	emf in $[V]$
V_{load}	load voltage $[V]$
V_{OC}	open circuit voltage [V]

Y	Young's modulus $[\frac{N}{m^2}]$
y	moving distance of the coil through the magnetic field [m]

Chapter 4

ϵ_{ri} $i = 1, 2$	relative dielectric constant
σ	surface charge density $[C.m^{-2}]$
E_{air}	electric field strength of the air $[\frac{V}{m}]$
h_o	effective thickness
h_i $i = 1, 2$	dielectric thickness $[m]$
Q	electrical charge $[C]$
S^m	area size of the metal $[m]$
x	displacement $[m]$

Chapter 6

$\hat{F_x}$	predicted value of the longitudinal force [N]
D_{cp}	length of the contact patch $[m]$
L_s	sensor length $[m]$
m	number of samples
t_0	entering time to the contact patch$[s]$
t_1	exit time from the contact patch $[s]$
t_c	period of electrical voltage generation $[s]$
V_c	velocity of vehicle $[m/s]$

Chapter 1

Introduction

1.1 Problem Statement

Tires are the most essential components in vehicles to provide safety for drivers and passengers. Indispensably, tire-condition monitoring system (TCMS), especially pressure monitoring, plays a significant role in promoting road traffic safety and reducing disastrous accidents. In fact, TCMS is installed to observe tire conditions such as tire pressure, different forces, moment and friction coefficient in order to warn the driver if there is any unsafe change in any of the measured values. Also, it plays a significant role in adaptively adjusting vehicle's stability. Installing TCMS module, specifically in recently developed smart tires, provides an accurate estimation from pressure, temperature, moment and different forces in tires. It must be highlighted that all of these parameters play an essential role in the overall multi-body dynamics of a road vehicle as well as vehicle control dynamics.

The necessity of exploiting TCMS becomes clear in preventing deflated and also flat tires. Deflated and flat tires can be a potential reason for extra fuel consumption, noise emissions, extreme tire wear, reduction in tire lifetime, escalation in CO_2 emissions and higher rolling resistance. It has been estimated that using only the pressure monitoring system in EU-15 could lead to a reduction in CO_2 emissions of 9.6 million tons per year by 2020. Owing to the importance of tire pressure monitoring sensor (TPMS) for providing safety, it has been mandatory for the vehicle manufacturers to equip all new light vehicles sold in United States with a TPMS in accordance with the U.S. Federal Regulations since September 2007. For commercially available TPMS, vehicle manufacturers supply the power for sensors inside of the tires using batteries that have a limited lifetime and power; therefore, they cannot last for the entire life of tire. Maintaining a proper tire pressure plays an important role in passenger safety owing to its substantial effect on the vehicle handling and control. Because of the direct relation of car safety to tire pressure, it is crucial to have a sustainable power source for real time monitoring of the pressure. Accordingly, it is inescapable to implement new emerging technologies in energy harvesting devices for powering tire-condition monitoring systems, and in particular, TPMS. As mentioned above, TCMS is also exploited for estimating different forces, namely longitudinal force F_x , lateral force F_y , and normal force F_z. These three forces play a key role in vehicle dynamics. For example, the longitudinal force is the most significant factor for determining the performance behavior of a vehicle. The lateral force is crucial, particularly in vehicle handling. The last one is the normal force, which is directly pertinent to vehicle road holding. As a result, having a self-powered multi-functional sensor, which is capable of measuring the above forces, provides better performance, handling and road holding for vehicles. In fact, research in this area has two main concerns. The first one is developing a reliable and durable sensor, and the second one is providing electrical power for the sensor. This leads researchers to work on new techniques to develop power harvesting devices for TCMS. Chapter 2 will provide a comprehensive review on the proposed energy harvesting and sensing mechanisms for tire-condition monitoring.

Although estimation methods currently are used to measure the tire forces, however a direct measurement of such forces will eliminate any uncertainties due to the changes in road condition, tire parameters, and etc. Current estimation methods are capable of predicting tire forces to some degree although; they malfunction in harsh maneuvers and depend on road surface conditions for which there is no solid and reliable estimation approach. Currently, tire force measurement tools exist for performance vehicles for a very expensive cost [13, 14].

As automotive industry moves towards autonomous driving on roads, enhancing vehicles' safety for any driving and road condition becomes even more important. Measuring road conditions and tire forces plays an important role in enhancing safety, reliability, and public confidence in automated driving and in applications such as mining and construction. There are three particular branches of research in the area of TCMS including estimation, sensing, and power harvesting. The main focus of this thesis is on the development of a self-contained sensing approaches and measurement strategy for TCMS based on piezoelectric, electromagnetic and triboelectric nanogenerators. Figure 1.1 depicts an intelligent tire with its basic parts, and its crucial applications and advantages. In Figure 1.1, NGs, PEGs, and EMGs refer to nanogenerators, piezoelectric generators, and electromagnetic generators, respectively.

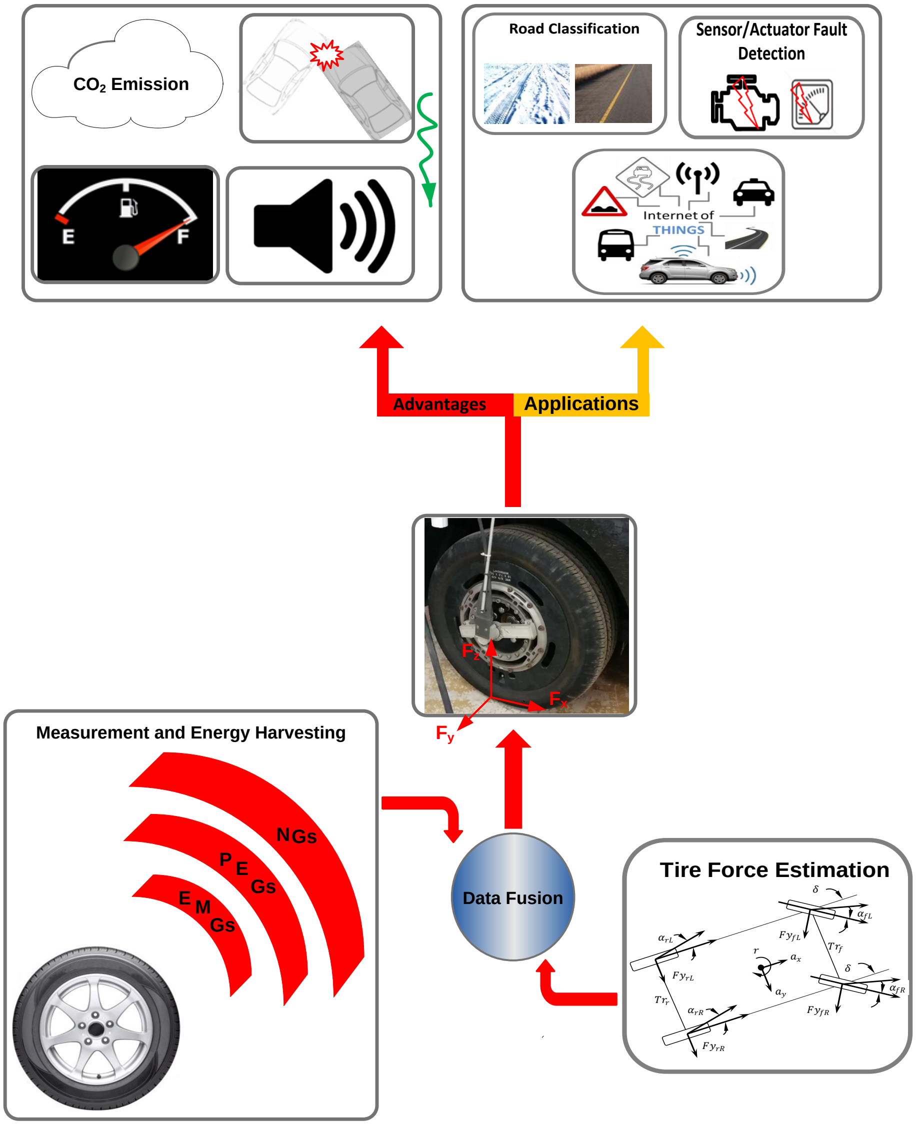

Figure 1.1: An intelligent tire: estimation, measurement, energy harvesting, data fusion, advantages and applications

Figure 1.1 shows potential technologies for reaching to intelligent tire systems, which include estimation techniques, measurement and energy harvesting approaches, and data fusion. To improve the existing technologies for TCMS, the main challenge is to find the most reliable and durable approach for measuring tire forces. To meet this objective, this research project is performed to find a potential sensing technology for online measuring of tire forces.

1.2 Research Objective

The main interest in self-contained sensory device for tire system is primarily prompted by the demand of vehicle industry to intelligent tires. In accordance with this demand, the principal objectives of this PhD work are as follows:

- Investigating the potential of different sensing and power harvesting technologies such as piezoelectricity, electromagnetism, and triboelectricity for tire-condition monitoring system
- Proposing a novel platform and strategy for sensing with application in tire-condition monitoring system
- Designing, modelling and fabricating a highly flexible, thermally and mechanical durable sensor, which is capable of working in a harsh environment, and measuring tire forces
- Experimentally studying the potential of micro fiber composite (MFC) sensor for tire-condition monitoring to select the best potential approach for this crucial application
- Developing an intelligent tire module based on the fabricated and also MFC sensors to be used for tire-condition monitoring
- Training a neural network for online prediction of tire forces based on the generated output of tire sensors, car velocity and acceleration

1.3 Contributions

In this thesis, different technologies and materials for sensing applications in tire systems are investigated considering its hostile environment with its huge acceleration, high temperature levels and limited space. Based on extensive research and experimental analysis, presented in this PhD thesis, the main contributions of this PhD thesis are as follows:

- Through an evolution process, five different types of sensors are designed, modelled, and fabricated with the aim of reaching a flexible and durable sensing system for TCMS using triboelectrification and electromagentism.
- For the first time, a set of intelligent tire module is developed based on triboelectric nanogenerator for road testing to show its capability for TCMS.
- The capability of commercially available MFC sensor is also shown under different road testing scenarios. It is presented that the MFC sensors are capable of identifying tire forces as well as power harvesting using tire contact patch deflection. This will open a new door to researchers to use the obtained experimental data of this thesis for finding a correlation between the sensor output and tire dynamical parameters.
- A neural network is trained based on the measured data from experimental tests of MFC sensors in vehicle's straight maneuvers to identify tire longitudinal forces. This is the first step towards a fully trained tire with the capability of online identification of tire forces.

Result of this PhD thesis enriches the state of the knowledge in the modelling, design, optimization, and fabrication of flexible sensors for TCMS and several other potential applications. In addition, this PhD thesis provides a comprehensives study on tire-condition monitoring systems implementing different approaches including theoretical, finite element, and experimental techniques. Indeed, the outcome of this research not only can provide useful information for researchers in tire systems, but also, it provides useful information for experts in the areas of sensor technologies, energy harvesting, and self-powered sensing. It presents all required technical background for designing novel sensors based on TENGs and EMGs, and also a robust strategy for TCMS.

1.4 Thesis Structure

This PhD thesis contains seven chapters, and its structure is as follows:

- Chapter 1 illustrates the considered problem of this thesis, the objectives, main contributions, and thesis structure.

- Chapter 2 provides a comprehensive review on the state of the art in the area of sensing and energy harvesting in tire systems. Section 2.2 reviews the potential of piezoelectric materials and the published works using these materials for sensing and energy harvesting in tires. Electromagnetic-based energy harvesters and sensors in tire systems are reviewed in Section 2.3. The potential of nanogenerators for TCMS and the developed devices based on NGs are discussed in Section 2.4. Other approaches for sensing and power harvesting in TCMS, and the prospective of the research in this area, based on the developed sensory devices, are presented in Sections 2.5 and 2.6, respectively.

- Chapter 3 is focused on design, modelling and fabrications of two first fabricated hybridized sensors for TCMS. The technical background related to the design and modelling of the proposed hybridized sensors are fully presented. Then, a conceptual discussion is provided for the possible deformation and locations of the sensors in a tire (Section 3.2). The first hybridized sensor is presented in Section 3.4 including all designs, mathematical modelling, working mechanisms, finite element modelling for both TENG and EMG components of the hybridized device. In addition, Section 3.4 includes the optimization results of the EMG component of the hybridized sensor I. In Section 3.5, all designs, mathematical modelling, working mechanisms, finite element modelling for both TENG and EMG components of the second hybridized device are presented.

- Chapter 4 presents three novel flexible TENG-based sensors for TCMS. The applications of flexible sensors in TCMS are discussed in Section 4.1. Section 4.2 describes the first designed single electrode flexible TENG-based sensor for TCMS including design, modelling and fabrication procedures. In Section 4.3, the design, working mechanisms, finite element simulations, and the fabrication procedure of an encapsulated single electrode TENG-based sensor for TCMS are presented. The working mechanisms, design, finite element simulations, and the fabrication procedure of an encapsulated double electrodes TENG-based sensor are illustrated in Section 4.4.

- Chapter 5 presents the experimental results for each of the fabricated sensors. The experimental results present the general capability of the sensors and also their potential for tire-condition monitoring.

- Chapter 6 shows the potential of the developed flexible TENG sensor for tire-condition monitoring. Data acquisition, sensor installation, and road testing are presented in this chapter. Data analysis related to the extracted measurement from the sensor in road tests are also presented in Chapter 6. The last part of the chapter shows results of the road testing and its experimental setup with MFC sensors used in the smart tire module. Furthermore, a neural network is trained for online identification of tire longitudinal force.

- Finally, conclusions and future works are presented in Chapter 7 of thesis. It provides concluding remarks based on the fabricated sensors, and road tests in accordance with both TENG and MFC sensors, and also the outstanding potential of TENGs for TCMS.

Chapter 2

Literature Review

Intelligent tires equipped with different sensors for the sake of tire-condition monitoring are highly in demand to improve vehicle control and safety. The idea of using self-powered sensing systems for TCMS is a hot topic among researchers. It is a new quest for researchers to exert wasted kinetic energy sources for energy-scavenging applications. Plenty of innovative approaches have been proposed so far to extract clean useful energy from accessible ambient sources that would be otherwise dissipated. The proposed energy harvesting techniques have the potential to be used for sustainable powering of wireless sensor nodes (WSN). Employing new methods for energy harvesting results in smaller and more efficient devices. The significance and high influence of tires in providing safety for passengers have prompted researchers to furnish advanced vehicles with a smart tire/wheel system. Implementing the smart tire/wheel system leads to increasing traffic safety [15]. In addition, it is highly significant in improving chassis/vehicle control systems, and Advanced Driver Assistance Systems (ADAS). In order to reach the above-mentioned aims, numerous sensory technologies have been proposed and implemented so far for collecting strain and deflection related data from tires [16]. A few examples are piezoelectric sensors, surface acoustic wave and ultrasonic sensors [17, 18], capacitance based strain sensors [19–21], fiber Bragg grating, resistance based strain sensors [22], segmented capacitance ring [23], and flex sensors [24]. With implementing the aforesaid sensory technologies, a fully functional smart tire would be capable of providing information about longitudinal force, lateral force, normal force [25], friction coefficient [26], inflation pressure [27], and aligning moment. Furthermore, online information about tire tread deformation with implementation of TCMS [28] can be obtained. Figure 2.1 represents a fully functional smart tire system [22].

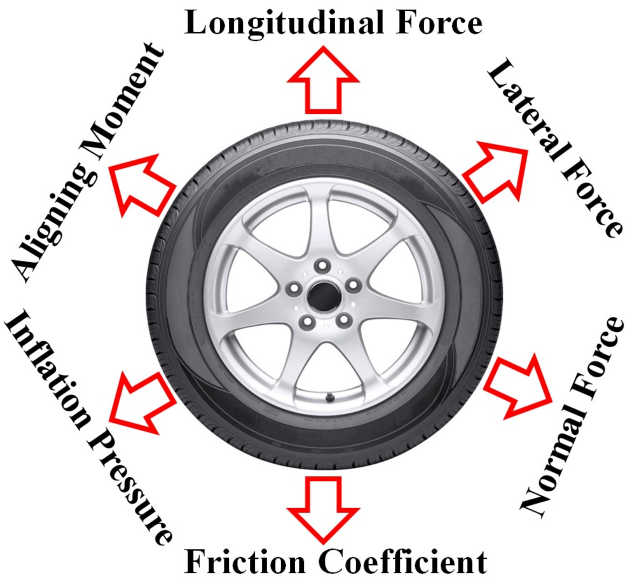

Figure 2.1: A fully functional smart tire; used with permission [1], copyright 2017 Wiley

In fact, a smart tire contains a tire-condition monitoring system (TCMS), which is capable of online extracting all the aforesaid parameters. In spite of recent developments in the reduction of power supplying of minuscule micro electromechanical systems, it is desperately needed to have power sources for the autonomous and continuous operation of such tiny and low-energy consumption electronic devices [29].

The fusion of sensory systems and energy harvesters results in improvements in our daily life, and leads to emerging new devices. There are plenty of different energy sources in our environment like thermal, light, acoustical noises, and also kinetic. Among the above-mentioned available sources, the kinetic type is ubiquitous, which makes it as a potent option to provide power for self-powered smart systems, especially sensors [30–32]. This chapter provides information about the principal techniques for energy harvesting and sensing in tires. Section 2.1 discusses the importance of the self-powered sensing system for tire condition monitoring. Section 2.2 presents the published articles in the area of TCMS using piezoelectric mechanisms. The focus of Section 2.3 is on electromagnetism and its applications in TCMS. Section 2.4 reviews the applications of nanogenerators in the development of TCMS. The last section of this chapter presents other methods, which have been already implemented by researchers for TCMS.

2.1 Self-Powered Sensing System for Tire-Condition Monitoring

Developing a self-powered sensory system for tire-condition monitoring system is an important step towards autonomous driving. It is highly needed to design, model, optimize, and fabricate a self-powered sensing system, which is capable of working in the harsh environment of a tire, and can measure the important tire dynamical parameters. The proposed sensor must be both thermally and mechanically durable, and should have the potential to provide its power through harvesting wasted kinetic energy in a tire. In fact, powering component is one of the main parts of TCMS. Accordingly, providing a sustainable power source for TCMS is necessary. A number of researchers have focused on developing energy harvesting mechanism for TCMS. A comprehensive review in Chapter 2 is provided on the efforts done by researchers to develop power harvesting component in tires. Their principal objective was to power the sensors inside the tire or promote the current sensory device to the category of self-powered sensing system for tire-condition monitoring. This will lead to having a fully functional sensory device, which is capable of extracting tire dynamical parameters as presented in Figure 2.2. These parameters include longitudinal force F_x, lateral force F_y, normal force F_z, and aligning moment M_z.

In fact, measuring tire-road forces plays a vital role in the state of the art developments in the field of vehicle state estimation and control. They are incorporated into the lateral dynamics to estimate vehicle states and analyze the vehicle stability on different roads. Tire curves are represented by three regions including linear, transient, and nonlinear defined by road friction coefficient, normal forces, and cornering stiffness. The generated lateral and longitudinal forces during cornering, acceleration, and brake scenarios are realized to depend on the road surface friction, slip ratio/angle, and vertical forces. Developing a sensor, which is capable of finding tire curves would lead to a significant step for reaching to an intelligent tire, which is highly needed to address the challenges in autonomous driving.

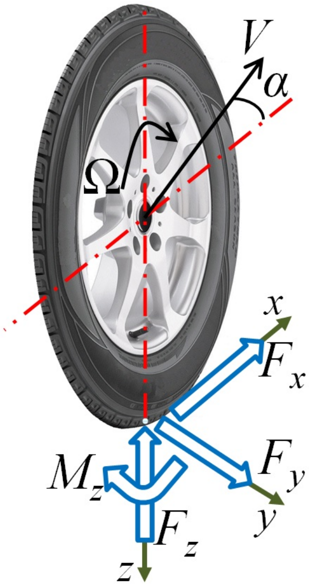

Figure 2.2: Tire with its dynamical parameters

2.2 Piezoelectricity

The presence of an electric field engenders physical deformation in piezoelectric materials, or on the other hand, generates an electrical charge when mechanically deformed. In fact, the spontaneous separation of charge within certain crystal structures under the right conditions leads to the generation of an electric dipole [33]. The most significant advantage of piezoelectricity is the direct conversion of mechanical strain, stress, or deformation into electrical charge and vice versa [34]. This superior characteristics of piezoelectric materials have been fascinating for researchers to utilize them in energy harvesting devices and sensors [33, 35, 36]. They have been exploited to scavenge energy for number of systems in bio-engineering, the detection of pollutants, programmable paper, vibration detection and vehicle monitoring. In addition, the generated voltage by the piezoelectric-based device not only can be used for energy harvesting applications, but also, it can be utilized for sensing in different systems including tires [37–41].

Recently, piezoelectric materials have been considered by a number of companies including Piezotag, Siemens, and Michelin Research et Technique SA to develop energy harvesters and sensing instruments. A few teams have dedicated research efforts on the development of piezoelectric generators for TCMS. In a novel research work, Marian Keck developed an energy harvester using piezoelectric materials to provide power for embedded sensors in a tire. The fabricated power harvesting device is capable of generating average power of 40 μW over 30–180 km/h velocity range [42]. The energy harvesting device contains a beam with support on both ends, and also nonlinear spring stiffness. In another work, Zheng et al. proposed a piezoelectric energy harvesting device, which should be installed on the wheel up-side-down, and it works in compression mode. The radial vibrations of the air-spaced cantilever were used to generate the peak power at the resonant frequency. The fabricated device can scavenge 47 μW power at approximately 80 km/h. The only shortcoming of their energy harvester is its size, which made its practical application impossible for TCMS [43]. Tang et al. designed piezoelectric cantilevers excited by magnetic repulsive force, and effectively generated an average power of 10 μW, in the frequency range of 10-22 Hz. The harvester is mounted on the rim inside the tire cavity [40]. Gu and Livermore proposed a self-tuning power harvesting mechanism, which encompasses a pendulum-driven system. With implementing tangential vibrations, the device is capable of generating a maximum power density about 30.83 $\frac{\mu W}{cm^3}$ [44, 45]. Their energy harvesting device was designed for a tire with a 572 mm outer diameter. The speed range of considered tires spans 25 to 65 mph. The considered speed range corresponds to a rotational frequency range from 6.2 Hz to 16.2 Hz. Figure 2.3 depicts the self-tuning energy harvester [2].

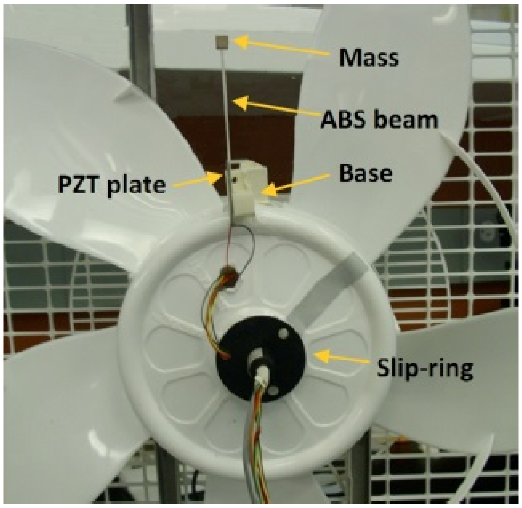

Figure 2.3: A harvester prototype mounted on an electrical fan; used with permission [2], copyright 2010 AIP

A piezoelectric bender generator, which directly harvests energy exerted by the tire speed, was proposed by Pinna in 2010. The generator was attached to the tire wall from the outside in the tangential direction at 16 cm distance from the wheel centre. It has been represented that their energy harvesting device is capable of generating power around 2.99 μWat 80 Km/h velocity [46].

Roundy and Tola developed a power harvesting system, which uses the earth's gravitational field [47]. In order to have a better operational bandwidth in their designed system, they combined the unique dynamics of an offset pendulum with a nonlinear bistable restoring spring. The ball inside of the harvester rolls back and forth in the curved track between the two end stops. As it passes through the center of the track, the piezoelectric beams are excited. The device can generate 10 μW power at 10 kph, which is more than the required power for transmitting the signal in each minute [47].

The feasibility of implementing an inertial vibrating energy harvester unit to provide electrical power for the sensor module inside the tire was investigated by Singh et al. [48]. They showed that the high acceleration levels associated with a tire result in certain issues in designing a harvester system for tires. These issues include broad-band operation, low weight, and small volume. Therefore, they designed a piezoelectric bimorph transducer considering all of these design issues. Also, in order to optimize the frequency band of operation, they developed a novel artificial neural network (ANN) based feedback loop control [48].

A novel ring piezoelectric harvester excited by magnetic forces was developed by Xie et al. for power harvesting in tires. The harvester includes an outer ring stator and an inner ring rotor. The stator ring is fabricated by a series of discrete piezoelectric patches with a rectangular shape surface mounted by magnetic ring slabs with the same size. Figure 2.4 shows the schematic of the proposed energy harvester. The proposed ring can generate up to $5274.8W$ power with considering $l = 0.4\ m$, $w = 0.005\ m$, $t_m = t_p = 0.01\ m$, $r_1 = 0.5\ m$, $r_2 = 0.499\ m$, and $B_r = 1.48\ T$ [3]. All of the aforesaid parameters are defined in Figure 2.4. Following this work, Xie and Wang proposed a mathematical model for piezoelectric ring energy harvesting technology in a tire. The model was developed based on an iteration method to obtain the energy harvested from excitation of tires by rough roads. In their conceptual design, they supposed a piezoelectric ring harvester, which consists of a series of discrete PZT4 patches in a square shape. The results of the paper show that the implementation of this ring in tires not only enables powering tire sensors, but also, it can power other appliances in vehicles as the RMS of the power for each ring can reach 42.08 W [49].

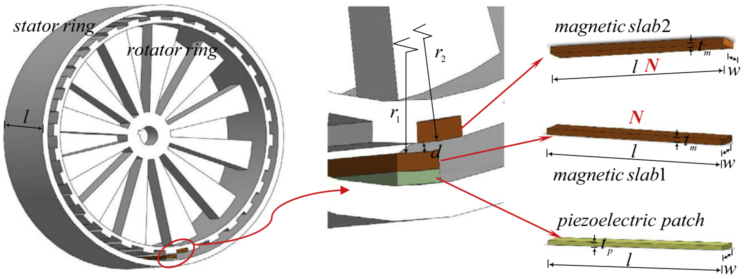

Figure 2.4: Schematic diagram and geometries of the piezoelectric energy harvester; used with permission [3], copyright 2014 Elsevier

Makki and Pop-Iliev designed and developed a functional automotive TPMS using a very low cost and highly flexible piezoceramic (PZT) bender elements. Based on the results of their research, the fabricated TPMS can be implemented as a battery-less and wireless device inside a tire [50].

Lee and Choi [51] used piezoelectric materials to design a power harvesting patch, which can generate 34.5 μJ. The fabricated power harvesting patch uses the strain energy of the deformation in a tire to generate electrical voltage. They also proposed an efficient method to enhance the generation efficiency of piezoelectric patch. The dimension of the fabricated piezoelectric patch is ($60 \times 10 \times 0.3\ mm^3$).

Eshghi et al. designed an optimized piezoelectric energy harvester, which is capable of powering TPMS under uncertainty and speed variability. A piezoelectric energy harvester was tested for an automotive wheel using stochastic resonance. Their results demonstrate that stochastic resonance can be used to optimize the performance of the power harvester with a sustainable power density of 0.76 $\frac{\mu W}{cm^3}$ [52].

In Mechatronics Vehicle System laboratory (MVS-lab), piezoelectric sensors have been used for finding tire forces. Using the finite element analysis, the best location for attaching the piezoelectric sensors was found, and then, with employing a trained neural network, different forces in tires have been obtained [22]. Although, the electrical output of the piezoelectric sensor was enough for both power harvesting and sensing, but it was realized that it cannot be used for real tire system due to its low thermal and mechanical durability [53]. An instrumented system for smart tire application was fabricated in MVS-lab using piezoelectric sensors [53]. To develop the smart tire sensory system, four sensors were located in different places of the smart tire. Two of them were attached to the sidewalls of tire, and the other sensors were located at the tread center-line. This pattern of sensors attachment provides the required measurement for different forces in a tire.

A scrutiny of literature about the piezoelectric energy harvesting and sensing devices in TCMS indicates that there are a few drawbacks and limitations in their designs:

a) In most cases, it is essential to design a harvester, which is capable of tuning the frequency.

b) In the case of utilizing beam-mass model, the developed devices must have an overload protection.

c) Generally, the considered resonant frequency for the different developed piezoelectric harvesting devices is not realistic.

d) The piezoelectric ceramics commonly used in energy harvesting devices are brittle.

2.3 Electromagnetism

The second practical and principal approach for energy harvesting and sensing performs based on the electromagnetic mechanism [54, 55]. Electromagnetic transducers typically work based on the relative motion of an electrical conductor in a magnetic field or time-varying magnetic field in the presence of a stationary conductor. In most cases, the conductor is wound in a coil to make an inductor [56]. In fact, the relative motion between the coil and magnetic field causes a current to flow in the coil [57], [58], [59]. Electromagnetic transducers have two interesting features. First, there is no need for having a separate voltage source to start the energy conversion process as with the electrostatic type. Second, no mechanical contact is needed in design elements of the device.

Owing to low-cost of the electromagnetic approach, it has been considered as a viable platform for TCMS [60]. There are two different types of electromagnetic power harvesting in tires including inertial electromagnetic and relative displacement electromagnetic transducers. The first type of electromagnetic transducers is utilized to generate electrical output for different applications such as TCMS. As an example of inertial devices, an energy harvesting design developed by Lee and Kim can be highlighted, which contains coil strap attached to the circumferential face of a rim, and a permanent magnet located on the brake caliper system [61]. The fabricated device harvests rotational energy and alters it into electricity utilizing electromagnetic induction via the coil strap located inside the wheel rim [61]. Inertial harvesters that are installed in the inner side of the tire have also been illustrated by Tornincasa et al. [62]. It is suggested that the inertial harvesting device to be mounted on the inner liner of a tire. The harvester operates based on the magnetic levitation. Because of tire and road interaction, the permanent magnet would have relative motion with respect to the coil. A novel design was proposed by Wang et al. to harvest power from a rotating wheel. The fabricated power harvesting device includes two springs along with a coil, magnet, and an electrical circuit [4]. The centrifugal force, and the push-pull forces by two springs are the main dynamical parameters of their proposed energy harvester. An energy harvesting device embedded in a rotating wheel is shown in Figure 2.5 [4]. The proposed energy harvesting device can generate 30 to 4200 μW power for a range of speed between 200 to 900 rpm. Their work also reports a nonlinear mathematical model for the developed fabricated energy harvesting device. The obtained nonlinear differential equation of their system has a relativistic form [63], and its approximated equation can be presented by the Duffing equation [64–66]. Considering the tangential accelerations faced by a rolling wheel, the fabricated power harvester can generate an output power of 0.4 mW for a resistance load of a 100 Ω at 15g peak-to-peak amplitude [5, 67]. Figure 2.6 represents an assembled FR4 energy scavenger design with spacer and components of a scavenger design. The implemented magnet in the fabricated energy harvester has a radius of 10 mm and a height of 2 mm.

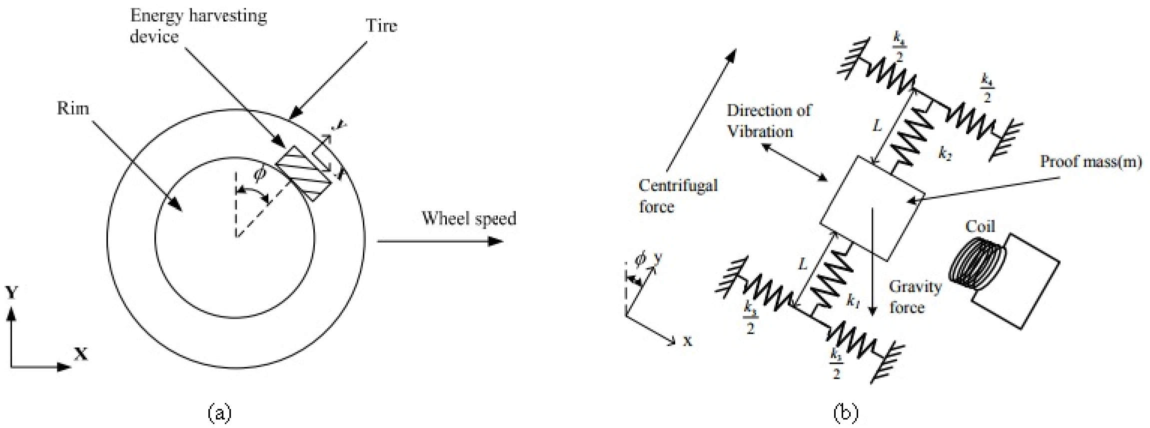

Figure 2.5: Nonlinear suspended energy harvester (NSEH) used in a wheel, (a) schematic representation of a rolling wheel, (b) schematic of the NSEH ; used with permission [4], copyright 2015 MDPI

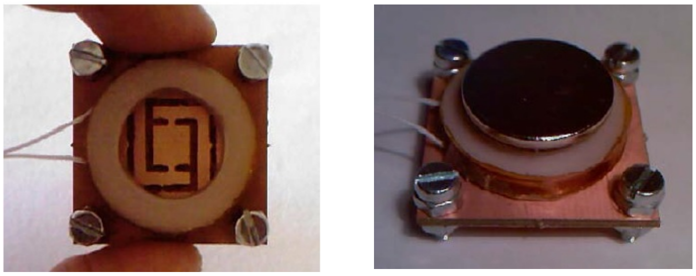

(a) (b)

Figure 2.6: (a) Assembled FR4 energy scavenger design with spacer (b) assembled structure with an oversized magnet; used with permission [5], copyright 2009 Elsevier

Oscillations induced by Karman Vortex street in the flow channel can be effectively used for energy scavenging. Based on this idea, Wang et al. designed an electromagnetic power harvester, which utilizes the pressure oscillations because of the Karman vortex street to generate electrical voltage. This results in a periodical relative motion between the magnet and coil, and therefore inducing electrical current [6]. Figure 2.7 represents their developed model. The volume of proposed energy harvesting device is 37.9 cm^3, and it can generate an instantaneous power of 1.77 μW at the pressure fluctuation frequency of 62 Hz and a pressure amplitude of 0.3 kPa [6].

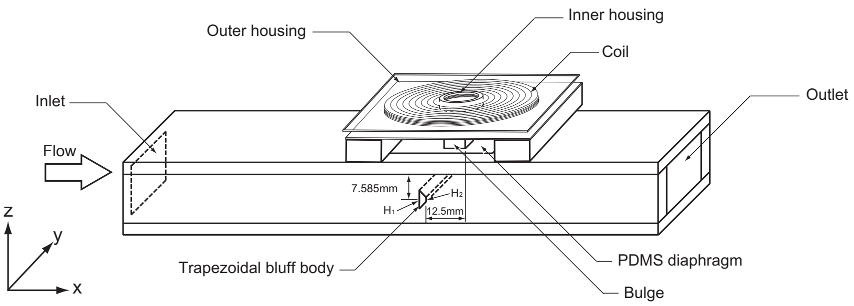

Figure 2.7: (a) An assembled energy harvester; reproduced with permission [6], copyright 2012 Elsevier

Tang and Zuo derives the closed-form of output power of dual-mass harvesters considering random excitation such as displacement, velocity and acceleration. Then, they compared the results with the performance of the single-mass configuration. With developing single and dual-mass vibration harvesters, they presented two different applications for them including: large-scale vibration energy harvesting from the regenerative suspensions of vehicles, and the regenerative TMDs of tall buildings [68]. Hybrid piezoelectric and electromagnetic energy harvesting from random vibrations have been developed by Li et al. [7], who proposed a hybrid energy harvester integrated with piezoelectric and electromagnetic conversion mechanisms, as shown in Figure 2.8. Their paper reports a comprehensive analytical and experimental results based on the proposed hybrid energy harvesting device considering random vibrations. Dimension of the piezoelectric layer of their device is $10 \times 8 \times 2\ mm^3$. The electromagnetic component of the energy harvester consists of a radial magnet with radius and thickness of 15 and 40 mm, respectively. The designed coil for the energy harvester has a diameter of 15 mm with 360 number of turns [7]. Wang et al. designed a well-weighted pendulum to harvest energy from a rotating wheel using electromagnetic induction technique. The fabricated device includes a pendulum and one or more weights, and it is capable of converting kinetic energy into electricity using electromagnetic approach. The proposed device can generate several miliwatts, which is enough for powering sensors inside a tire [69]. A similar design can be found in ref. [70] in which Wang et al. proposed a weighted pendulum-type electromagnetic generator for harvesting energy from a rotating wheel. Results of their paper illustrate that the fabricated energy harvester is capable of generating the electrical power of 200–300 μW at about 200–400 r/min [70].

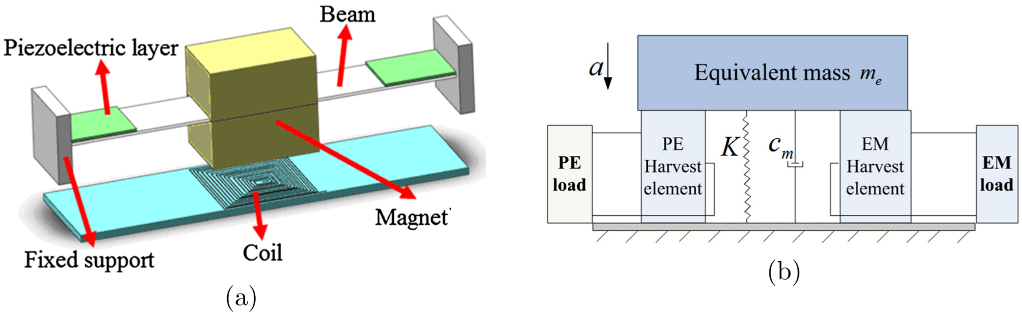

Figure 2.8: (a) Designed hybrid PE and EM energy harvester (b) SDOF model of hybrid PE and EM energy harvester; used with permission [7], copyright 2015 Springer

After a broad survey about the use of electromagnetic transducers in TCMS and designing two types of EMG-based device for this application, it is found that this mechanism is not suitable for this application, as any design based on this technique results in a bulky system. This leads to a high centrifugal force in a tire, which can have negative effects on tire dynamics. In addition, it is difficult to have a flexible system using electromagnetic technique.

2.4 Nano Generators

Since their discovery in 2006 [71], nanogenerators [72] have fascinated researchers to use them in different applications including wave [73–77] and wind energy harvesting [78–80], traffic monitoring [81], harsh environments such as turbines and tires [1], wearable electronics and also portable devices [82–86]. Generally, a nanogenerator can convert mechanical/thermal energy as generated by a tiny physical variation, into electricity. There are three main categories of nanogenerators including piezoelectric [87,88], triboelectric [89–91], and pyroelectric [92, 93]. The piezoelectric and triboelectric nanogenerators are used for converting wasted kinetic energy into electricity [86, 89, 94–99], and pyroelectric nanogenerators [100] can scavenge thermal energy from a time-dependent temperature fluctuation.

The focus of this part of the chapter is on the recent progress in tire-condition monitoring using both piezoelectric and triboelectric nanogenerators. One of the pioneering works in this area is a paper by Hu et al. in which they used piezoelectric nanogenerators for self-powered sensing in a tire. When a bending load is applied to the fabricated piezoelectric nanogenerator, a transient flow of electrons is generated across an external electrical load [8]. In accordance with the working area of the device, a maximum power output density of 70 $\frac{\mu W}{cm^3}$ was obtained. They reported that the fabricated NGs can generate an output voltage about 1.5 V and output current around 25 nA with a travel distance of 12 mm and an acceleration of 30 $\frac{m}{s^2}$. Also, the effective working area of the NGs is about 1.5 $cm \times 0.5$ cm [8]. Figure 2.9 represents the shape change of the tire in the contact patch, a sketch of the nano-generator, simulating the tire's deformation, and the location of the nano-generator in the tire [8].

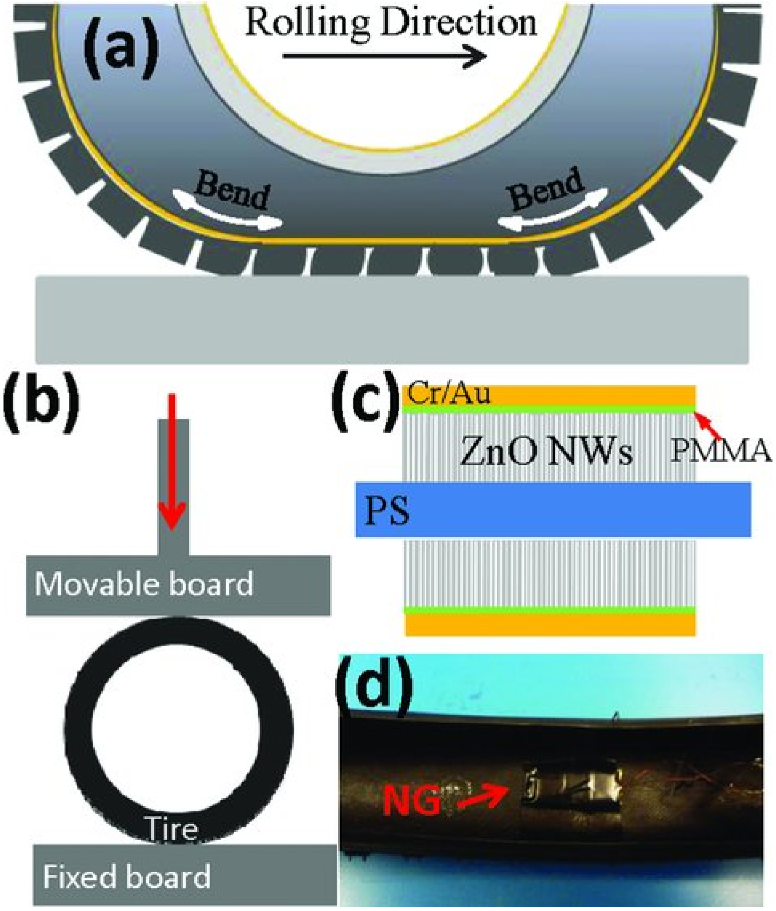

Figure 2.9: a) Shape change of the tire in the contact patch, d) simulating the tire's deformation, c) a sketch of the nano-generator and d) the location of the nano-generator in tire; used with permission [8], copyright 2011 Wiley

Another earliest attempt of the implementation of nanogenerators in a tire system, has been presented in a paper published by Mao et al. [9]. For the first time, they utilized single-electrode triboelectric nanogenerator for scavenging friction energy from rolling tires. With design and implementation of a PDMS S-TENG on a rubber wheel, they provided a systematical analysis on the potential of triboelectric nanogenerators in tires. Results of their work show that the fabricated device is capable of generating maximum instantaneous power of 1.79 mW at a load resistance of 10 $M\Omega$. Figure 2.10 schematically represents their TENG self-powered device for tire systems [9]. The experimental setup includes 6 PDMS S-TENGs (1.5 × 3.5 $cm^2 each$), which were located on the tire surface of a toy car. They showed that the highest efficiency is 10.4 % when it is shunted to 10 $M\Omega$ load resistance [9].

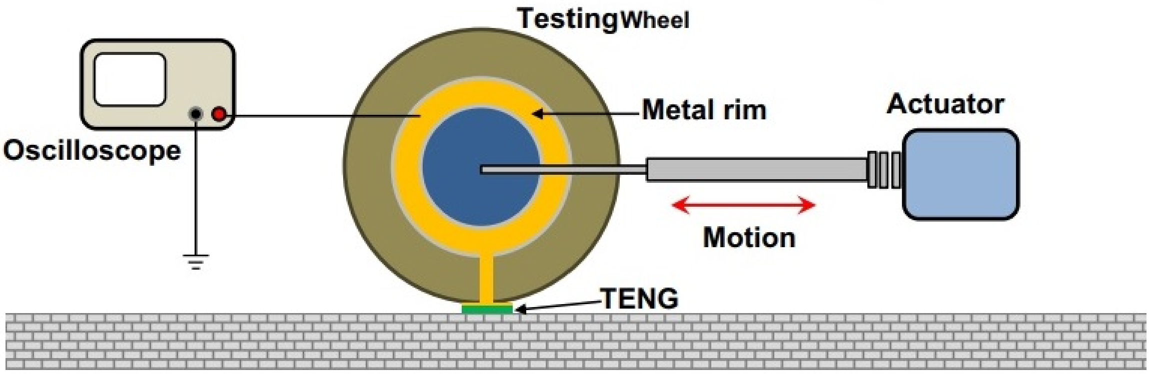

Figure 2.10: Schematic setup for characterizing the friction energy scavenging ability of the S-TENG from a rolling wheel ; used with permission [9], copyright 2015 Elsevier

Chen et al. proposed a fully packaged hybridized nanogenerator to scavenge rotation energy. The proposed device is a cylinder-like fully-packaged hybrid nanogenerator, which can scavenge vertical rotation energy. It implements a magnet rod to trigger the triboelectric nanogenerator (TENG). The hybridized generator includes eight TENG units, which have been uniformly located on the inner surface of an acrylic cylinder with dimension of $200 \times 48 \times 2\ mm^3$. The magnetic component of the device operates based on electromagnetic concepts, and it is triggered by coupling magnet rod with copper coils [10]. The magnet rod has a diameter of 30 mm and length of 42 mm, and it is used as a rolling trigger for TENG unit, and magnetic source for EMG unit of the hybridized device. The copper coil of the EMG unit has 1500 laps, and its wire's diameter is 0.015 mm. Figure 2.11 schematically depicts the designed hybridized generator, and an installed device in an automobile tire.

(a) (b)

Figure 2.11: (a) Schematic diagram of the designed hybridized generator (b) schematic of the WSN charged by the proposed nanogenerator used in a tire; used with permission [10], Copyright 2017 Elsevier

Recently, Qian et al. [11] developed a new type of self-powered magnetically tribeoelctric-based sensor for tire pressure monitoring system. The fabricated TENG based self-powered sensor is located on the wheel hub, and will periodically be actuated by the magnet mounted on the brake calliper. They showed that the fabricated self-powered sensor can generate 22.3 mW with a load of 3 $M\Omega$ under a constant magnetic field strength of 0.2 T at the rotation speed of 100 rpm. Figure 2.12 represent the fabricated self-powered sensor developed for TPMS by Qian et al.

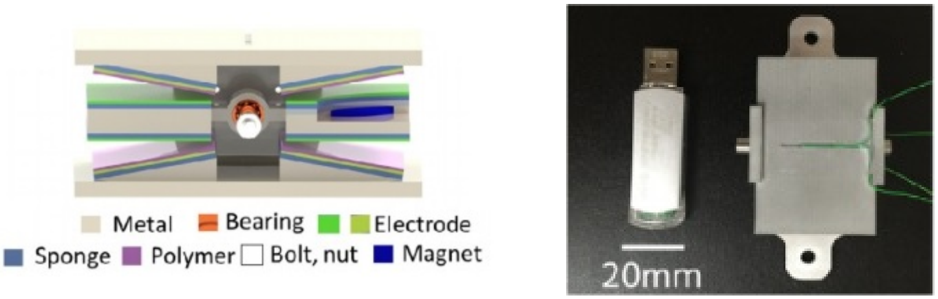

(a) (b)

Figure 2.12: (a) Three-dimensional structure of a magnetic-driven rotating triboelectric nanogenerator (b) an optical image of fabricated V-TENG device (compared with a commercial USB memory) ; used with permission [11], copyright 2018 Elsevier

2.5 Other Approaches

The above-mentioned approaches are in fact the principal methods for energy harvesting and sensing in tires. There are a few other approaches, which have been used by researchers to develop a sensing or energy harvesting system for tires. These approaches include surface acoustic wave (SAW), electrostatic, piezoresistive, and optical fiber sensing. Table 2.1 illustrates these approaches for TCMS.

Table 2.1: Other techniques for sensing and energy harvesting in tires

Technique	**Illustration-Example**
Surface Acoustic Wave (SAW)	SAW elements have been used in TPMS by Stack. SAW will re-transmit a particular RF frequency, in response to the pressure and temperature inside the tire. In addition, there is a central module in TPMS of each tire, which interrogates each wheel sensor by transmitting RF signal [17].
Electrostatic	**Example 1**: a microscale electret-based energy harvester for TPMS systems was developed by Westby and Halvorsen. It is capable of generating 4.5 μW power in the speed of 50 km/h, which is enough for TPMS [101]. **Example 2**:Lhndorf et al. developed a MEMS-based electrostatic vibration power harvesters, which can generate up to 10 μW electrical power for a TPMS .
Piezoresistive Sensors	**Example**: a flexible piezoresistive pressure sensor for measuring force magnitude and location was proposed by Emon and Choi [102].
Optical fiber sensors	**Example**: Coppo et al. have used optical fiber sensors to measure the internal tire strain during the tire rolling in real operating conditions. They have used the measured data to identify the dynamics of contact patch [103].

2.6 General View and Perspective

Force calculation at each corner (tire) based on a tire model requires road friction information and accurate tire parameters. Thereby, even accurate slip ratio/angle information from a high precision GPS does not result in forces at each tire. Estimation of longitudinal, lateral, and vertical tire forces is therefore required whenever affordable and practical measurement solution is not available. Tire force estimation independent from the road friction condition is classified on the basis of wheel dynamics and planar kinetics into the linear, nonlinear, sliding mode, Kalman-based, and unknown input observers as discussed and summarized in Table 2.2. Road friction estimation is also required for advanced vehicle active safety systems and falls into two main categories: *i)* estimation in the linear and low-excitation region (slip-slope) and *ii)* estimation around saturation area. These two main categories utilize Kalman-based, RLS-based, and linear/nonlinear methods to estimate road friction conditions [104]. Connectivity in inter-and intra-vehicular networks provide information such as nearby sudden braking events, road conditions, and road topographic data. Using this approach, a distributed diagnosis method robust to disturbances, and communication failure could be devised. Based on the comprehensive study on this topic, it can be concluded that additional sensory information (such as steering torque, TCMS, and sound/vision-based systems) and data provided by connectivity from IoT (infrastructure and inter-vehicular networks) are required to enhance the reliability of the tire force and road friction estimation, and have high potential to be used in all production vehicles in near future.

Table 2.2: Tire force estimation and tire-road friction identification

Type	**Methodology**	**Illustration/References**
Tire force estimation	Linear observers	Switching: [105]
		Steering torque Meas.: [106, 107]
	RLS-based observers	[108, 109]
	Sliding mode observers	[110]
	Nonlinear observers	[111–113]
	Unknown input observers	[114, 115]
	Kalman-based estimation	Random-walk KF: [116]
		UKF on wheel/vehicle dynamics: [**?**, 117]
		KF and EKF: [118, 119]
Road friction estimation	Nonlinear observers	[120–122]
	Unknown input observers	[123]
	Sliding mode observers [124]	
	Linear observers	[111, 125–128]
	RLS-based Est.:	[129–135]
	Steering torque Meas.	[136, 137]
	Kalman-based estimation	Extended Kalman filter: [138]
		EKFBucy and Bayesian hypothesis: [139]

In accordance with the approaches discussed in previous sections, there are four main subcategories of energy harvesting and sensing devices in tires, which have been developed so far by researchers in this area. The following table represents four subcategories of the developed devices in TCMS. In accordance with these four subcategories, plenty of devices have been fabricated for sensing and energy harvesting in tires.

Table 2.3: Categories of developed self-powered devices

Technique	**Illustration**
Relative motion devices	**Example**: A magnetic harvester which is mounted on a rim and it rotates around a stationary coil which is installed on the brake caliper [61].
Strain-driven devices	**Example**: Employ the longitudinal strain of a tire when it deforms in its contact patch [140–142].
Fluid flow devices	**Example**: Pressure fluctuations and air flow inside the tire cavity [143].
Inertial devices	**Example**: Using the concept of time varying acceleration of different points on a rolling tire [144].

Based on the presented comprehensive review on tire-condition monitoring, it is concluded that nanogenerators have a high potential to provide a reliable solution for this application in comparison with other techniques. As it has been discussed before, nanogenerators can be fabricated based on a highly flexible and thermally durable polymeric materials. These two features make them an excellent candidate for TCMS. Furthermore, NGs have a higher power density and also open circuit voltage comparing with other techniques for energy harvesting and sensing. These two features of NGs accentuate their potential for implementation in an inaccessible and harsh environment of a tire. It is expected that NGs attract attention of both academic and industrial researchers to use them for TCMS. In fact, due to their high durability, flexibility and electrical output of NGs, they are an ideal candidate for implementation in tires. Figure 2.13 illustrate the evolution of intelligent tire and the prediction for future TCMS technology. The expectation is that the challenges related to commercialization of the smart tires will be addressed using nanogenerators, flexible materials, estimation and data fusion techniques. The challenges related to mechanical and thermal durability can be solved by choosing the right materials as well as a coupling of the operation mode of the nanogenerator. Based on the existing data, TENG-based sensors functions well at temperature between -50 to 200 $^{\circ}C$ [145]. The decaying of triboelectric effect at high temperature is due to the electron thermionic emission effect [146]. Another research direction is in correlating the sensor data to tire states and tire contact patch forces, which can be solved by comprehensively measuring and simulating the tire operation conditions. Extensive research is necessary to address these issues so that the nanogenerator can be integrated into future tires. This PhD thesis opens a new door to researchers in this area to have a detailed information about the applications of NGs in harsh environments such as tire. This will lead to having fully functional smart tires in all production vehicles in near future.

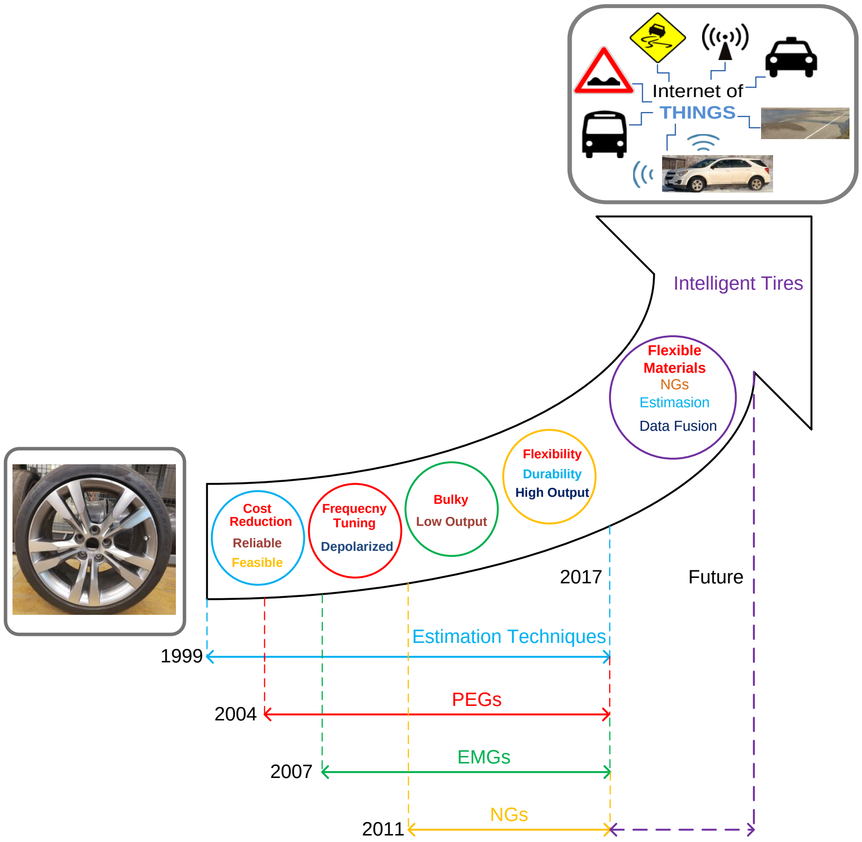

Figure 2.13: Evolution of intelligent tire and the prediction for future TCMS technology

In addition, this PhD thesis will be a comprehensive source for researchers in the area of sensing and energy harvesting as it presents technical and experimental information related to piezoelectric, electromagnetic and tribolectric generators.

2.7 Sensor Design Criteria for Tire System

Based on the literature review and tire conditions, the developed sensing system should be able to operate in a wide temperature range (-30 to 130 ^oC). In addition, in order to have a self-powered system, it is needed to generate about 10 μW. The generated power is used for powering the wireless sensor node within the tire for processing and transmitting the signal to the desired location. Furthermore, the sensor should last for the entire life span of a tire. The tire forces can exceed up to 10-11 kN in sedan type cars.

Chapter 3

Hybridized Electromagentic-Triboelectric Generator

In this chapter, two different sensory devices are introduced with the potential of utilization in tire systems. In Section 3.1, the main technologies and technical concepts used in this thesis, are discussed for developing the sensors. In Section 3.2 of this chapter, it is described how the designed sensors are implemented inside the tire. The principal concept behind the designed systems are also discussed to show how the tire deformation in its contact patch can be used for electrical voltage generation in the hybridized sensors. As this chapter discusses two novel types of hybridized generators, the main advantages of hybridization using EMG and TENG technologies are also illustrated in Section 3.3.

The first design is a tube-based flexible device, which uses both electromagnetism and triboelectricty as its mechanisms of power generation. In Section 3.4, the structure, design, modelling,and working mechanism of the tube-based hybridized device are represented. The second hybridized device also operates based on both electromagnetic and triboelectric concepts. The device has a switch shape, and it is sensitive to a very small amplitude of oscillation. Section 3.5 presents the structure, design, modelling, and working mechanism of the switch-based hybridized generator.

3.1 Sensing and Energy Harvesting Mechanisms

As stated in Section 1.1, the main objective is to find a potential sensing technology to reach an intelligent tire system, which is capable of providing online information about tire dynamical parameters such as forces. Herein, different potential technologies for TCMS are briefly studied. As it is known, there are plenty of different technologies for sensing and energy harvesting with the potential of implementation in tire systems. In the following sections, the dominant technologies used by researchers for the above-mentioned application, are briefly described . These technologies include electromagnetism, piezoeletricity, and nanogenerators. In this thesis, all of these technologies are utilized to finally reach a proper strategy and platform for this application. First, the principal concept used based on the electromagnetism, is presented in Section 3.1.1. Triboelectric nanogenerators (TENGs) and all of their operating modes are presented in Section 3.1.2. Section 3.1.3 discusses the concept behind piezoelectric generators in both macro- and nano-scales.

3.1.1 Electromagnetic System

Theory of electromagnetism, which is in fact a cornerstone of classical physics, was developed by Maxwell during 1860-1871 [147]. The following set of Maxwells equations (shown in differential form) are the basis of many different technologies varying from macro- to nano-systems:

$$\nabla \cdot D = \rho, \tag{3.1}$$

$$\nabla \cdot B = 0, \tag{3.2}$$

$$\nabla \times E = -\frac{\partial B}{\partial t}, \tag{3.3}$$

$$\nabla \times H = J + \frac{\partial D}{\partial t}, \tag{3.4}$$

in which $J\ [\frac{A}{m^2}]$ and $\rho[\frac{C}{m^3}]$ are the current and electric charge density, H (magnetic field strength $[\frac{A}{m}]$), B (magnetic flux density T), E (electric field $[\frac{V}{m}]$), ∇ denotes the three-dimensional gradient operator, and D (electric flux density $\frac{C}{m^3}$). This set of equations are fundamental relations in antenna, radio, TV, microwave, wireless communications, Internet of Things (IoT), sensors, and blue energy harvesting [148]. In automotive systems, magnetism can be found in anisotropic magneto-resistive (AMR) [149] and giant magneto resistive (GMR) [150, 151], speed/timing sensors, magnetically poled encoder rings [152], dual-magnet sensors [153], TPMS [17], torque sensors [154], and seat-belt tension sensors [155]. They are also the principal equations behind the hybridized sensors presented in this chapter.

3.1.1.1 Electromagnetic Energy Harvester

Energy harvesting based on electromagnetism has several applications such as harvesting energy from wind, ocean wave, and wasted kinetic energy. All of the electromagnetic harvesters operate based on Faraday's law of electromagnetic induction. Thus, an electromagnetic energy harvester should be designed with using at least one coil and one magnet, and a relative motion between them to generate electrical power. Due to the relative motion between a coil and a magnetic field, a current flow is generated in the coil. Suspension systems and tires are considered as the potential components in ground vehicles for energy harvesting based on electromagnetism. Generally, the voltage on the coil is determined by Faraday's law (is related to Maxwell Eq. (3.3)) given by the following equation:

$$\epsilon = -\frac{d\Phi}{dt}, \tag{3.5}$$

where ϵ $[V]$, Φ $[T.m^2]$, and dt are the induced electromotive force (EMF), the magnetic flux, and derivative with respect to time, respectively. Considering a simple case, which consists a coil moving through a perpendicular magnetic field of constant strength, the maximum open circuit voltage across the coil can be obtained by:

$$V_{OC} = nBL\frac{dy}{dt}, \tag{3.6}$$

in which n, L $[m]$, and y $[m]$ are the number of turns in the coil per unit length, the length of the coil, the distance that the coil moves through the magnetic field, respectively. This concept is used in the proposed hybridized generators presented in this chapter.

3.1.2 Triboelectric Nanogenerators

Triboelectrification has been recently used for energy harvesting and active sensing purposes [89, 156, 157]. The triboelectric effect is basically a type of contact electrification in which specific materials become electrically charged after they come into frictional contact with a different material. Based on a conjunction of triboelectrification and electrostatic induction, triboelectric nanogenerators (TENGs), which could convert mechanical energy into electricity, have been introduced [157]. TENGs exhibit a very highly efficient performance in terms of energy conversion, even under operation in variable and harsh environments [96, 158, 159]. Therefore, TENGs have been widely utilized for a variety of applications such as flexible and wearable electronics, bio-medical implantable devices, vibration energy harvesting, and active sensing [148]. In addition, they can be simply fabricated with cost-effective and lightweight materials delivering high power densities for vast micro- and macro-scale systems [148]. Triboelectric nanogenerators have been used for plenty of different applications including pressure sensing [160], bio-engineering, ocean wave harvesting [161], wind energy harvesting [162], and other applications [163–165].

The working principle of this method is based on the premise that when two different materials are brought into contact, a chemical bond is formed between the two surfaces and then charges, i.e. in the form of electrons or ions/molecules, move between the two materials to make the electrochemical potential equal for each material. This surface charge transfer is due to the difference between the polarities of triboelectricity for the two distinct materials, and therefore, one surface achieves positive charges unlike the other surface, which has negative charges. This effect causes an inner potential leading to a charge in outer layers of each material, which are generally covered by electrodes. As the surfaces of the two materials are separated, the charge in the inner layers becomes unbalanced that causes a charge flow to the outer layers to maintain the balance. Therefore, as the distance of the two surfaces intermittently changes, an alternative current is generated in the outer circuit, which results in electrical power generation. This alternative change of distance can be obtained by mechanical stimuli converting kinetic energy to electricity. It should be noted that the two materials must have distinct electron affinities and at least one of them must be an insulator.

3.1.2.1 Operating Modes

Different working modes for TENGs have been recently discovered and developed based on the concept of triboelectrification. Accordingly, four main operating principles for TENGs [156, 159], are discussed in the following parts. The red and blue colors in all figures of this section indicate two distinct materials with opposite electron affinities, and yellow color represents an electrode layer.

3.1.2.1.1 Contact-separation mode

The contact-separation mode, the system operation is schematically presented in Figure 3.1, is the first mode discovered for TENG. First, the two surfaces are brought into contact and then separated by a gap. The corresponding electrodes are connected to a load, and consequently, the electron flow is observed in the formed circuit. Periodic contact and separation of the two materials results in back and forth flow leading to an AC output. The periodic contact-separation switching plays an important role in the power generation; thus, various methods have been designed for this mode of operations such as cantilevers, spring supported systems, arch and cymbal shapes [89, 166]. One of the advantages of this method is that it can be operational in low-frequency inputs, which enables it to be applied in human body kinematics, biomedical devices, machine vibrations, and pressure sensors. [89, 166].

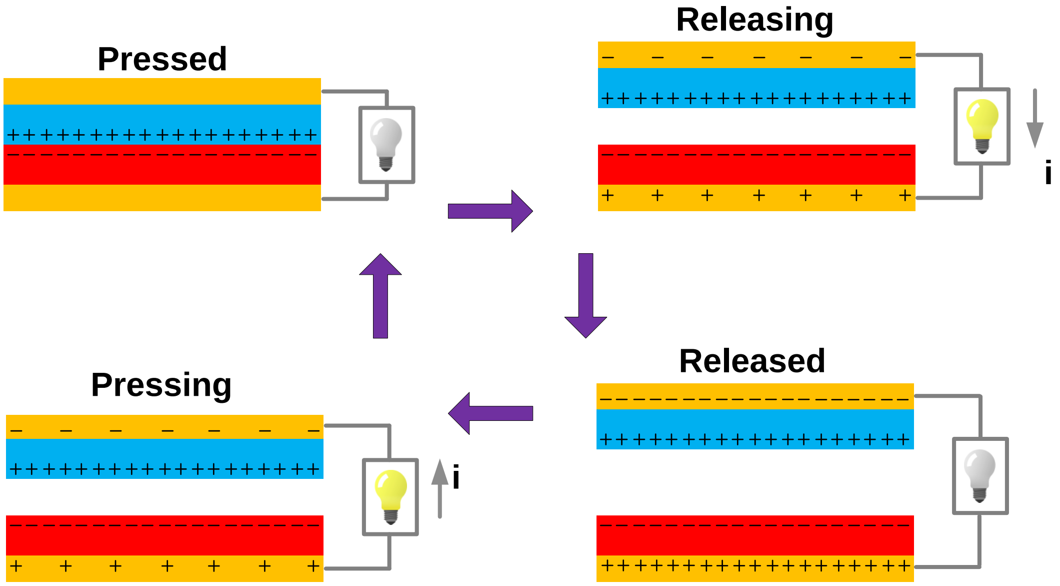

Figure 3.1: Contact-separation mode

3.1.2.1.2 Sliding mode

This working mode is based on the relative sliding motion between the two triboelectric surfaces, as depicted in Figure 3.2. This type of motion causes potential differences across the two materials, which can result in charge flow in outer electrodes. The sliding motion of the two surfaces, originated from the alternative external forces, is more efficient than the first mode in order to improve the output power, and it can be harnessed by the external electrical circuits. Also, this mode can be operated in a variety of ambient motions such as linear and rotational systems, which can be easily implemented in wind and ocean energy harvesting as well as motion sensors [89,166]. High-frequency sliding motion is required for this mode to reach the desired output power for the system.

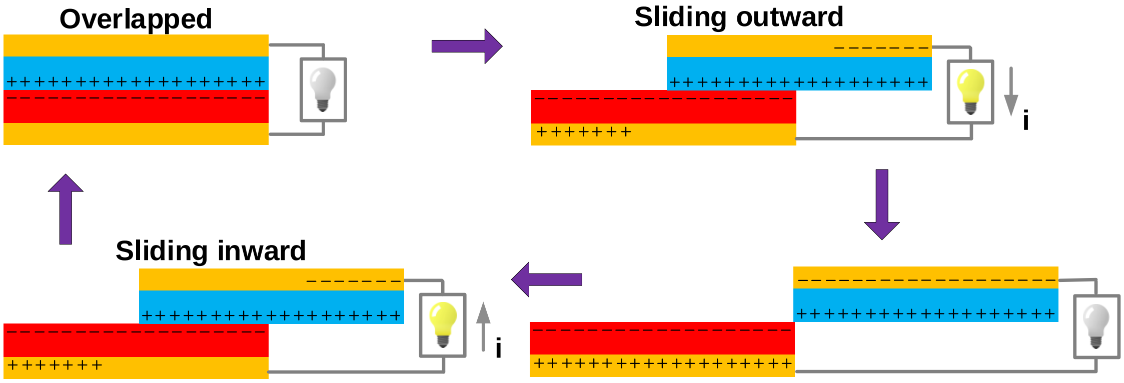

Figure 3.2: Sliding mode

3.1.2.1.3 Single Electrode mode

One of the interesting and simple configurations of TENG is known as the single-electrode mode, as shown in Figure 3.3. The tribomaterial (such as a polymer) is the moving object, while the other material (such as a metal electrode) is fixed and electrically connected to the ground. The working principle of this mode is based on the electron flow between the electrode layer and the ground, which is the result of the unbalanced charge between the moving and fixed layers. This unbalanced charge can be obtained by having contact/sliding and separation of the polymer and the electrode. The outstanding feature of this simple structure is that one of the layers is not bounded in motion and therefore can be used for various mechanical, chemical, and biomedical self-powered sensors [89,166]. It is worth noting that an electrostatic screening effect appears in the system operation, thus reducing the electrode induction, which is known as an important drawback of this mode, and may restrict its use for some specific applications.

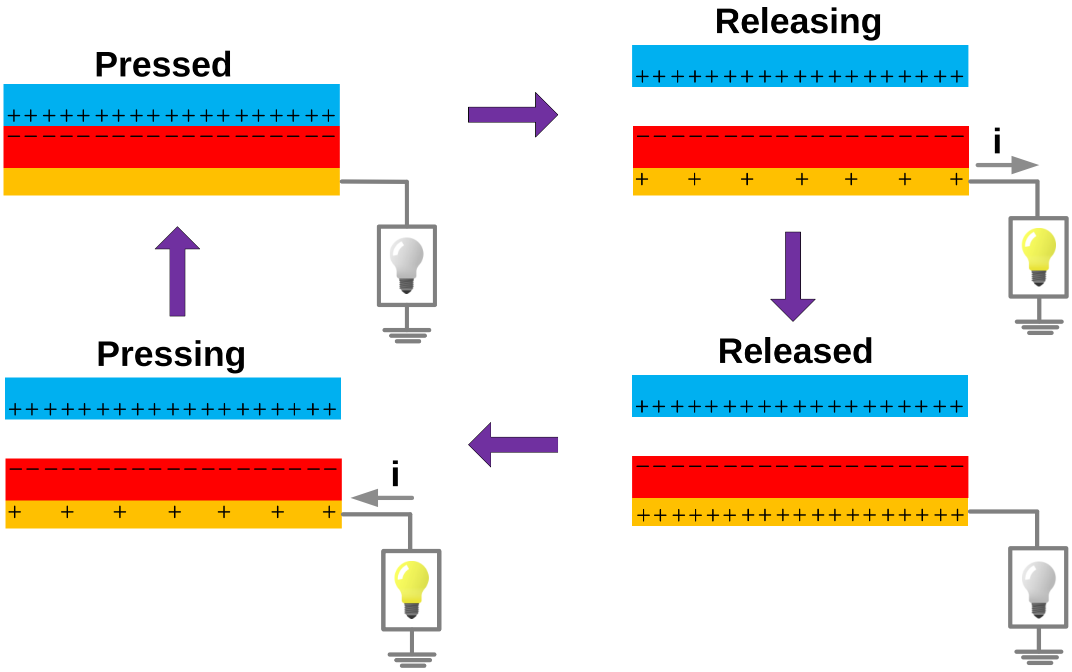

Figure 3.3: Single electrode mode

3.1.2.1.4 Free-standing mode

The free-standing mode is mainly used to eliminate the need of attached electrodes in the structure, as seen in Figure 3.4. In this mode, a pair of symmetrical metal layers is located in a line with a small gap and the moving dielectric, which has the same length of the fixed layers, is moving above the two layers. The oscillation of this layer between the two metals leads to asymmetric charge distribution, thus, an electrical flow is generated in the external circuit. This mode has shown a longer operation life-time in comparison with the second mode due to its lower material abrasion, and heat generation, as well as high energy efficiency. These features enable this mode to be used for various energy harvesting applications such as human motion measurement, automotive systems, air flow measurement, and diverse self-powered sensors [89, 166].

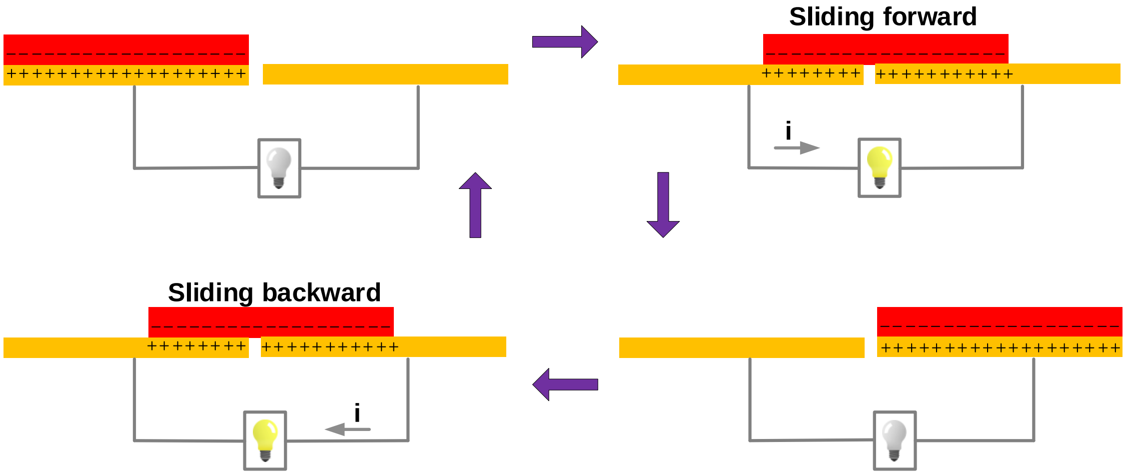

Figure 3.4: Free-standing sliding modes TENG

3.1.3 Piezoelectric Generators

Piezoelectricity is another common technology with applications in both sensing and energy harvesting. The ability of converting applied strain energy into electrical output in piezoelectric materials has attracted the attention of numerous researchers to implement them in both energy harvesting and sensing applications. In addition, piezoelectric materials can be easily integrated into a system. This makes them a suitable choice for implementation in different devices, which require a sustainable power source. The electrical output is generated in piezoelectric materials because of the orientation of their molecular structure. This molecular structure results in a local charge separation, which is called an electric dipole. Accordingly, when a mechanical load is applied to piezoelectric materials, a deformation of dipole occurs, which results in the formation of an electrical charge. This electrical charge can be removed from the piezoelectric materials to be used in sensing and power generation. The fundamental equation for a piezoelectric material is given in Eq. 3.7 and Eq. 3.8.

$$\delta = \frac{\sigma}{Y} + dE, \tag{3.7}$$

and

$$D = \varepsilon E + d\sigma, \tag{3.8}$$

where $\delta, \sigma, Y, d, E, D$ and ε are the mechanical strain, the stress, the Young's modulus, the piezoelectric strain coefficient, the electric field, the charge density and the dielectric constant of the piezoelectric material, respectively. Generally, exerting a period or sinusoidal stress to the piezoelectric material generates an AC open circuit voltage, which can be obtained by Eq. 3.9.

$$V_{AC} = -\frac{\sigma}{\epsilon} dt, \tag{3.9}$$

Assuming a simple resistive load for the piezoelectric generator results in load voltage (V_{load}). Accordingly, the average power can be obtained by $P = \frac{V_{load}^2}{2R_{load}}$.

Zirconate Titanate, a piezoelectric ceramic (piezoceramic), known as PZT is the most common type of piezoelectric materials with applications in power harvesting. Although PZT has been used for power harvesting, it is highly brittle, which limits the applied strain to this type of piezoelectric materials. There are a few other piezoelectric-based materials with applications in sensing and power harvesting such as poly (vinylidene fluoride) (PVDF), piezofiber, flexible piezoelectric materials, MFC composite and piezoelectric nanogenerators.

3.1.3.1 Piezoelectric Nanogenerators

Piezoelectric ZnO nanowires (NWs) were first proposed by Z.L. Wang at the Georgia Institute of Technology as a new platform for energy harvesting and sensing [71]. This concept has shown a remarkable potential for harvesting wasted kinetic energy from micro- and nano-scale mechanical devices. The electrical output generation of ZnO nanowires under a mechanical deflection is caused by the piezoelectric potential generation on the side surfaces because of crystal lattice distortion. Basically, when a piezoelectric NW goes under deflection, the side under tensile gives a positive potential and the other side, which is under compressing load, gives a negative potential. Figure 3.5 shows the potential distribution for a ZnO NW [167].

Implementation of NWs provides three exceptional advantages: i) high sensitivity to small forces, ii) superior mechanical properties, and iii) enhanced piezoelectric effects. These three unique features make them suitable for plenty of sensing and energy harvesting applications. In order to better explain the working mechanism of nanogenerators fabricated from piezoelectric semiconductors materials, the coupled semiconducting and piezoelectric properties [12, 167] could be studied. It must be noted that the direction of the exerted force on piezoelectric materials affects the power generation of piezoelectric nanomaterials. These materials can be used for both AC and DC electric generation [168].

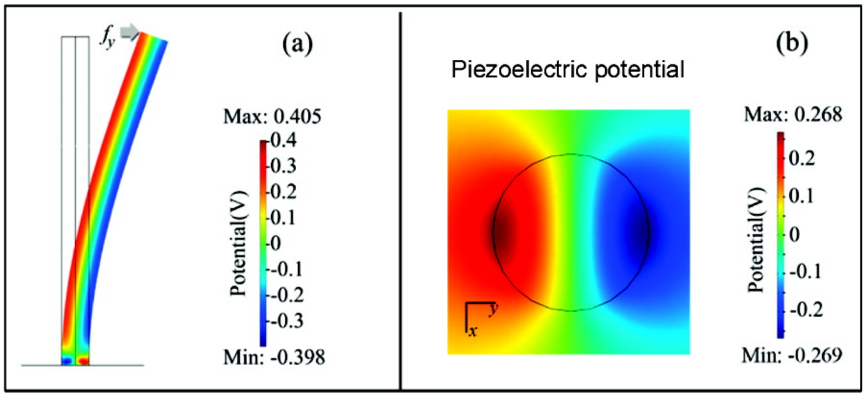

Figure 3.5: Potential distributions for a ZnO NW. (a) side view of the potential profile. (b) cross-sectional view of the piezoelectric potential; reprinted with permission [12], copyright 2006 Science

3.2 In Tire Implementation

The structures of the proposed hybridized sensors have two main parts. The first part works based on the electromagnetic, and the second part operates based on the contact separation mode of triboelectric nanogenerators. Thus, in order to have power generation in both parts, it is indispensable to have a clear understanding from the possible relative deformation in the proposed sensory devices when they enter to the contact patch of a tire. In this section, the cycle of electrical voltage generation in the fabricated devices due to tire deformation in its contact patch is illustrated. Figure 3.6 shows a tire with an attached sensor experiencing deformation.

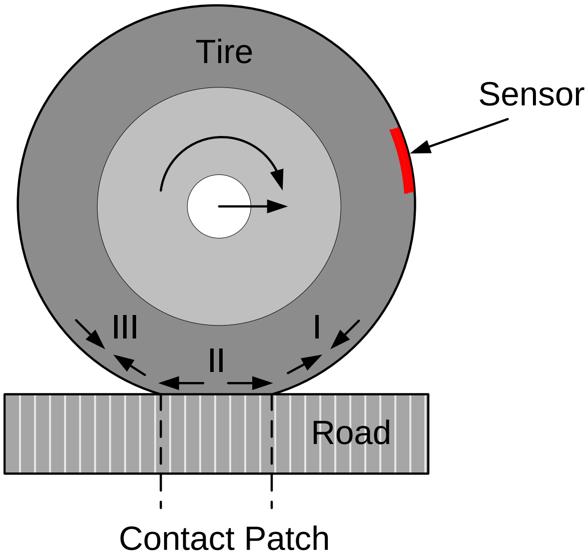

Figure 3.6: Schematic of the deformation of a tire with an embedded sensor: The sensor is attached to the inner liner of the tire will experience compressing stress before and after the contact patch (I and III), and tensile stress in the contact patch (II).

The main aim is to locate the sensor inside the inner liner of the tire. When the fabricated sensor enters to the contact patch at Point A, (See Figure 3.7), a deformation occurs in its flexible part, and it starts generating electrical voltage in both parts of the hybridized sensors. When the sensor is completely in the contact patch, the electrical voltage generation stops until reaching to point B in which the hybridized devices generate the electrical voltage till completely leaving the contact patch as shown in 3.7. These three-steps cycle is the electrical voltage generation cycle of the sensor during one tire rotation.

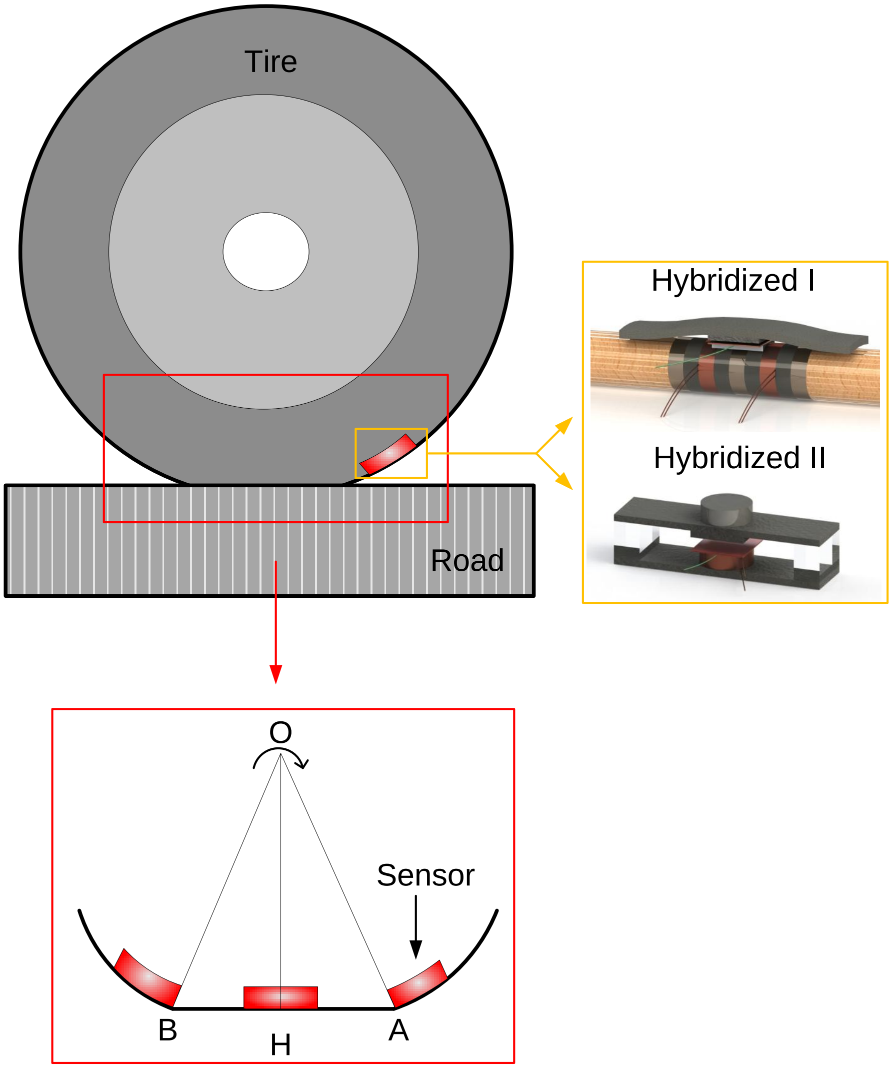

Figure 3.7: Schematic of a tire with an embedded sensor; as fabricated sensor located inside the inner liner of the tire; and the electrical voltage generation cycle of the sensor inside the tire

This cycle is behind the idea of fabricating flexible hybridized self-powered sensing system in this chapter, and flexible sensors for TCMS in Chapter 4. Basically, tire contact patch contains useful information about the interaction forces and moments between the road and the tire. With this idea in hand, the changes in tire-road forces and moments can be measured in the form of electrical voltage. A translation package is required to provide the meaning of the generated voltage during each cycle of tire rotation and correlate them with tire forces and moments. In Chapter 6, information is provided about analyzing, understanding and validating the generated signals using implemented sensor within tire. In the next section, the advantages of using hybridized electromagnetic-triboelectric nanogenerators are illustrated.

3.3 Hybridized Generator

Integrating two types of kinetic energy harvesting results in largely increasing the total output power of the power-harvesting device. The main idea of the hybridization technology is to extract more energy from one source of mechanical motion. Integration of a TENG and an EMG units in a single package enhances the electrical voltage generation in each tire rotation. The integration of TENG to EMG component not only enhances the electrical voltage generation of the device, but also increases the total efficiency and power density.

A hybridized electromagnetic-triboelectric energy-harvesting device encompasses advantages of both electromagnetic and triboelectric mechanisms. Generally, triboelectric nanogenerator (TENG) and electromagnetic generator (EMG) play complementary roles in output performance. TENG is capable of capturing power even in a very small mechanical relative motion. In addition, it can be implemented when there is high impedance in the system. It must be noted that EMG can harvest enough amount of power when there exists sufficient relative displacement between the permanent magnets and coils. In addition, they are usually being used for low impedance circuity systems. Accordingly, the novel self-powered sensing system is capable of power scavenging even in a very small relative motion because of having triboelectric part. These two features help in scavenging energy from a wide-band of frequency and amplitude ranges. That is why the hybridized EMG-TENG sensor is considered as a potential approach for sensing in a tire. Based on this promising potential, two different types of energy harvesting mechanisms are presented as they will be described in sections 3.4 and 3.5.

3.4 Hybridized Sensor I

This section illustrates the design components of the proposed hybridized sensory system, which will be called Hybridized Sensor I. The proposed hybridized design integrates electromagnetism and triboelectricity in a single package. Integration of the two energy harvesting mechanisms provides many advantages such as high sensitivity to both small deflection and low frequency. The main structure of the device consists of a flexible tube, round wood, and Viton rubber. Two clamps are used to hold the wood inside the flexible tube. In the initial design, a single stack of magnet and coil is considered, which consist of two magnets and one coil in the middle of the tube. A flexible foam is located between each set of coil and magnet. In order to increase the capability of the sensing device, a larger stack is fabricated, which includes two coils and three magnets, as shown in Figure 3.8. Section 3.4.1 demonstrates the configuration and working mechanism of the EMG component considering both single and double stacks in detail. Figure 3.8 (a) schematically represents the sensing device. Figure 3.8 (b) shows the zoomed-view of the device. Figure 3.8(c) schematically depicts the device when it is mechanically triggered. When the sensor is deformed, as presented in Figure 3.8 (d), both EMG and TENG components of the sensor are being triggered leading to electricity generation.

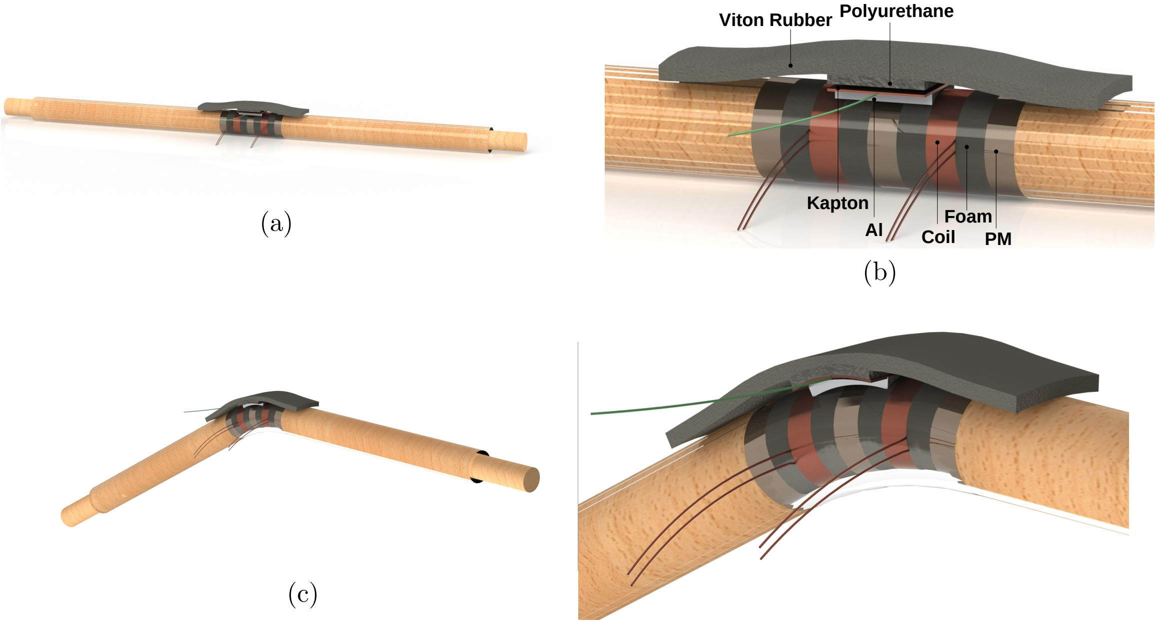

(a)

(b)

(c)

(d)

Figure 3.8: Schematic of the proposed hybrid electromagnetic-triboelectric generator (a) straight tube, (b) zoomed-view, (c) curved tube, (d) zoomed-view of the device under deformation

Figure 3.8 (d) shows the zoomed-view of the deformed sensor. The TENG component of the sensor includes a layer of Polyurethane attached to the middle of Viton rubber, and also, a layer of Kapton, which is attached to the outer surface of the tube. The two edges of the Viton rubber are attached to the outer surface of the flexible tube as shown in Figure 3.8(b). The working mechanism and details about the structure of TENG components are provided in Section 3.4.5.

3.4.1 EMG Structure and Working Mechanism

EMG component of the device, as represented in Figure 3.9, consists of coils, magnets, iron cores, and foams. In a single stack EMG component, the device contains two magnets in left and right sides of a coil equipped by an iron core. Information pertinent to the size of the coils, magnets, and iron cores are provided in Table 3.1. Coils and magnets are connected to each other through the foam. Foams are glued to the coils and magnets. Figure 3.9(a) represents coils, magnets,and iron cores of a double stacks sensing device. Figure 3.9(b) shows the connected double stacks EMG component of the hybridized device.

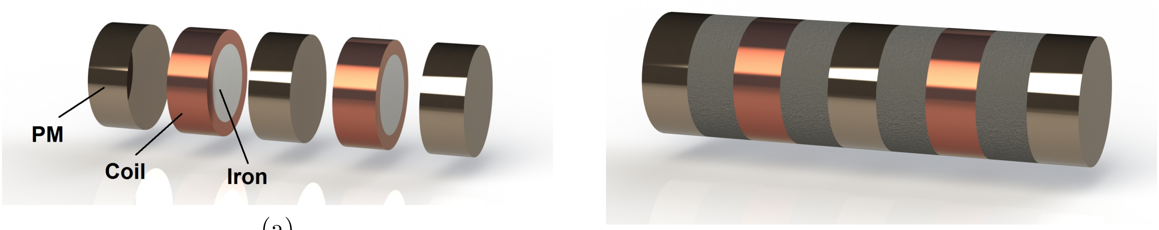

(a)

(b)

Figure 3.9: Electromagnetic component of the sensor (a) without connecting foam, (b) with connecting foam

When a periodical load is applied to the tip of the sensor, the flexible tube is deformed as schematically depicted in Figure 3.10. Deformation of the flexible tube is transferred to the EMG component through the inner liner of the tube and also two holding woods. Thus, it results in deformation in flexible foam as indicated in Figure 3.10. The deformation of the flexible foam provides a relative motion between the coils and magnets. Accordingly, electrical current and voltage are generated in coil wires. Direction of the PM magnetization and their configuration selecting procedure are discussed in Section 3.4.3.

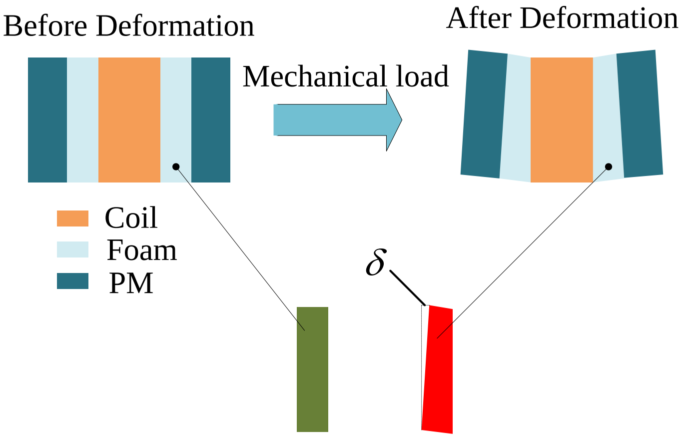

Figure 3.10: A single stack of EMG component, before and after applying mechanical load to the flexible tube

3.4.2 EMG Optimization

In order to maximize the performance of the system in terms of power harvesting, an optimization is performed to select the dimensions of the electromagnetic component. The magnet should be selected based on the availability in the market. Furthermore, the allocated space for the magnet and the coil is limited. Considering these two constraints, a magnet with diameter of $3/8\ in$ and thickness of $1/8\ in$ is selected from the market. For the coil dimensions, a thickness of $4\ mm$ is chosen to fit inside the sensor. The remained parameters for optimization are the inner and outer radius of electromagnetic coil. Figure 3.11 (a) and 3.11 (b) represent the harvested power and power densities (power to coil volume ratio) of the electromagnetic component respectively, for different coil outer radius and different coil outer to inner radius rations. It should be noted that, the obtained values are multiplied by two constants (α and γ for figure 3.11 (a) and 3.11 (b) to normalize the results). As it can be seen, generally by increasing the size of the coil, the harvested power increases (i.e larger R_{out} and smaller R_{in}/R_{out}), however, the best power density is obtained for a smaller coil (i.e. smaller R_{in} and larger R_{in}/R_{out}). Thus, there is trade-off between higher power and higher power density. For this work, the values of 5 and 0.635 for R_{out} and R_{in}/R_{out} are selected respectively, to obtain a good compromise of power and power densities.

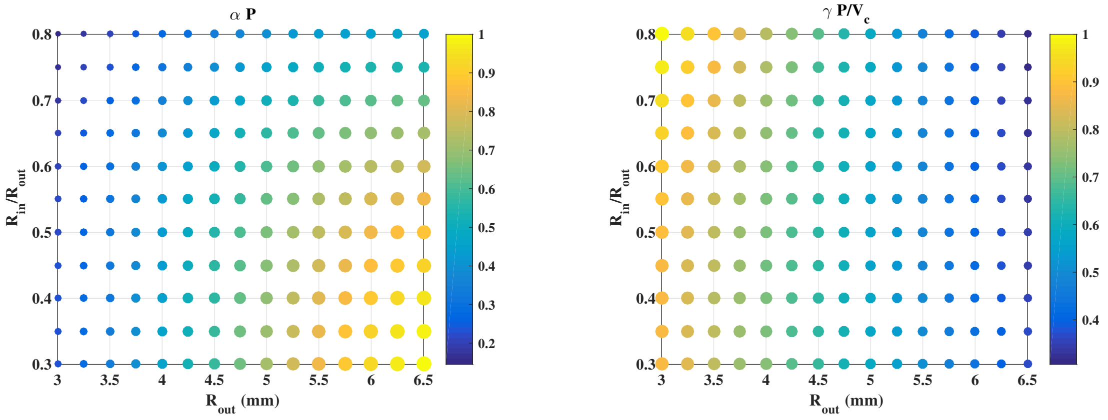

(a) (b)

Figure 3.11: Optimization results (a) variation of output power with respect to the ratio of inner diameter to outer diameter, and also outer diameter, (b) power density (power to coil volume)

Table 3.1: Geometry of the magnets, coils and iron cores

Components	**Thickness**	**Size**	**Turns**	B_r	**AWG**
Round coil	4 mm	R=1 cm	73	○	30
Round PM	1/8 in	R=3/8 in	○	1.35 T	○
Round core	4 mm	R=6.35 mm	○	○	○

3.4.3 Electromagnetic Model and Configuration

The dominant principle in electromagnetic modelling is Faraday and Lenz's laws of induction. In accordance with these combined laws, the following general formulation can be written for the electro-motive force (emf) across the coils:

$$V_{emf} = -\int_{C} (\boldsymbol{E} + \boldsymbol{v} \times \boldsymbol{B}) \cdot d\boldsymbol{l}\,, \tag{3.10}$$

where V_{emf} represents the emf in volts, $\boldsymbol{E}$ and $\boldsymbol{B}$ are electric and magnetic fields, $d\boldsymbol{l}$ is an infinitesimal vector element of the coils wire with a velocity of $\boldsymbol{v}$. After finding V_{emf}, using the Faraday-Lenz's law, the induced current (i) and regenerated power (P_e) of the coil are determined using the following relations:

$$L_{coil}\frac{di}{dt} + \left(R_{coil} + R_{ext}\right) i = V_{emf}, \tag{3.11}$$

$$P_e = R_{ext} i^2, \tag{3.12}$$

where L_{coil} and R_{coil} are inductance and resistance of the coil respectively, and R_{ext} is the resistance of external load connected to the coil. Finding an accurate closed form magnetic field for the considered configuration (coil with iron core) is significantly complicated. However for the case of having no iron core in both round and square cases, a closed form can be obtained for the components of the magnetic field in coil wires. For a cylindrical permanent magnet of radius R_{pm} and length h_{pm}, and remnant magnetic flux density of B_r, the produced magnetic field at any location (r,z) is given by:

$$B_r = B_0 \left[\alpha_+ C\left(k_+, 1, 1, -1, \right) - \alpha_+ C\left(k_-, 1, 1, -1, \right)\right], \tag{3.13}$$

with

$$B_0 = \frac{B_{rem}}{\pi}, \tag{3.14}$$

The coefficients of Eq. (3.13) are defined as below:

$$z_\pm = z \pm \frac{h_{pm}}{2}, \tag{3.15}$$

$$\alpha_\pm = \frac{R_{pm}}{\sqrt{{z_\pm}^2 + \left(r + R_{pm}\right)^2}}, \tag{3.16}$$

$$\beta_\pm = \frac{z_\pm}{\sqrt{{z_\pm}^2 + \left(r + R_{pm}\right)^2}}, \tag{3.17}$$

$$\gamma = \frac{R_{pm} - r}{R_{pm} + r}, \tag{3.18}$$

$$k_\pm = \frac{\sqrt{{z_\pm}^2 + \left(R_{pm} - r\right)^2}}{\sqrt{{z_\pm}^2 + \left(R_{pm} + r\right)^2}}, \tag{3.19}$$

where C represent a generalized complete elliptic integral given by:

$$C\left(k_c, p, c, s\right) = \int_0^{\pi/2} \frac{c\,\cos^2\phi + s\,\sin^2\phi}{\left(\cos^2\phi + p\,\sin^2\phi\right)\sqrt{\cos^2\phi + {k_c}^2\,\sin^2\phi}} d\phi. \tag{3.20}$$

An important part of the design of the proposed flexible sensor is the magnetization direction of each magnet inside the tube. The strength of the magnetic field is studied after locating each magnet beside each other using COMSOL, and finally obtained the configuration indicated in Figure 3.12 as the optimized arrangement for the permanent magnets. Figure 3.12 represents the implemented arrangement of the PMs and coils in the tube for a simple case, which includes one PM and one coil, a single stack, which contains two PMs and one coil in the middle, and finally, a double stack with three PMs and two coils. Figure 3.13 shows the curved tube after applying a mechanical load, which results in angle θ. Based on Figure 3.13, the angle θ is approximately found by the following simple mathematical calculation:

$$\theta = tan^{-1}\frac{c}{b}, \tag{3.21}$$

This shows the potential of the device for measuring of the angular deformation, as experienced in a tire cycle of rotation.

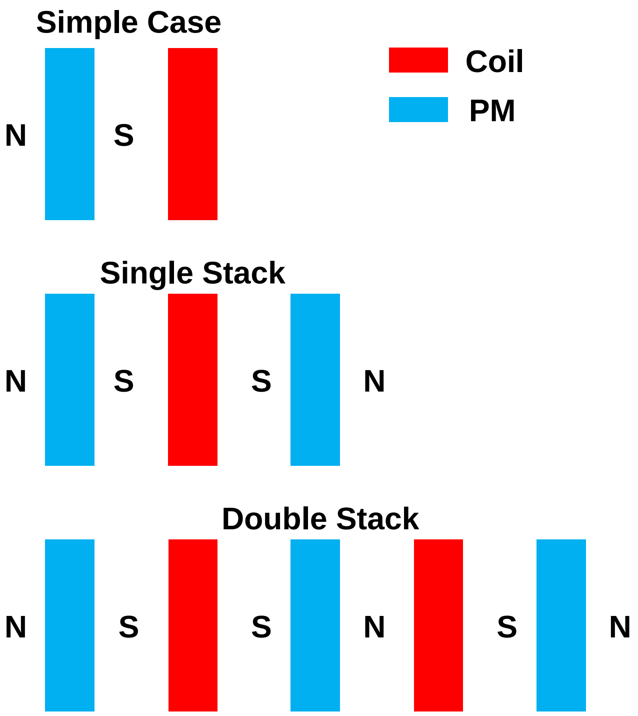

Figure 3.12: Configuration of the EMG component considering simple case, single stack and double stack of PMs and coils

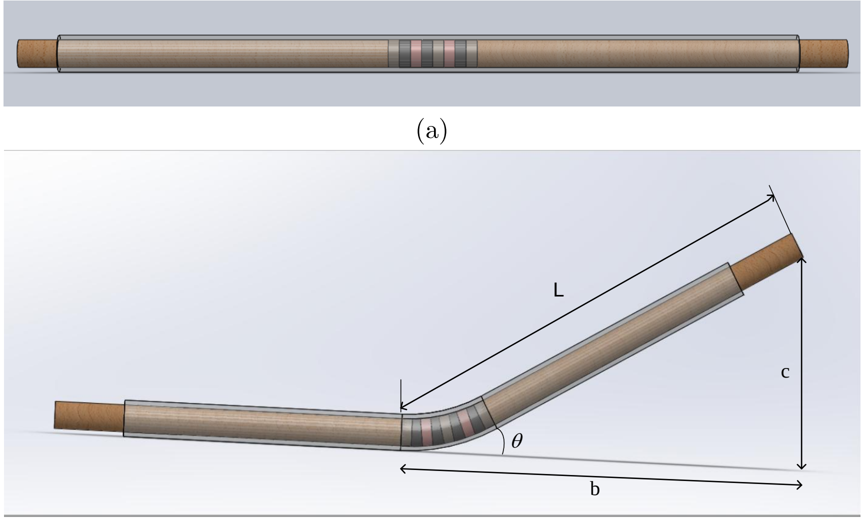

(a)

(b)

Figure 3.13: Schematic representations of the sensor (a) before applying the mechanical load, (b) after applying the mechanical load

3.4.4 Finite Element Analysis-EMG Component

This section presents the finite element analysis for both EMG and TENG components. There are two main reasons for using FEM simulations in our design procedure. The first one is related to the optimization of the coil and iron core ratio for having the best electrical output. The second reason of using FEM analysis is attributed to finding the best configuration for locating permanent magnet in the stack of coil and PMs in terms of magnetization direction. Figure 3.14 represents the FEM results for the EMG components. Figure 3.14(a) represent the magnetic flux density for a simple system consisting a PM, a coil and an iron core. Figure 3.14(b) shows the magnetic flux density for a simple system consisting a PM, a coil with air core. Figure 3.14(c) represents the magnetic flux density for a single stack system without iron core, and Figure 3.14(d) shows the magnetic flux density for a single stack with iron core. Figures 3.14(e)-(f) illustrate the magnetic flux density for a double stack system without and with iron cores, respectively. As indicated by the figures, adding iron core to the coil results in enhancement of the magnetic flux density in the coil.

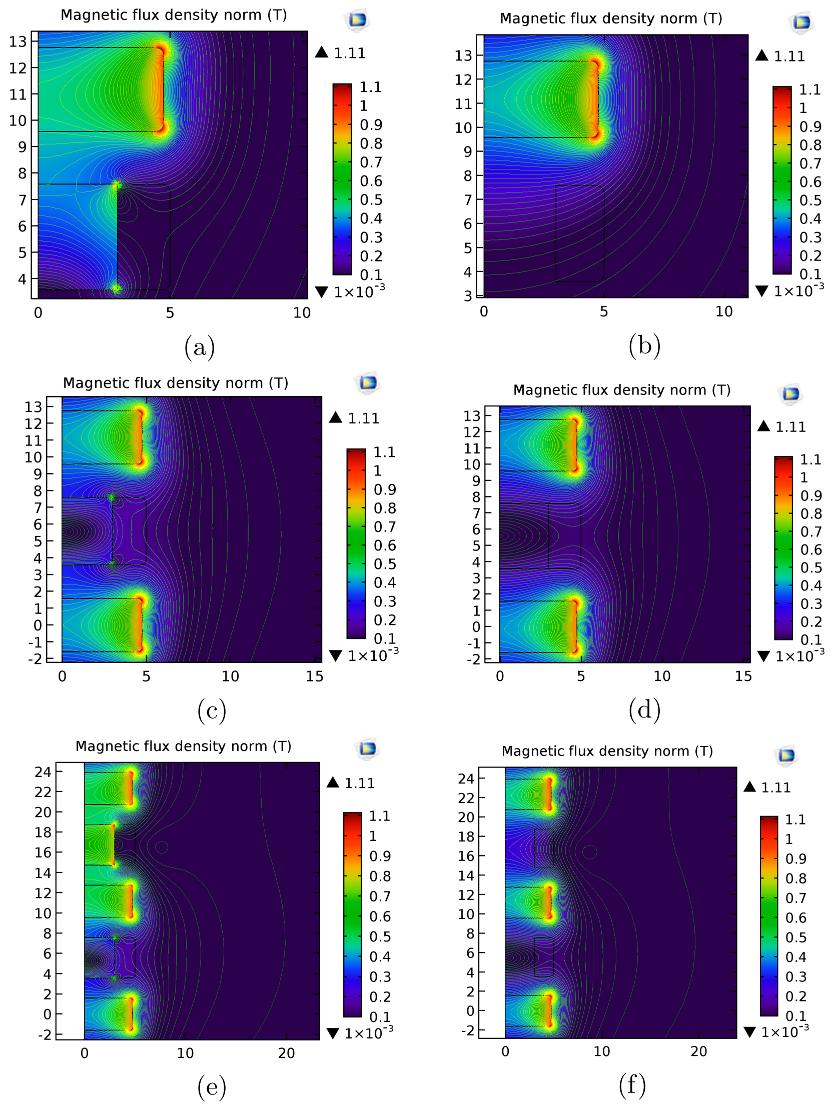

(a) (b) (c) (d) (e) (f)

Figure 3.14: FEM model of the EMG component (a) simple case with iron core, (b) simple case without iron core, (c) single stack with iron core, (d) single stack without iron core, (e) double stack with iron core, (f) double stack without iron core

3.4.5 TENG Structure and Working Mechanism

The operation principle of the TENG sensor is based on the single-electrode mode TENG, as schematically shown in Figure 3.15. This part includes highly flexible, mechanically and thermally durable, and cost-effective polymeric materials. When the tube structure is being excited, the contact layers of the TENG sensor will be under contact and separation in each cycle of excitation. When the two layers are in full contact and due to triboelectricity, negative and positive charges are generated in Kapton and Polyurethane surfaces, respectively (Figure 3.15(a)). The electrode is connected to the electrical ground and no electron flow occurs in between owing to the balance condition. As the two layers separate and a gap takes place, electrons flow from the metal electrode toward the ground due to the variation of local electrical field (Figure 3.15(b)). The flow continues until reaching the maximum gap where the balance condition is achieved and the charge transfer is stopped (Figure 3.15(c)). By approaching the Polyurethane layer toward the Kapton layer, the electrons flow back in opposite direction of the separation case (Figure 3.15(d)).Thus, an alternative current is generated owing to the flow of electrons, which reveals the process of electricity generation.

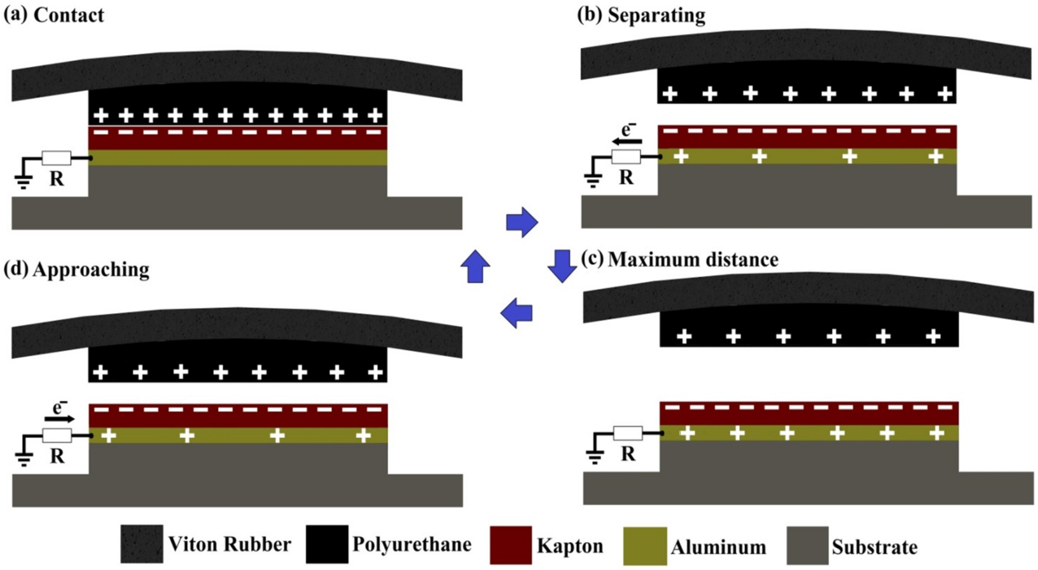

Figure 3.15: Working mechanism of the single-electrode mode TENG sensor in one full cycle

3.4.6 Finite Element Analysis- TENG Component

In addition, a study has been performed using finite element method (FEM) to realize the electric potential distribution in the sensor and the charge transfer between the ground and the electrode for the TENG component of the device. Figure 3.16(a) shows the schematic FEM model developed in COMSOL software in which the effect of changing the relative gap distance, i.e. z, was evaluated. A 2D model was considered since the thickness of contact layers and gaps are relatively small compared to the other dimensions of the device. As Kapton and Polyurethane are insulating materials, charges are uniformly distributed on the contact surfaces. Thus, the Kapton surface was assigned with a negative charge density while the same magnitude with opposite polarity was assigned to the Polyurethane surface to maintain the charge conservation. The dimensions were all selected equal to the fabricated sensor. The model was surrounded by air similar to the actual device and infinity was chosen as the reference point in the simulation. The effect of varying gap on the electric potential distribution was calculated in open-circuit condition. As a result, increasing the gap will enhance the electric potential, as shown in Figures 3.16(b)-3.16(d). Also, the variation of open-circuit voltage on the electrode versus the gap distance was shown in Figure 3.16(e) where the voltage is relatively dependent to the gap size. Therefore, the FEM analysis verifies the process of electricity generation in an excitation cycle where the distance between contact surfaces is being changed from zero to a maximum value.

Here is the final fabricated hybridized sensor I using both TENG and EMG mechanisms (Figure 3.17). Figure 3.17(a) shows the fabricated sensor with a single stack EMG component. Figure 3.17(b) shows as-fabricated sensor with a double stack EMG component incorporated with the TENG component.

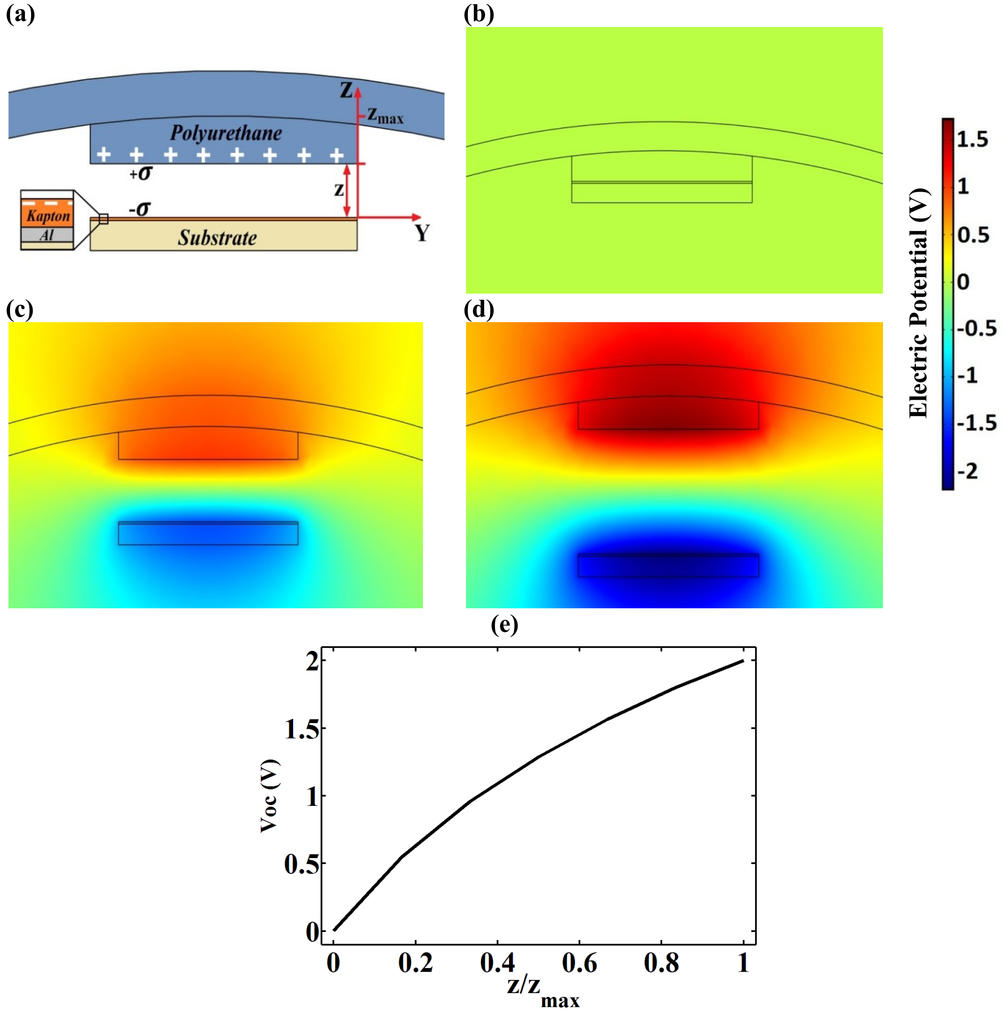

Figure 3.16: (a) FEA model of the TENG section, (b)-(d) electric potential distribution for $\frac{z}{z_{max}} = 0, 0.5, 1$ (e) variation of open-circuit voltage on the electrode versus the relative displacement $\frac{z}{z_{max}}$


(a) (b)

Figure 3.17: Fabricated hybrid electromagnetic-triboelectric generator: (a) single stack (b) double stack

3.5 Hybridized Sensor II

This section fully describes design and working mechanism of the Hybridized Sensor II. First, the electromagnetic component of the proposed system is illustrated. In addition, a detailed geometrical information is provided for EMG component, and also, its working mechanism is fully discussed. Section 3.5.2 describes design and working mechanism of TENG component of the proposed energy harvester. Figure 3.18(a-b) schematically represents the proposed hybridized sensor with round PMs, and coils and also its cross section view, respectively.

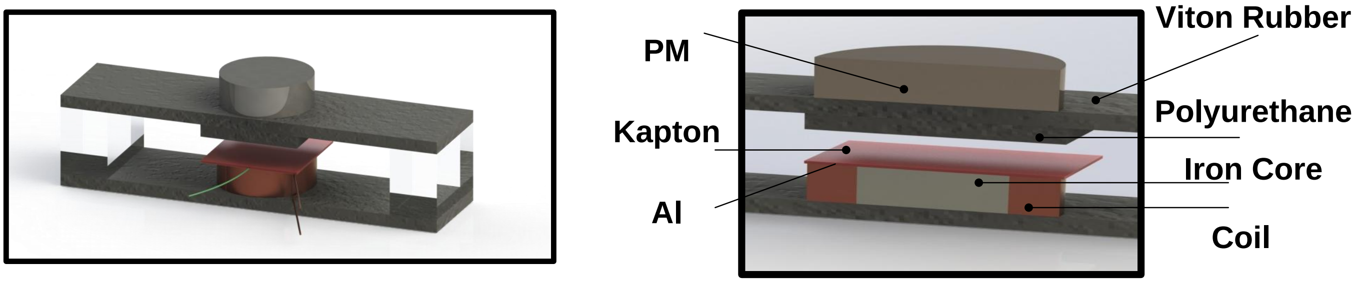

(a) **(b)**

Figure 3.18: Schematic of the proposed hybrid electromagnetic-triboelectric generator: (a) circular shape PM and coil (b) cross section view of circular shape

Similarly, Figure 3.19(a-b) schematically show the system with square shape PMs and coils and also its cross section view, respectively.

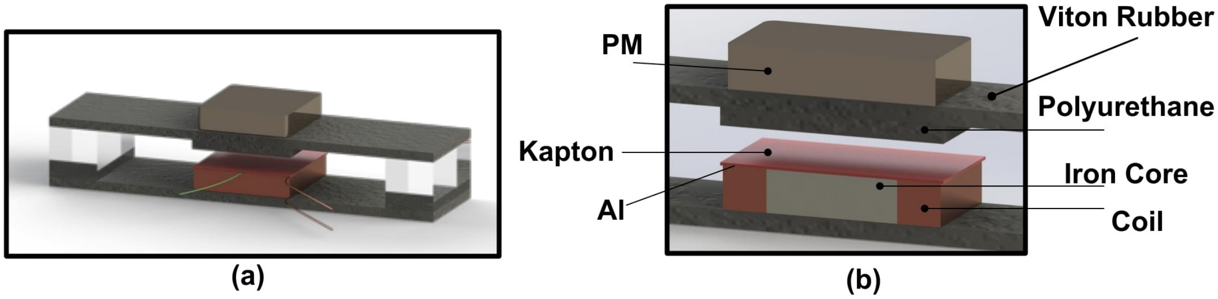

Figure 3.19: Schematic of the proposed hybrid electromagnetic-triboelectric generator: (a) square shape PM and coil, (b) cross section view of square shape

3.5.1 EMG Structure and Working Mechanism

As indicated in Figures 3.18 and 3.19, two types of hybridized sensors with similar configuration are presented in this section. The first one contains a cylindrical permanent magnet (gray color), and a cylindrical coil (copper color). The second design includes a square shape permanent magnet and coil. Each coil has an iron core as indicated in the Figure. The permanent magnet is located on top of the rubber and the coil is placed under the Kapton as indicated in Figure 3.18. The iron core closes the magnetic flux circuits, and thus, enhances the energy regeneration rate. Table 3.2 provides the details relevant to the geometry and properties of both coils and magnets. The electromagnetic component of the hybrid design functions based on the Faraday′s and Lenz′s laws. Faraday′s law of induction states that the change of the total flux in a closed circuit results in an induced electromotive force proportional to the rate of change of flux through the integral path. According to the Lenz′s Law, the induced magnetic field produced by the induced current will oppose the direction of the original magnetic field. Applying an external force, pressure or moment on the fabricated sensor causes a relative displacement between the magnet and the coil, resulting in current inside the coil wires, and thus, generating voltage.

Table 3.2: Geometry of the magnets, coils and iron cores

Components	**Thickness**	**Size**	**Turns**	B_r	**AWG**
Round coil	4 mm	R=1 cm	73	○	30
Square coil	4 mm	L=1 cm	73	○	30
Round PM	1/8 in	R=3/8 in	○	1.35 T	○
Square PM	1/8 in	L=3/8 in	○	1.35 T	○
Round core	4 mm	R=6.35 mm	○	○	○
Square core	4 mm	L=6.35 mm	○	○	○

3.5.2 TENG Structure and Working Mechanism

TENG component of the sensor contains a layer of Polyurethane and a layer of Kapton with a thin Aluminum electrode on its bottom. As represented in Figure 3.20, Kapton layer is located on the top surface of the coil. The location of Polyurethane is under the PM. The working mechanism of the TENG component is schematically depicted in Figure 3.20, which is based on the conjunction of contact electrification and electrostatic induction. When the device is being pressed, the surfaces of Kapton and Polyurethane are fully in contact so that the charges will be transferred between them, as shown in Figure 3.20(a). The reason is that the Kapton layer is more triboelectrically negative than Polyurethane, and therefore, electrons are transferred to the Kapton surface. The Kapton layer holds negative charges while the Polyurethane surface obtains similar magnitude of charges with opposite polarities to maintain the charge balance. In this condition, there is no electron flow between the electrode and the ground, which are connected to each other through an external electrical load. As the Polyurethane layer departs the bottom layer, the local electrical field distribution will be changed leading to the electron flow from the electrode toward the ground, as seen in Figure 3.20(b). The maximum charge transfer is obtained when the top layers reaches to a specific distance where the charge balance is fully achieved, as depicted in Figure 3.20(c). Similarly as the Polyurethane approaches the bottom layer, the electrons are driven back through the external load to maintain the balance until reaching the full contact (Figure 3.20 (d)). Therefore, such process will result in an electricity generation.

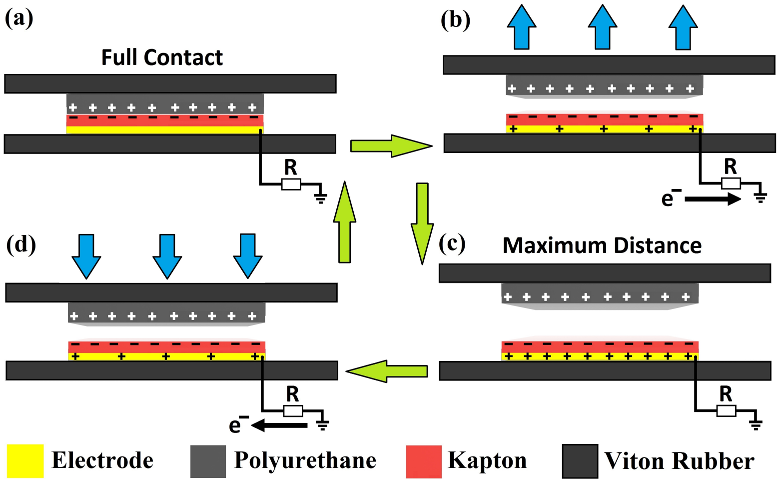

Figure 3.20: Mechanism of the TENG component of the hybridized sensor under one cycle of pressing and releasing

3.5.3 Finite Element Analysis: EMG Component

This section provides the finite element analysis for both EMG and TENG components. Figure 3.21(a-d) shows the radial magnetic flux density at different locations obtained by COMSOL ® multiphysics software package (version:5.2a) for EMG component with round coil and PM. Figure 3.21(a) represents a 2D view of the radial magnetic flux density of the EMG component with iron core. Figure 3.21(b) shows a 3D view of magnetic flux density of the the EMG component with iron core. Figure 3.21(c-d) illustrate 2D and 3D views of the magnetic flux density of the EMG components without iron core. It must be highlighted that using iron core increases the maximum of the radial magnetic flux density in coil from 0.11758 T to 0.30304 T. It is a significant increase as expected based on the optimization results, which is presented in Section 3.4.2. Figures 3.21(e) and (f) represent the magnetic flux density in square shape coil and magnet with and without iron core, respectively. Similar to the round shape, the magnetic flux density increases with implementing the iron core.

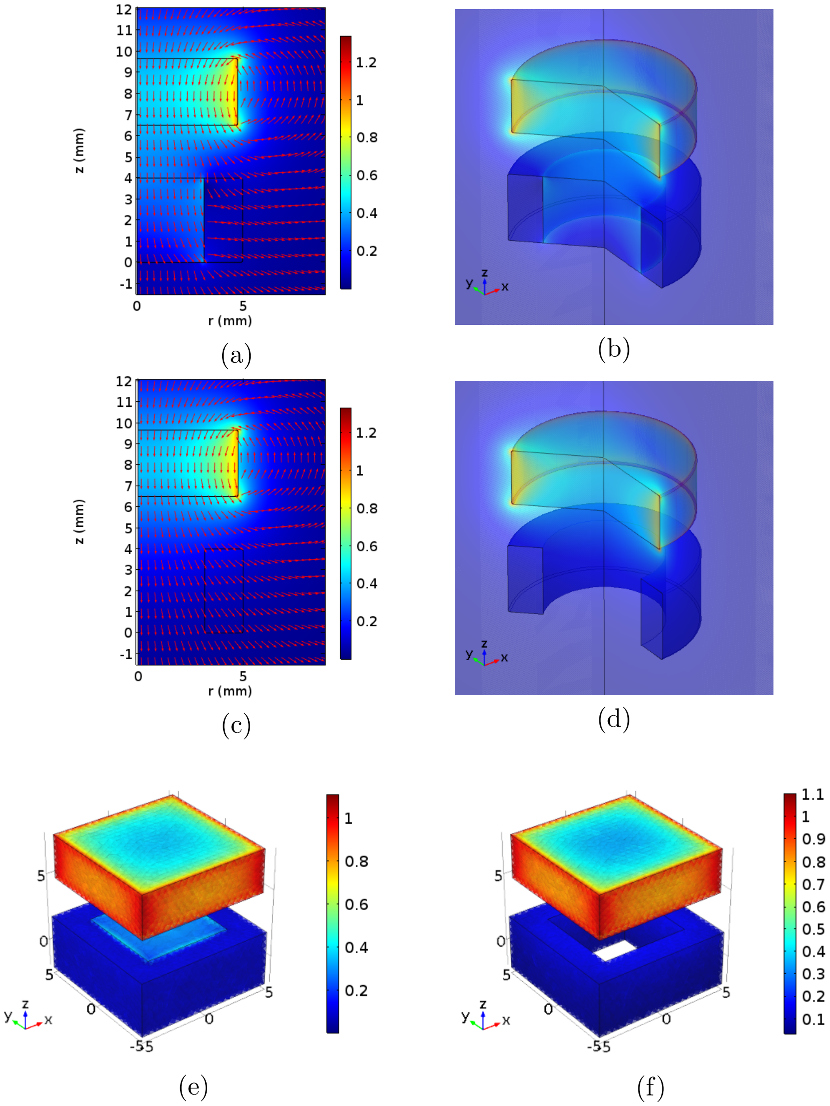

(a)
(b)
(c)
(d)
(e)
(f)

Figure 3.21: Electromagnetic component FEM representation of the coil and magnet: magnetic flux density (T) (a) 2D view with iron core for circular shape, (b) 3D view with iron core for circular shape, (c) 2D view without iron core for circular shape, (d)3D view without iron core for circular shape, (e) square shape with iron core, (f) square shape without iron core

3.5.4 Finite Element Analysis: TENG Component

In order to analyze the operation of the TENG component, a finite element model is carried out in COMSOL ® software, as schematically shown in Figure 3.22(a). The electric potential distribution in the open circuit (OC) condition is calculated by changing the distance between the top and bottom layers. The Kapton layer and attached electrode was fixed, and the external excitation results in changing the position of Polyurethane layer. The 2D model was taken into the account due to the very small thickness of contact layers in comparison with other dimensions of the layers. A similar magnitude of the surface charge density is assigned on both surfaces, but with an opposite polarity to the bottom surface. The charges were uniformly distributed on the contact surfaces owing to the insulation properties of the selected materials. The potential at infinity was taken as the reference condition and the entire system was surrounded by air same as the real experimental condition.

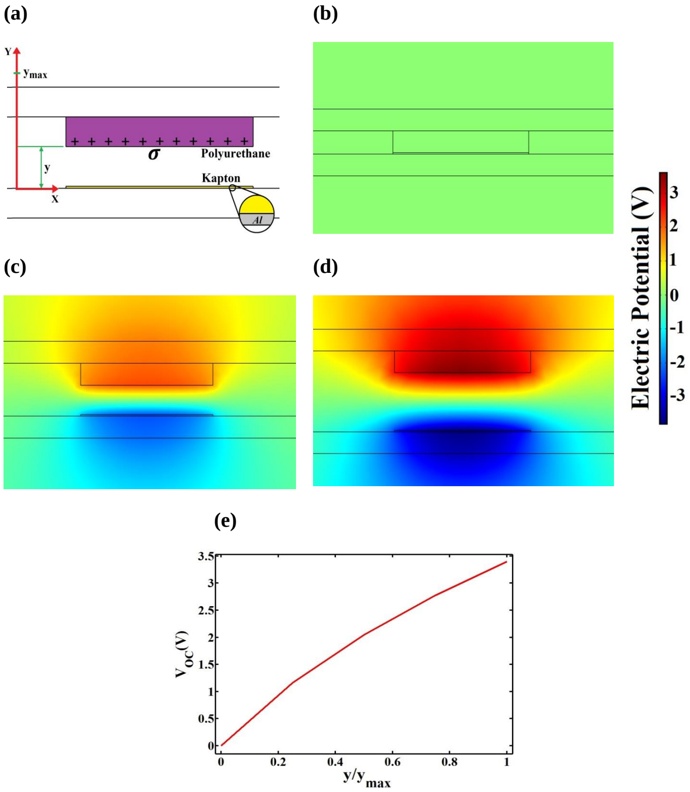

Figure 3.22: (a) FEM model for the TENG component (b)-(d) electric potential distribution for $\frac{y}{y_{max}} = 0, 0.5, 1$. (e) open-circuit voltage with respect to the relative displacement

Figures 3.22(b)-(d) show the variation of potential distribution when the distance changes from zero to the maximum condition. Accordingly, the electric potential is increased as the top layer departs from the bottom layer. Figure 3.22(e) shows the variation of open-circuit voltage V_{oc} with respect to the relative displacement (y/y_{max}). The voltage is increased by raising the top layer indicating the generation of electricity when the system is being pressed and released. Here is the final fabricated Hybridized Sensor II using both TENG and EMG mechanisms (Figure 3.23). Figure 3.23(a) shows the fabricated sensor with a round shape magnet and coil. Figure 3.23(f) shows as-fabricated sensor with a square shape coil and magnet.

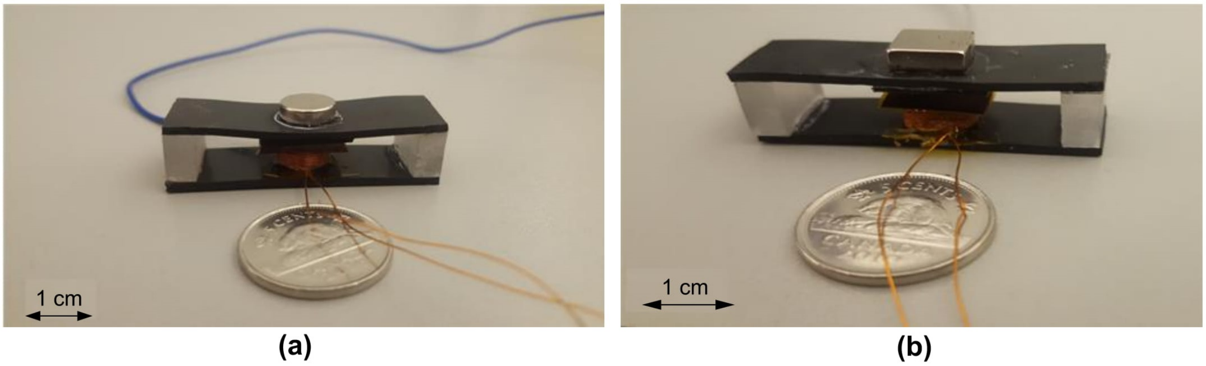

Figure 3.23: As-fabricated hybrid electromagnetic-triboelectric generator: (a) circular shape PM and coil(b) square shape PM and coil

3.6 Concluding Remarks

Two types of flexible hybridized EMG-TENG devices were designed, modelled, optimized and fabricated for TCMS. It was discussed where and how these devices can be implemented in a tire. Finite element models were provided for each unit of the proposed sensory devices. In addition, a study was presented regarding the configuration of the EMG component of proposed hybridized sensory I. The proposed devices are tested for the considered application of this thesis to show their potency and effectiveness in converting mechanical energy into electricity in Chapter 5.

Although, the designed hybridized sensors have flexible structures, but their size and weight could be considered as their main drawbacks for tire-condition monitoring systems. In addition, considering the tire environment, it was noticed that it is not a clean area, and it is full of rubber dusts, which could have a negative impact on TENG units of the proposed hybridized sensors as they are not fully insulated from the environment. Another issue for implementing these devices within tire is attributed to their durability. The above-mentioned drawbacks of these designs, and also the high potential of TENG used in the hybridized devices lead towards studying and developing novel flexible nanogenerators, which will be presented in the next chapter.

Chapter 4

Flexible Triboelectric Nanogenerators

As it was stated in previous chapters, the main objective is to design a flexible sensor, which can endure the harsh environment of tire, with the capability of providing measurement of tire dynamical parameters. In addition, it should have no negative impact on the dynamics of the vehicle due to its size, as it is attached to an inner liner of a tire. In this chapter, three novel designs of flexible sensors, based on the triboelectrification effect, are introduced with potential application in tire-condition monitoring. The flexible materials and sensors are first introduced in Section 4.1, then, the focus will be on the proposed sensors with illustrating the related design procedure, modelling, and fabrication taking into account tire-condition monitoring application. In addition, the working mechanisms of each of proposed flexible sensors are fully illustrated.

4.1 Flexible Sensors in TCMS

Flexible sensors, based on triboelectric nanogenerators, have shown a great potential for sensing and energy harvesting for different applications. They have been used so far in different applications including wind and water wave energy harvesting, traffic flow monitoring, tire condition monitoring, tactile sensing, biomedical energy harvesting, and safety systems. Nanogenerators, especially TENGs, have shown a high power density in comparison with other competitive technologies such as electromagnetic generators (EMGs). There are plenty of other advantages for nanogenerators in comparison with EMGs including high voltage, high efficiency at low frequency, low cost, low weight, multiple working modes and material choices. Figure 4.1 highlights different applications of nanogenerators.

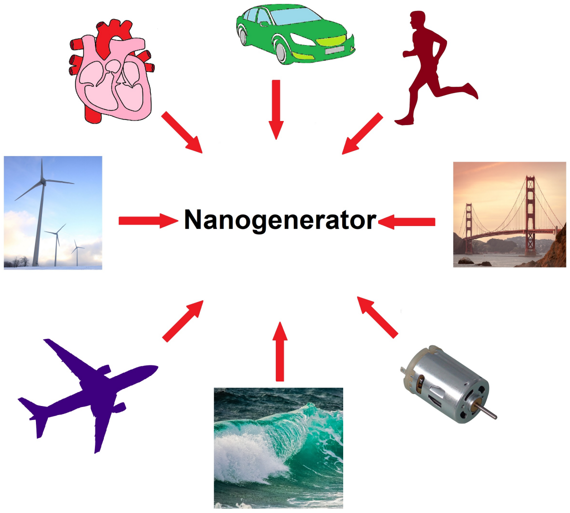

Figure 4.1: Applications of nanogenerators in different systems

All of the promising potentials of the flexible nanogenerators are persuasive to use them for tire-condition monitoring application. Figure 4.2 schematically represent a tire with an attached flexible sensor.

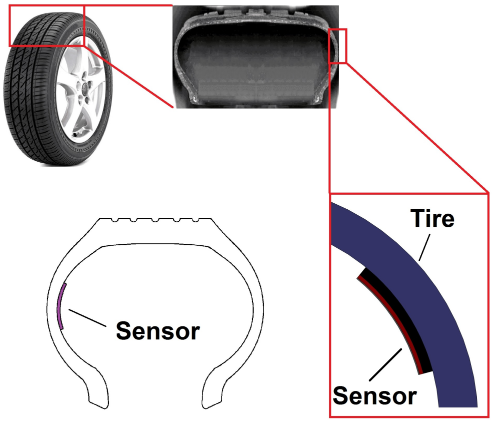

Figure 4.2: A flexible sensor attached to inner liner of a tire with its zoomed-view and cut cross section

The main idea is that when the flexible TENG based sensor enters to tire contact patch, it starts electrical voltage generation based on the triboelectrification effect. Similar to what was discussed in previous chapter about the cycle of electrical voltage generation for the hybridized sensor happens for the flexible TENG-based sensors. Comprehensive information about this electrical voltage generation cycle can be found in 3.2. Taking into account the potential of the flexible nanogenerators, three different types of sensors are developed based on this technology. The evolution of the designed sensors, for TCMS based on the flexible TENGs, are shown starting with a flexible single electrode TENG in Section 4.2, and ending with an encapsulated double electrode flexible TENG in Section 4.4.

4.2 Flexible Sensor I

The first flexible sensor, which will be introduced here, operates based on the single electrode mode. This sensor contains two polymer layers and one electrode. Two polymer layers are Kapton and Polyurethane, and Aluminum plays role of an electrode. In the next part, the main criteria for the design of this flexible sensor is discussed.

4.2.1 Design

In order to design a flexible sensor for TCMS based on the triboelectrification effect, it is needed to choose an operating mode for this specific application. Therefore, single electrode mode is selected as an operating mechanism for the first flexible sensor, as it would have one polymer face ready for attaching to the inner liner of a tire. Also, the selected material must be thermally durable for working in the harsh environment of a tire. In terms of thermal durability, the selected materials for fabricating the sensor including Kapton and Polyurethane can withstand in both low and high temperature, which are both lower and higher than the operating temperature range in a tire. Table 4.1 describes the lowest and the highest temperature in which the chosen materials can withstand. Polyurethane is a thermosetting polymer, and it withstands in temperature range of -40 to 250. In addition, it is flexible enough to experience large deformation. Similarly, Kapton is a Polyimide film, which remains stable in a wide range of temperature variation, and it is a proper choice for the harsh environment of a tire.

Table 4.1: Thermal operating range of the selected materials

Material	**Operating Temperature Range**
Polyurethane	-40 to +250 $°C$
Kapton	-40 to +300 $°C$

As stated above, the whole sensor has three layers including Kapton with a deposited layer of Aluminum, and Polyurethane. The other reason of selecting Kapton and Polyurethane is their ability for gaining and losing electron. Based on the triboelectrification series, Polyurethane is highly prone to lose electrons, and Kapton is very potent for gaining electron. In Section 4.2.4, the fabrication procedure of the sensor is fully illustrated, considering the design criteria presented here.

4.2.2 Working Mechanism

The working mechanism of the sensor lies on the concept of single-electrode mode TENG, as shown in Figure 4.3 [169]. In each cycle of the tire rotation, the sensor is bent and released owing to the applied pressure to the tire while contacting the ground. When the sensor is bent, the two friction layers contact each other, and due to triboelectrification between the surfaces, equivalent negative and positive charges are generated on the Kapton and PU layers, respectively (Figure 4.3 (a)). During the releasing process of the sensor, positive charges will be induced on the electrode owing to the effect of electrostatic induction. As a result, electrons flow between the electrode and electrical ground (Figure 4.3(b)) due to the corresponding potential difference until reaching an electrical equilibrium (Figure 4.3(c)). Similarly, the electrons flow back in a reverse direction as the sensor starts bending (Figure 4.3(d)). The flow of electrons between the electrode layer and the electrical ground induces an alternating current through the external circuit resulting in electricity generation. It must be noted that the two short edges of the sensor layers are sealed while a small relative distance exists between the two layers. Figure 4.3 shows the middle section of the sensor where the maximum separation, sliding, and subsequently triboelectrification takes place between the two layers. Such relative sliding and separation can be attributed to two main reasons. First, there exists non-uniform roughness on the surfaces of the two materials which causes a small friction and separation under bending force. Second, the sensor edges are sealed when the two layers are straight while the sensor is in a curved shape in order to match the tire curvature. Therefore, a small relative distance exists between the two layers, as the layers show different elastic behavior in a curved structure.

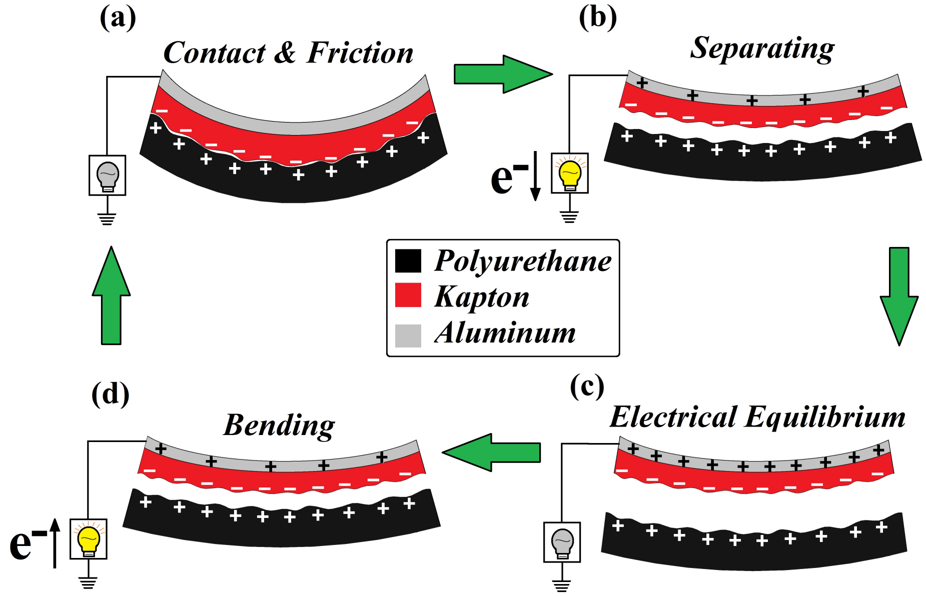

Figure 4.3: Working mechanism of the flexible TENG sensor in an operating cycle (This shows the middle section of the sensor where the maximum separation occurs under bending)

4.2.3 Finite Element Analysis

In order to quantitatively understand the function of the TENG sensor, the working principle of the sensor is studied by a Finite Element Analysis (FEA) using COMSOL software. The main reason of using FEM for TENG sensor is to show its electrical potential during each cycle and the feasibility of electricity generation based on the used polymers, electrode and considered configuration. The behavior of the sensor is modelled under the working condition i.e. bending and releasing imposed by the tire deformation. Then, the corresponding potential charge distribution and the open-circuit voltage are obtained through this process. As the thickness of each layer is much smaller than the sensor width, a 2D model is used in the simulation. Figure 4.4(a) shows the FEM model where the sensor is initially in the released condition $x = 0$, and then undergoes a bending deformation until reaching the maximum deformation of $x = x_{max}$. Figures 4.4(b)-(e) show the electric potential distribution of the sensor. Electric potential distributions are shown when no bending is applied to the sensor (figure 4.4(b)), and then the sensor is bent gradually to reach the maximum deformation (Figure 4.4(e)). It is observed that increasing the deformation reduces the electric potential as the effective contact layers further come in to contact. It is found that the maximum distributed electric potential when the sensor is fully released. In addition, Figure 4.4(f) depicts the variation of the generated open-circuit voltage V_{oc} (between the electrode layer and ground) with respect to the relative displacement (x/x_{max}) of the sensor. This reveals that the process of bending and releasing the sensor results in generation of electricity through the external circuit, which can be used as the signal of the sensor.

4.2.4 Sensor Fabrication

A layer of 100 nm Aluminum was first deposited onto the 100 μm thick Kapton using Physical Vapor Deposition (PVD) to act as the electrode layer. In order to maximize the triboelectrification process for efficient sensor performance, the selected materials should show the most distinguished ability to gain or refuse electrons [94]. According to the literature and based on the triboelectric series, Polyurethane shows a relatively high tendency to easily lose electrons while Kapton is highly potent to gain electrons [94]. Also, the tire is under a long-term cyclic load and the sensor is required to resist against bending motion without being permanently deformed. Both selected polymeric materials show excellent elasticity, which is proper for the proposed application [170, 171]. Besides, the dielectric materials were chosen so that they provide outstanding hardness at high temperatures as the tire undergoes relatively high temperatures under operating conditions [170, 171]. It should be noted that the use of Aluminum for the electrode is because Aluminum is a cost-effective, lightweight, temperature resistant, and highly-conductive material, which has been utilized as the electrode for various TENG applications [172, 173]. To apply surface roughness for increasing the effective contact area with the Polyurethane layer, fine grit sandpaper (2000#) was applied to the Kapton surface both horizontally and vertically for 100 cycles to form a rectangular-shaped surface texture at a very small scale. The processed Kapton layer was then washed with deionized water and isopropyl alcohol and dried out with Nitrogen gas. Subsequently, 1.5 mm thick Polyurethane was cut into the same dimensions of the Kapton layer, and similarly washed with deionized water and isopropyl alcohol, and then dried out using Nitrogen gun. Finally, the two short edges of the layers were adhered to each other to form the sandwiched structure of the flexible TENG sensor. Figure 4.5 shows the surface of both Kapton and Polyurethane before and

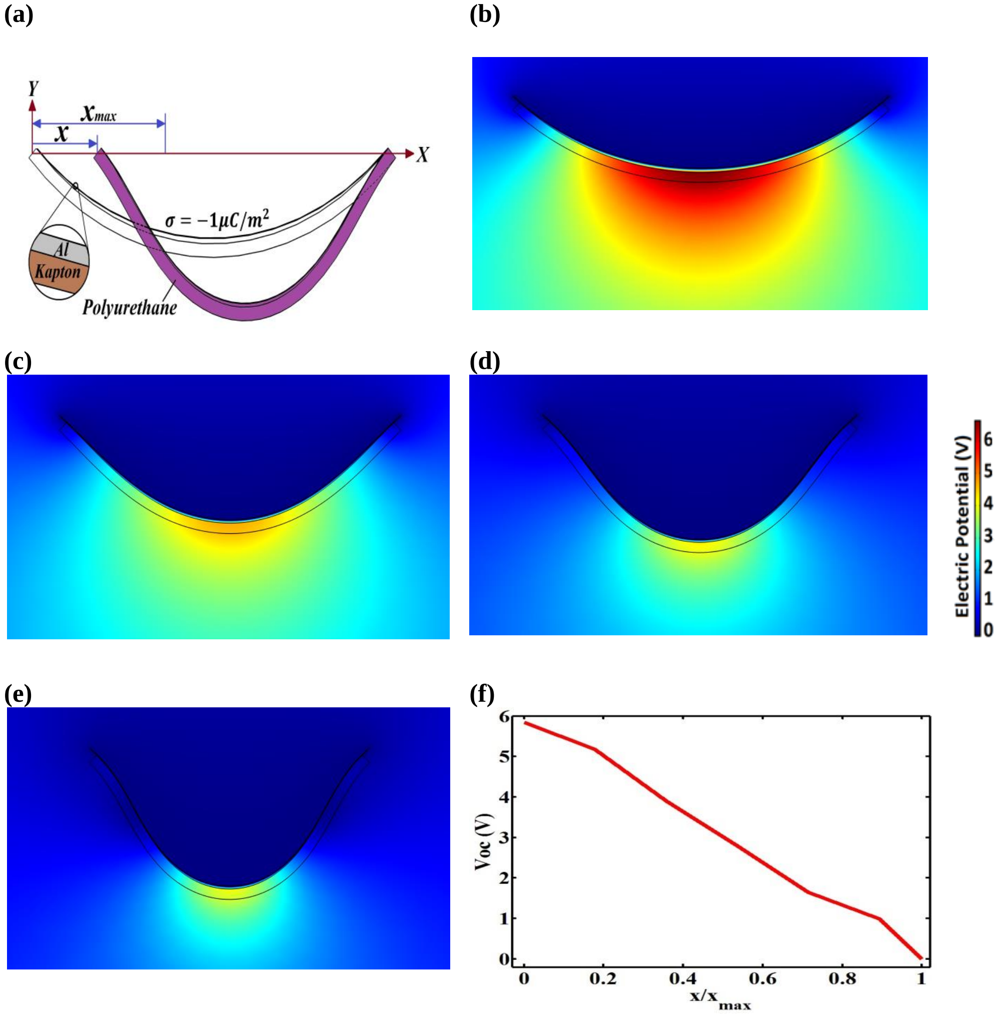

Figure 4.4: (a) FEA model of the sensor: (b)-(e) electric potential distributions for $x/x_{max} = 0, 0.3, 0.6, 1.$, (f) open-circuit voltage with respect to the relative displacement

after sanding with sandpaper grit #2000. The surface roughness has been characterized by means of a Scanning Electrode Microscope(SEM).

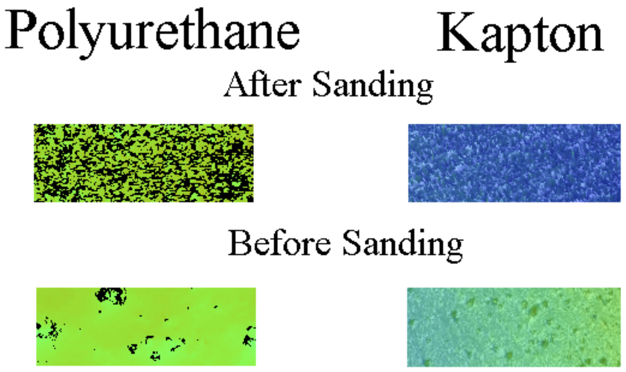

Figure 4.5: Surfaces of sensor before and after sanding with grit#2000

The sensor is attached to the sidewall of a tire as presented in Figure 4.6. More details related to the attachment is presented in Chapter 5.

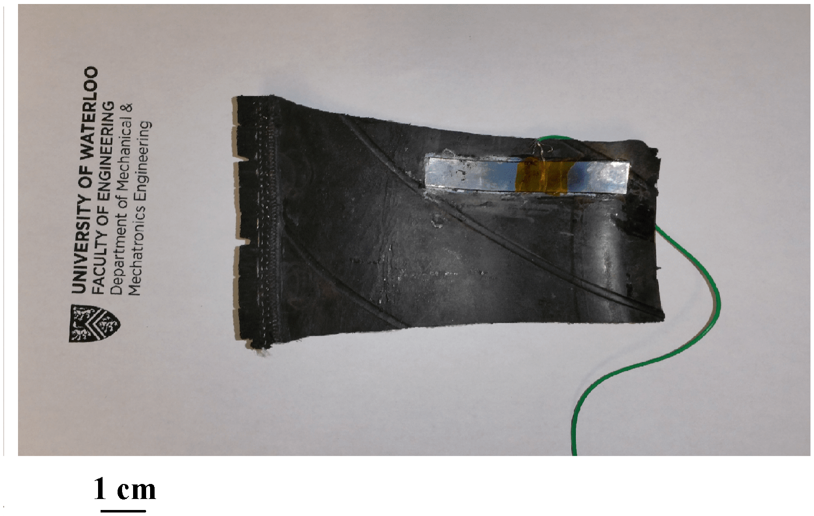

Figure 4.6: Top view of the sidewall of the tire with as-fabricated sensor

4.3 Flexible Sensor II

In this part, the second flexible sensor, designed for TCMS, is described. First, the design concerns and procedures are briefly discussed (Section 4.3.1). Then, working mechanism of the sensor is presented (Section 4.3.2). In Section 4.3.3, FEM analysis of the proposed flexible sensor is presented. The sensor fabrication procedure is discussed in Section 4.3.4.

4.3.1 Design

One of the main issues for the first flexible sensor is the rubber dust inside the tire. The rubber dust is small enough to enter between the layers of the sensor and decreases its sensitivity and accuracy. This leads to design a dust-free flexible sensor, which can fit to the harsh environment of the tire. Therefore, with using the same design presented in previous section, the sensor is fully covered with a heat shrink wrap. The other difference with the Flexible Sensor I is its size. This sensor is thinner and shorter than the first fabricated flexible sensor. The heat shrink has also high thermal durability. Heat shrink wrap is made of Polyolefin plastic, and it can withstand in a high temperature range, which covers -65 to 275 $^{\circ}F$. The sensor has a simple design as the layer of Kapton is located to one of the surfaces of Polyurethane. In addition, a thin electrical wire is attached to the surface of the electrode part of the sensor. The sandwiched form of the layers are located inside the heat shrink wrap. With heating the shrink wrap, the main body of the sensor is fully covered and tighten, which will make it a more proper sensor for TCMS.

4.3.2 Working Mechanism

When the sensor is bent, the two friction layers contact each other due to triboelectrification between the surfaces, equivalent negative and positive charges are generated on the Kapton and PU layers, respectively. During the releasing process of the sensor, positive charges will be induced on the electrode owing to the effect of electrostatic induction. As a result, electrons flow between the electrode and electrical ground due to the corresponding potential difference until reaching an electrical equilibrium. Similarly, the electrons flow back in a reverse direction as the sensor starts bending. The flow of electrons between the electrode layer and the electrical ground induces an alternative current through the external circuit resulting in electricity generation. Figure 4.7 depicts the working mechanism of the sensor based on the single-electrode mode TENG. When the Kapton and Polyurethane layers are brought into contact and slide over, electrostatic charges are generated on the surfaces owing to the triboelectrification. Figure 4.7(a) shows that the released condition of the sensor. As Figure 4.7(b) shows, when the sensor is bent, electrons will flow from the electrical ground toward the electrode owing to a potential difference. As indicated in Figure 4.7(c), the electrons motion continues until the maximum deflection and the electrical equilibrium is achieved. Similarly as the sensor is being released, the electrons will flow backward to the ground until reaching the fully released condition, as shown in Figure 4.7(d). Therefore, the cycle of bending and releasing the sensor will result in generation of an alternating electrical output because of the motions of electrons between the electrical ground and the sensor electrode.

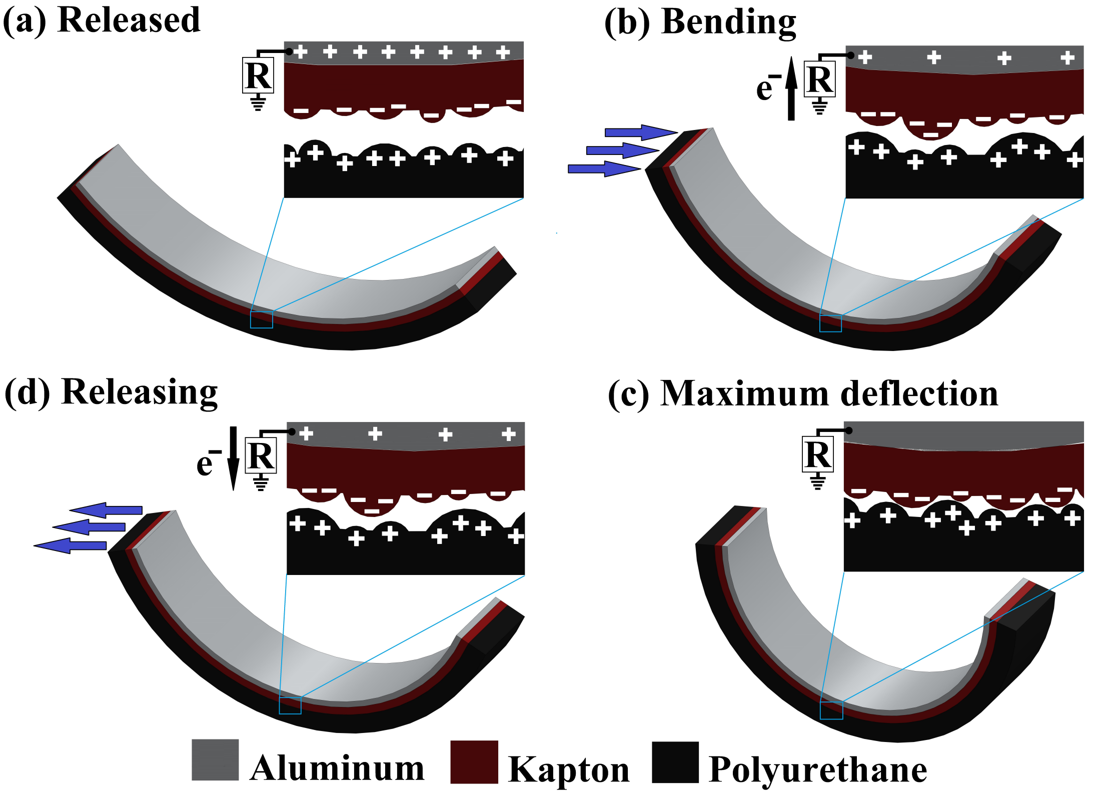

Figure 4.7: The schematic of the working mechanism of the sensor in one loading cycle

4.3.3 Finite Element Analysis

The sensor performance has been theoretically investigated using Finite Element Analysis (FEA) in COMSOL software. The performance of the sensor under a bending load was modeled, and corresponding potential charge distribution and open-circuit voltage (V_{oc}) were obtained when the sensor relative deflection x, was changed form $x = 0$ to $x = x_{max}$. It should be noted that a 2D simulation was considered owing to the small thickness of contact layers. Figures 4.8(a)-(d) illustrates the electric potential distribution when the sensor was bent from the released condition to the maximum deflection. It is obvious that as the deformation increases, the electric potential reduces owing to the further contact of the layers. The variation of generated open-circuit voltage (V_{oc}) between the electrode layer and electrical ground versus the relative deflection (x/x_{max}) was also calculated, as depicted in Figure 4.8(e). Accordingly, V_{oc} is gradually decreased by applying further deflection. Therefore, it is proved that the cycle of bending and releasing the sensor leads to the generation of electricity between the electrode and ground, which is considered as the sensor signal.

4.3.4 Sensor Fabrication

The triboelectric-based sensor is made of Kapton, Polyurethane and a heat shrink wrap as a cover, and a thin layer of aluminum as an electrode. The sandwiched-like sensor comprises a rectangular 1.5 mm thick Polyurethane layer and a 100 μm temperature resistant Kapton. The selection of the two materials is due to three main reasons: first, Kapton and Polyurethane are highly different in triboelectricity, which is useful for strong electric signal generation; second, both materials show excellent elasticity for the targeted application; third, the materials are reasonably temperature resistant owing to the presence of high temperatures in a tire under operating condition. A thin layer of Aluminum was deposited on the Kapton layer as the electrode using Physical Vapor Deposition (PVD). In order to maximize the triboelectrification process for efficient sensor performance, the selected materials should show the most distinguished ability to gain or refuse electrons. According to the literature and based on the triboelectric series, Polyurethane shows a relatively high tendency to easily lose electrons while Kapton is highly potent to gain electrons. Also, the tire is under a long-term cyclic load and the sensor is required to resist against bending motion without being permanently deformed. Both selected polymeric materials show excellent elasticity, which is suitable for the proposed application. The use of aluminum for the electrode is because aluminum is a cost-effective, lightweight, temperature resistant, and highly-conductive material, which has been utilized as the electrode for various TENG applications.

In order to increase the effective contact area between the Kapton and Polyurethane, a fine grit sandpaper (2000#) was applied to the Kapton surface both horizontally and vertically for 100 cycles to form a rectangular-shaped surface texture at a very small scale.

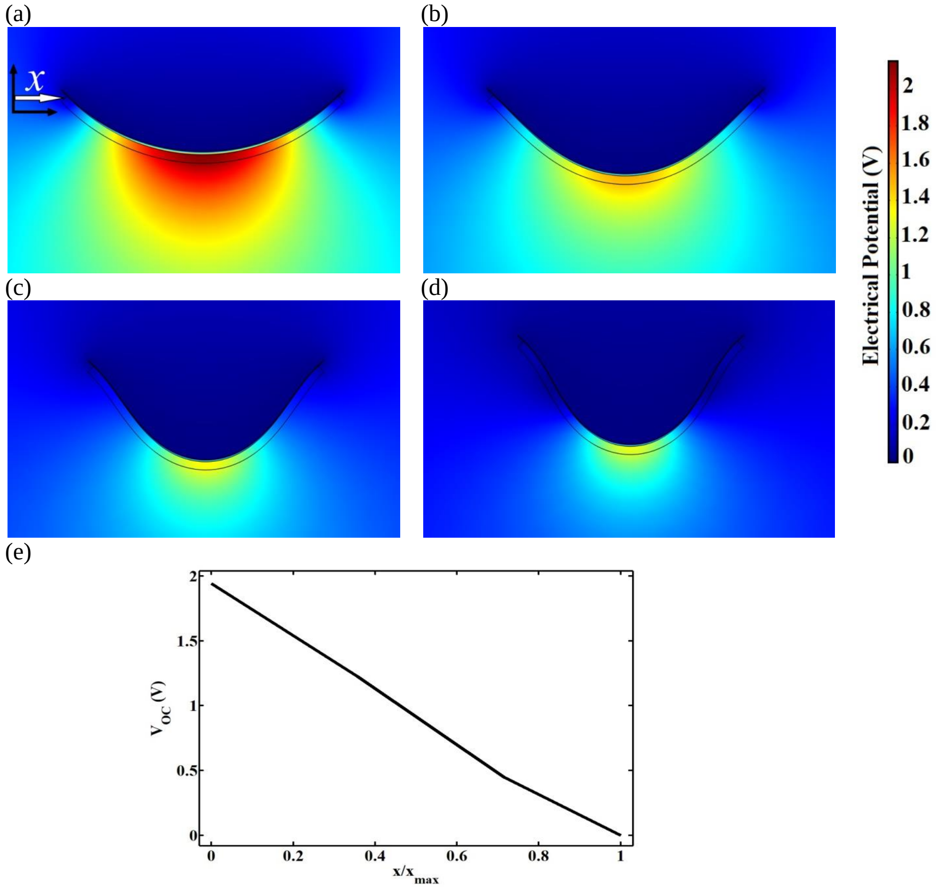

Figure 4.8: Results of the FEA simulation of the sensor: (a)-(d) electric potential distribution for different relative deflections, $\frac{x}{x_{max}} = 0, 0.3, 0.6, 1$.(e) open-circuit voltage versus the relative deflection

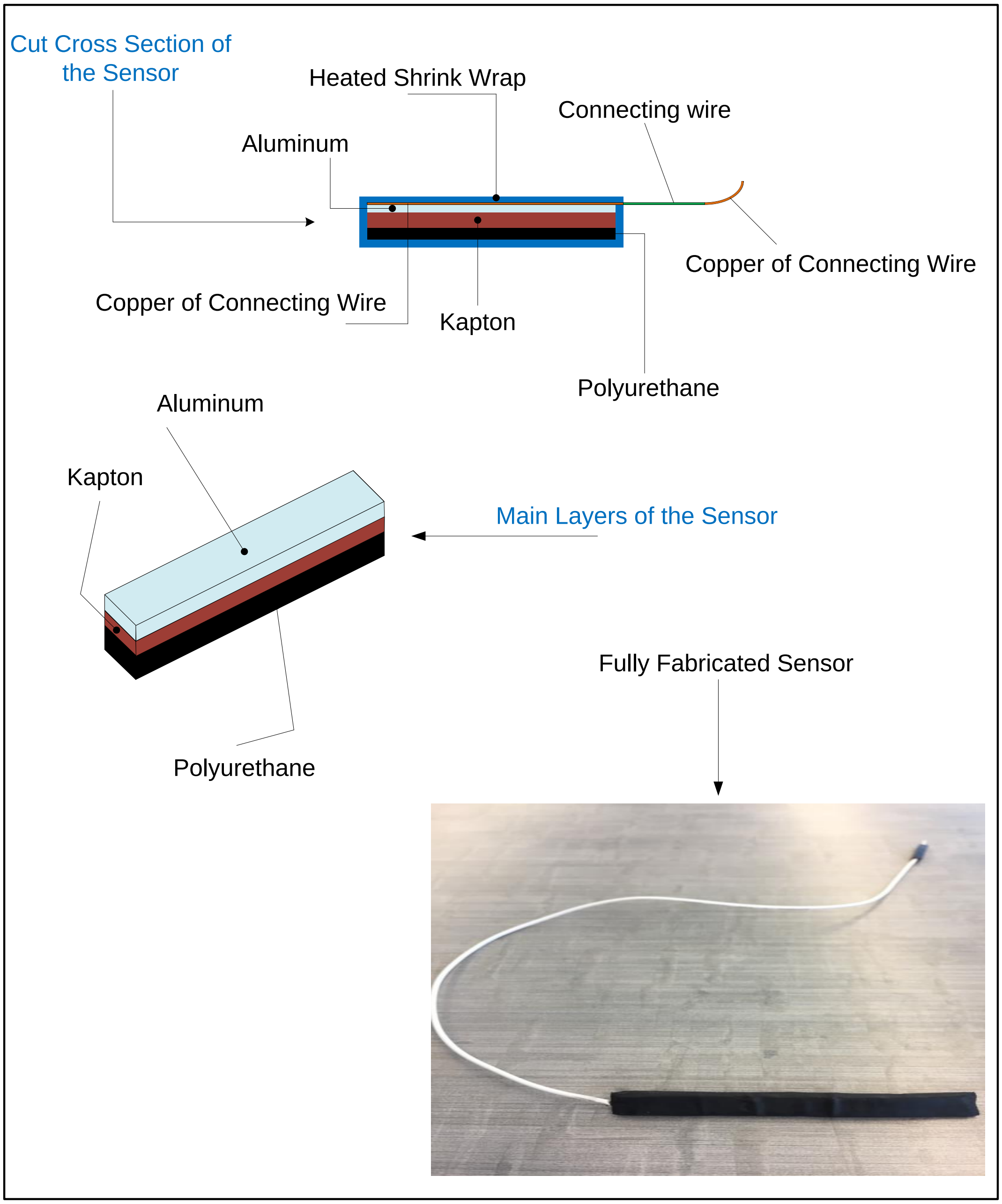

Figure 4.9: Flexible sensor II: configuration, schematic representation and a photograph of as-fabricated sensor

The processed Kapton layer was then washed with deionized water and isopropyl alcohol and dried out with Nitrogen gas. Subsequently, 1.5 *mm* thick Polyurethane was cut into the same dimensions of the Kapton layer, and similarly washed with deionized water and isopropyl alcohol and then dried out using Nitrogen gun. The layer of Kapton is located to one of the surfaces of Polyurethane. In addition, a thin electrical wire is attached to the surface of the electrode part of the sensor. Then, the layers of sensors are located inside the heat shrink wrap. Finally, the heat shrink wrap is heated to fully cover the sensor and tighten the layers of the sensor. Figure 4.9 shows different parts of the fabricated sensor. The fabricated sensor is a single electrode type TENG.

4.4 Flexible Sensor III

In this section, the last designed flexible sensor is presented (Section 4.4.1). First, the design criteria is presented for the sensor, and then its working mechanism is discussed (Section 4.4.2). Theoretical model of this sensor is discussed in Section 4.4.3. The finite element modelling and the sensor fabrication procedure are illustrated in Sections 4.4.4 and 4.4.5, respectively.

4.4.1 Design

In order to enhance the electrical output of the sensor, the third flexible sensor is designed with two electrodes. The used dielectric materials are the same, but copper is implemented as the electrode. The main reason of replacing Aluminum with copper is its its coefficient of thermal expansion, which is almost 40% greater than Copper. This can lead to clamping force that can promote creep in the sensor materials, as it undergoes thermal cycles. Similar to Flexible Sensor II, the sensor layers will be covered with heat shrink wrap. Generally, this sensor has a sandwich form, with two layers of electron on its top and bottom, two dielectric materials in between, and a flexible cover, which is a shrink wrap.

4.4.2 Working Mechanism

The working mechanism of the sensor operates based on the concept of double-electrode TENGs, depicted in Figure 4.10. The sensor is bent and released due to the applied force to the tire while contacting the ground in each cycle of the tire rotation. In the bending cycle, when the two polymer layers contact each other, equal negative and positive charges are generated on the Kapton and PU layers, based on the triboelectrification effect, Figure 4.10(a). When the sensor goes to releasing process, positive and negative charges will be induced on the electrodes due to electrostatic induction effect as depicted by Figure 4.10(b). Therefore, a current pulse occurs between the electrodes. After releasing the sensor, the induced potential difference is balanced as presented in Figure 4.10(c). In a similar process, the electrons flow back in a reverse direction as the sensor goes under the bending load as presented in Figure 4.10(d).

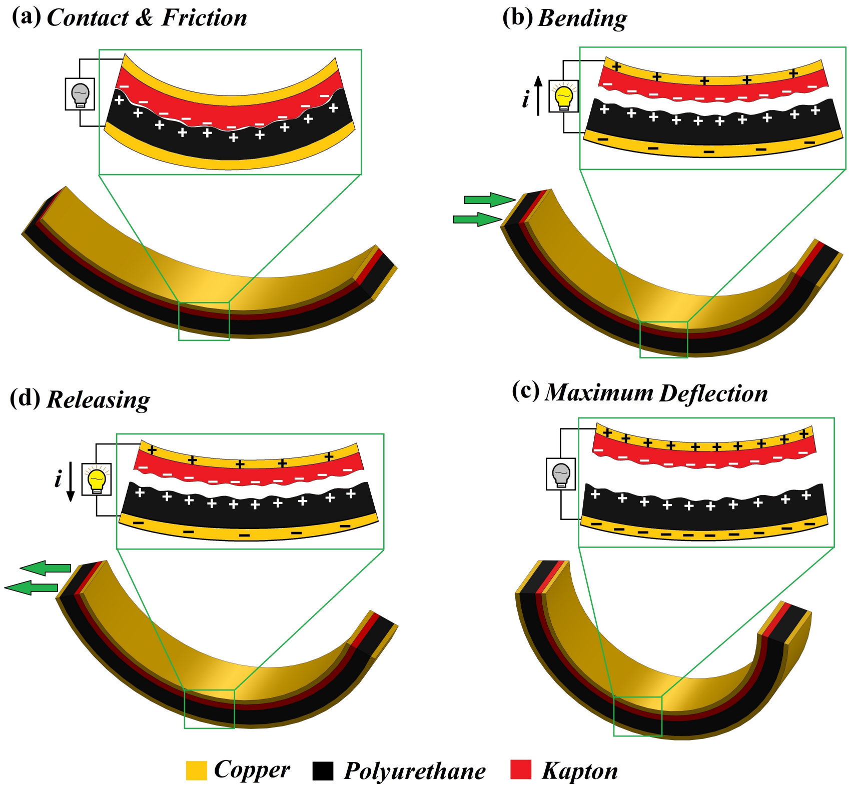

Figure 4.10: Working mechanism of the proposed flexible sensory device

4.4.3 Theoretical Model

As the sensor is a double electrode TENG, in this part, a general model is provided considering this type of TENG, which is the principal concept behind the last fabricated sensor. The fabricated sensor is considered as dielectric-to-dielectric mode, as presented in Figure 4.11.

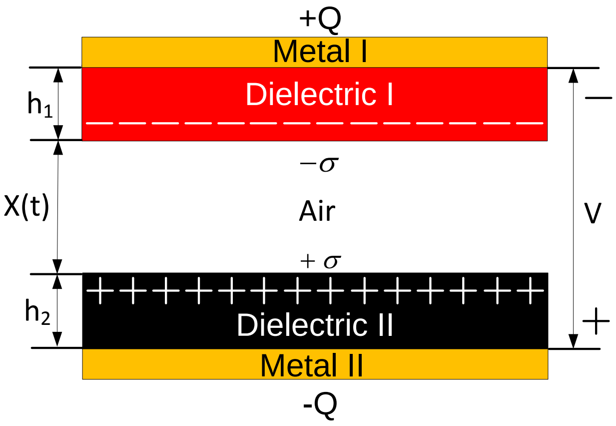

Figure 4.11: Theoretical models for dielectric-to-dielectric parallel plate TENG

The two dielectric plates of the sensor, with thicknesses of h_1 and h_2 and the relative dielectric constants ϵ_{r1} and ϵ_{r2}, respectively, are located face to face as two triboelectric layers. The two metal layers are attached/deposited on top faces of the dielectrics. The distance $x(t)$ between two dielectric layers can vary depending to the applied mechanical force. For the Flexible Sensor III, the distance between the layers are very tiny. After contacting the inner surface of the dielectric layers, they will have opposite static charges, with equal amount of density (σ). For the insulators, it is assumed that the triboelctric charges are uniformly distributed over their surfaces. A potential difference (V) will be induced between the two electrodes when the triboelectric layers become separated. The amount of transferred charges on two electrodes induced by the potential difference is called Q. Considering the minimum obtainable charge reference state, it is supposed that the instantaneous amount of the charges on the electrodes is Q and $-Q$. In order to provide a theoretical model for representing the electrical output generation of a TENG, it is necessary to define the relationship between the voltage V, the amount of transferred charge Q, and the distance between two triboelectric layers x. Taking into account the following assumption, a relationship can be formulated based on $V - Q - x$:

- For the experimental case, it is assumed that $h_1 + x(t) + h_2 \ll S^m$, where S^m is the area size of the metal. Therefore, considering that the electrode are infinitely large is a reasonable assumption.
- It is supposed that the electric field only has a perpendicular component to the surface inside the air-gap and the dielectrics.

- It is assumed that the charges are uniformly distributed over the inner surface of the metals.

Accordingly, using the Gauss theorem, the electric field strength can be found at each specific region. For inside Dielectric I, it can be written:

$$E_1 = -\frac{Q}{S^m \epsilon_0 \epsilon_{r1}}. \tag{4.1}$$

For the air, the the electric field strength is defined by:

$$E_{air} = \frac{-\frac{Q}{s^m} + \sigma(t)}{\epsilon_0}. \tag{4.2}$$

For the second Dielectric, one could have:

$$E_2 = -\frac{Q}{S^m \epsilon_0 \epsilon_{r2}}. \tag{4.3}$$

Therefore, the voltage between two electrodes can be found using the following relationship:

$$V = E_1 h_1 + E_2 h_2 + E_{air} x. \tag{4.4}$$

Finally, (V-Q-x) relationship can be obtained by the following equation:

$$V = -\frac{Q}{S^m \epsilon_0}\left(\frac{h_1}{\epsilon_{r1}} + \frac{h_2}{\epsilon_{r2}} + x(t)\right) + \frac{\sigma x(t)}{\epsilon_0}. \tag{4.5}$$

The effective thickness for all of the dielectric materials can be defined as:

$$h_o = \sum_{m=1}^{n} \frac{h_i}{\epsilon_{rm}}. \tag{4.6}$$

Taking into account the effective dielectric, the following formulation can be written for the (V-Q-x) relationship:

$$V = -\frac{Q}{S^m \epsilon_0}(h_o + x(t)) + \frac{\sigma x(t)}{\epsilon_0}. \tag{4.7}$$

Therefore, the following relations are obtained for V_{oc}, Q_{sc}, and C:

$$V_{oc} = \frac{\sigma x(t)}{\epsilon_0}, \tag{4.8}$$

$$Q_{sc} = \frac{S^m \sigma x(t)}{h_o + x(t)}, \tag{4.9}$$

and

$$C = \frac{\epsilon_0 S^m}{h_o + x(t)}. \tag{4.10}$$

4.4.4 Finite Element Modelling

Finite Element Model (FEM) is implemented to quantitatively study the performance of the proposed TENG sensor. COMSOL software is used to develop the finite element model. A 2D model is used as the thicknesses of sensors layers are much smaller than the sensor width. The working condition of the sensor, similar to the real case in tire, is based on bending and releasing process in each cycle.

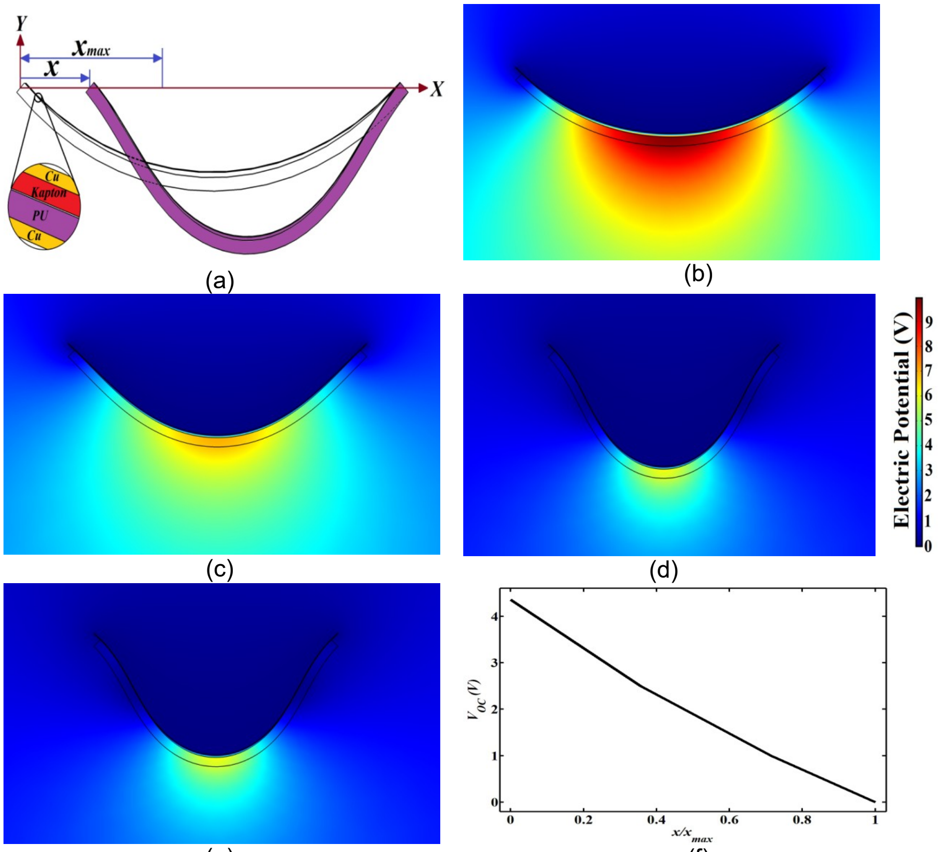

(a) (b) (c) (d) (e) (f)

Figure 4.12: (a) Schematic representation of the sensor , (b-e) finite element model for the sensor: electric potential distribution for $\frac{x}{x_{max}} = 0; 0 : 3; 0 : 6; 1$, (f) open-circuit voltage versus relative displacement

This simulation is developed to obtain the potential charge distribution and also open circuit voltage during each cycle. As depicted from Figure 4.12(a), the sensor is initially at its release condition $x = 0$, and then, after experiencing the bending deformation, it will reach to the maximum bending as $x = x_{max}$. In the modelling, it is assumed that PU and Kapton layers have the same amount of charges to maintain the charge conservation. The electric potential distribution is illustrated in Figures 4.12(b-e). Figure 4.12(b) represents the electric potential of the sensor when there is no bending load, and then, the bending load is gradually increased to reach the maximum deformation in the sensor (Figure 4.12(e)). Based on the simulation results, it is concluded that increasing the deformation of the sensor results in reduction of the electric potential. In fact, it happens as the effective contact layers further come in to contact. Once the sensor is fully released, the maximum distributed electric potential occurs. Figure 4.12 (f) represents the relation of relative displacement and open circuit voltage. Increasing the relative displacement reduces the generation of the open circuit voltage as shown by Figure 4.12 (f).

4.4.5 Sensor Fabrication

The structure of the proposed self-powered sensing system includes a thin layer of Kapton, a thin layer of Polyurethane, layers of copper as electrodes, and a heat shrink wrap as the cover of the sensor. Both Kapton and Polyurethane layers have copper on their top surfaces as an electrode. The fabricated sensor has a sandwich type structure in which the free surface of the kapton is located on the free surface of Polyurethane. Then, these two layers are covered by a heat shrink wrap. Heat shrink wrap is heated using a handheld heat gun to keep the polymer layers attached, and also to fully cover and tighten the core part of the sensor.

Using the heat shrink wrap results in the fabrication of a sandwich based structure sensor, which is encapsulated, highly flexible and thermally durable. All of these characteristics make this sensor an ideal candidate for tire condition monitoring applications. In the next chapter, an experimental analysis is provided to investigate the potential of five different fabricated sensor for power harvesting and self-powered sensing considering TCMS. Figure 4.13 shows the cut cross section of the sensor, schematic configuration, and optical image of the fabricated Flexible Sensor III.

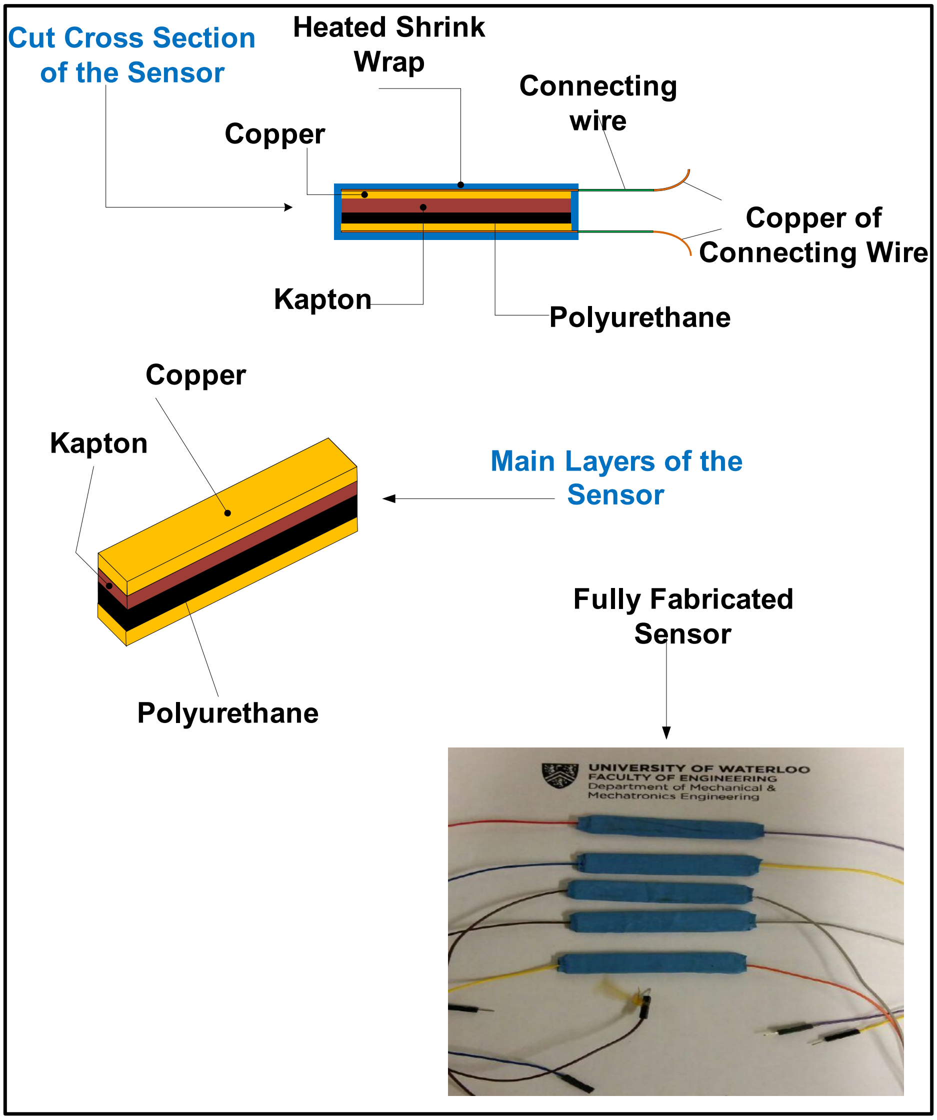

Figure 4.13: Flexible Sensor III: configuration, schematic representation and a photograph of as-fabricated sensor

4.5 Concluding Remarks

Three different types of flexible TENG based sensors were developed for TCMS. The first flexible fabricated sensor operates based on single electrode mode. One of the main issues with this design was its sensitivity to rubber dust in a tire. Therefore, an encapsulated single electrode TENG-based sensor was developed using heat shrink wrap. The working mechanisms, finite element modelling, and the fabrication procedure of each of the sensors were fully illustrated. In order to enhance the electrical output of the second designed flexible sensor, an encapsulated double electrode flexible TENG sensor was developed as the last sensory device for TCMS. Copper was used as the electrode of this sensor to increase its durability. Similarly, the working mechanism, finite element modelling, and the fabrication procedure of this sensor were fully discussed as well as a principal theoretical modelling. As stated, the main aim is to locate these sensors inside a tire for TCMS. It should be noted that with locating these sensors inside the tire, they will experience a very harsh environment, dirt and grim from the tire and even physical obstructions. Therefore, it is highly needed to test these sensors taking into account all of these hostile conditions. In the next two chapters, the potential of all proposed sensors is investigated for real-world condition, considering the concerns pertinent to the harsh environment of the tire including wide range of temperature and forces, lifetime, durability, and possible pressure variation.

Chapter 5

Experimental Results and Discussion

In this chapter, an extensive laboratory experimental results are provided to show the capability of fabricated devices. Section 5.1 fully presents the experimental setup, results and analysis for both of the fabricated hybridized sensors. A general performance analysis is presented to show the capability of the developed hybridized sensors. In Section 5.2, a comprehensive experimental results and discussion are provided for the developed flexible nanogenerators. Their electrical output under different excitation conditions are investigated, and their potential for tire-condition monitoring is discussed.

5.1 Hybridized Generators

In this section, a comprehensive experimental analysis is provided on the designed hybridized generators to assess their energy harvesting and sensing potential. In the next section, the experimental setup and equipment are fully presented. Section 5.1.2 shows the output of the Hybridized Sensor I. In Section 5.1.3, the electrical output of the Hybridized Sensor II is described.

5.1.1 Experimental Setup

The implemented experimental instruments for testing the fabricated hybridized sensor are presented in Figure 5.1. As indicated, the experimental setup includes four main parts:

mechanical excitation system, data acquisition,the fabricated hybridized sensors, and electrical circuits. In addition, a displacement sensor is needed to measure the oscillation's amplitude of the shaker depending on the excitation frequency and amplitude of the function generator. The mechanical excitation part contains a function generator (Agilent 33220A), an amplifier (LDS PA 2000), and a shaker (LDS V722). The LDS V722 shaker can operate in the frequency range of 5-4000 Hz with a random or sine wave profile.

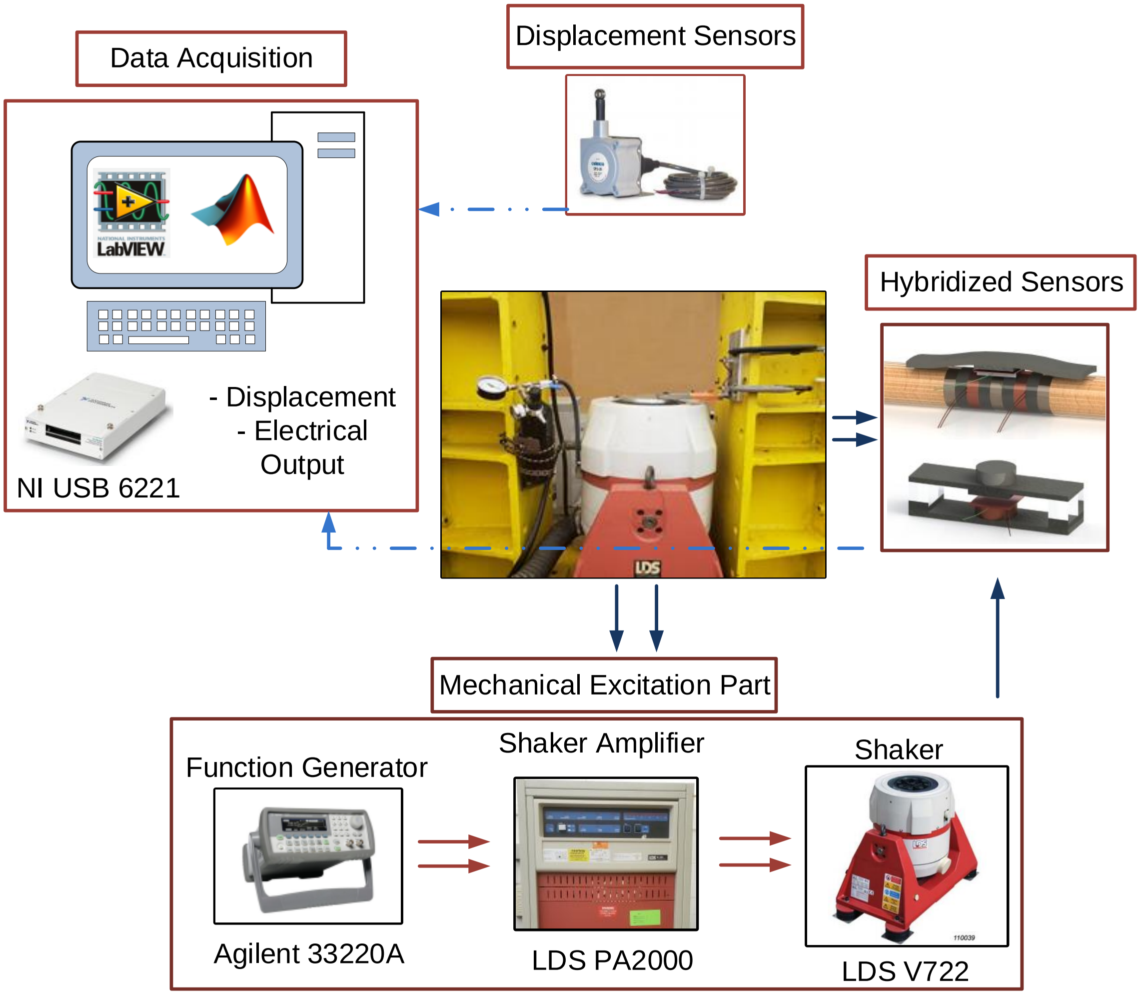

Figure 5.1: The experimental instruments used for testing the electrical output of the fabricated hybridized sensors

The function generator (Agilent 33220A) is used to control the excitation frequency and the amplitude of the shaker. The data acquisition includes a PC, Windows real time target app in MATLAB, and NI USB 6221 DAQ to directly measure the electrical output of the hybridized sensors when they are mechanically excited with the shaker. A variable resistor is also used in the circuit connected to the sensors to investigate the effect of resistance on the electrical output of the sensor, and to find the optimal resistance for the highest possible power harvested from the hybridized sensors.

In order to test the Hybridized Sensor I, it is hold with a clamp on top of the shaker similar to a cantilever beam. Then, a rigid bar is glued from one side to the tip of the sensor, and from the other side to the shaker. Once the shaker is excited, the mechanical force is transferred to the sensor through the rigid connection, and it bends, similar to possible bending in tire when it goes to contact patch. This mechanical bending in the sensor is converted to the electrical output through the EMG and TENG units. The Hybridized Sensor II is attached to the shaker. Once the shaker is excited, the top part of the sensor bends due to inertia. Increasing the excitation amplitude of the shaker enhances the displacement of top part of sensor. This periodical displacement results in induction of the current into the coil and periodically contacting the lower layer of TENG unit, which results in electrical voltage generation. The next section presents the experimental results pertinent to Hybridized Sensor I.

5.1.2 Hybridized Sensor I

This section provides the experimental results and detailed illustration about the outputs of Hybridized Sensor I. Figure 5.2(a) shows the open circuit voltage of the EMG component for a single stack device. As the figure shows, by increasing the frequency of excitation from 0.5 Hz to 10 Hz, the open circuit voltage increases from 0.2 mV to approximately 1.5 mV. Figure 5.2(b) represents the sensitivity of the system to the angular amplitude of oscillations. As indicated by the figure, increasing the angular amplitude of excitation at the tip of the sensor, increases the open circuit voltage. In Figure 5.2(b), the shaker's amplitude of excitation is converted to the angular deformation based on Figure 3.13. As the figure shows, the fabricated device is highly sensitive to the angular motion, and a very small angular change results in voltage generation in EMG component.

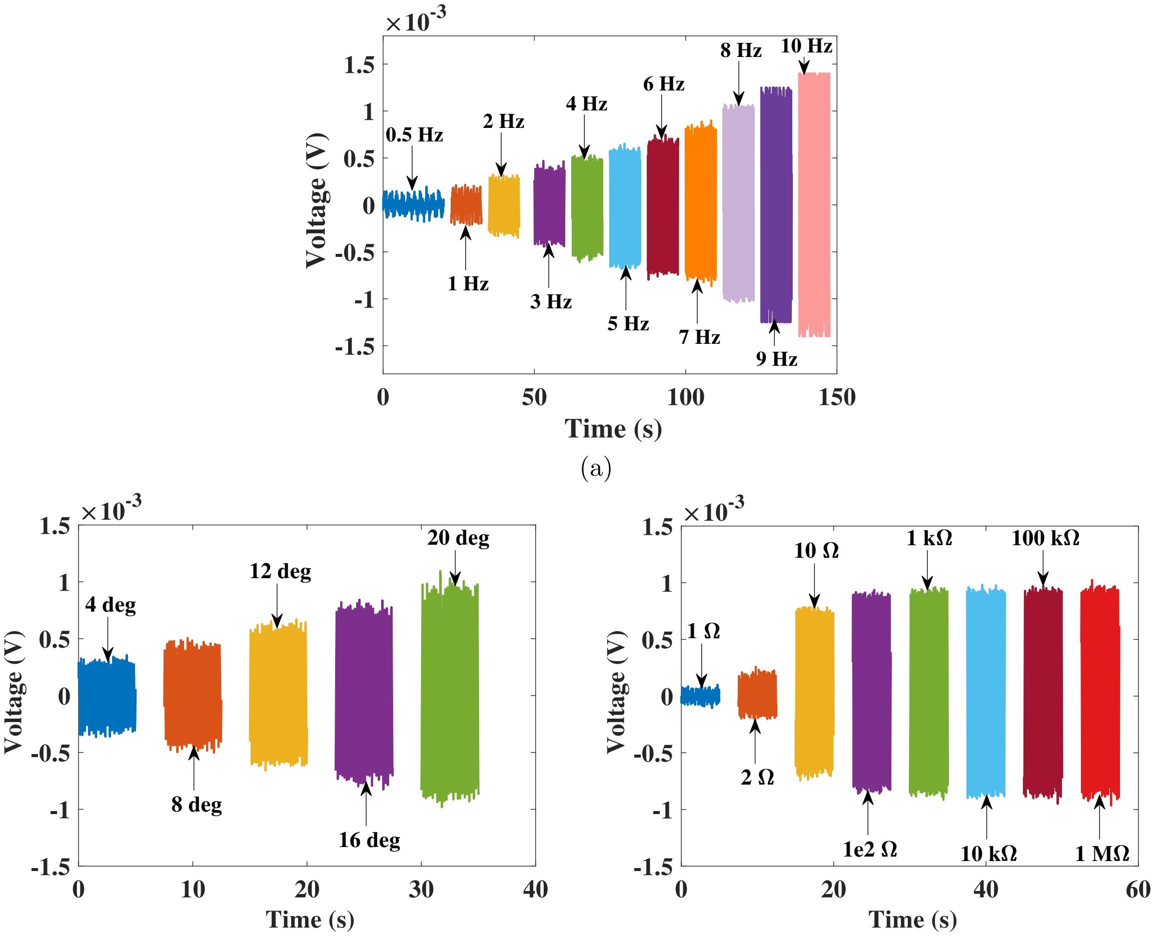

(a)

(b)

(c)

Figure 5.2: Open circuit voltage of the EMG component-single stack (a) effect of triggering frequency (b) effect of angular amplitude of excitation, ($\theta = 4, 8, 12, 16, 20$ degrees) (c) effect of resistive load on the open circuit voltage

Figure 5.2(c) illustrates the effect of external resistive load on the EMG component of the single stack device. As expected, increasing the external resistive load enhances the open circuit voltage.

The electrical output of the system with a double stack EMG component is also investigated. Figure 5.3(a) illustrates the influence of the amplitude of excitation on open circuit voltage of the left coil of the double stack EMG component of the sensor. Figure 5.3(b) represents the effect of the angular amplitude of excitation on open circuit voltage for the right coil of the double stack EMG component. Enhancing the angular amplitude of excitation, increases the open circuit voltage of both coils.

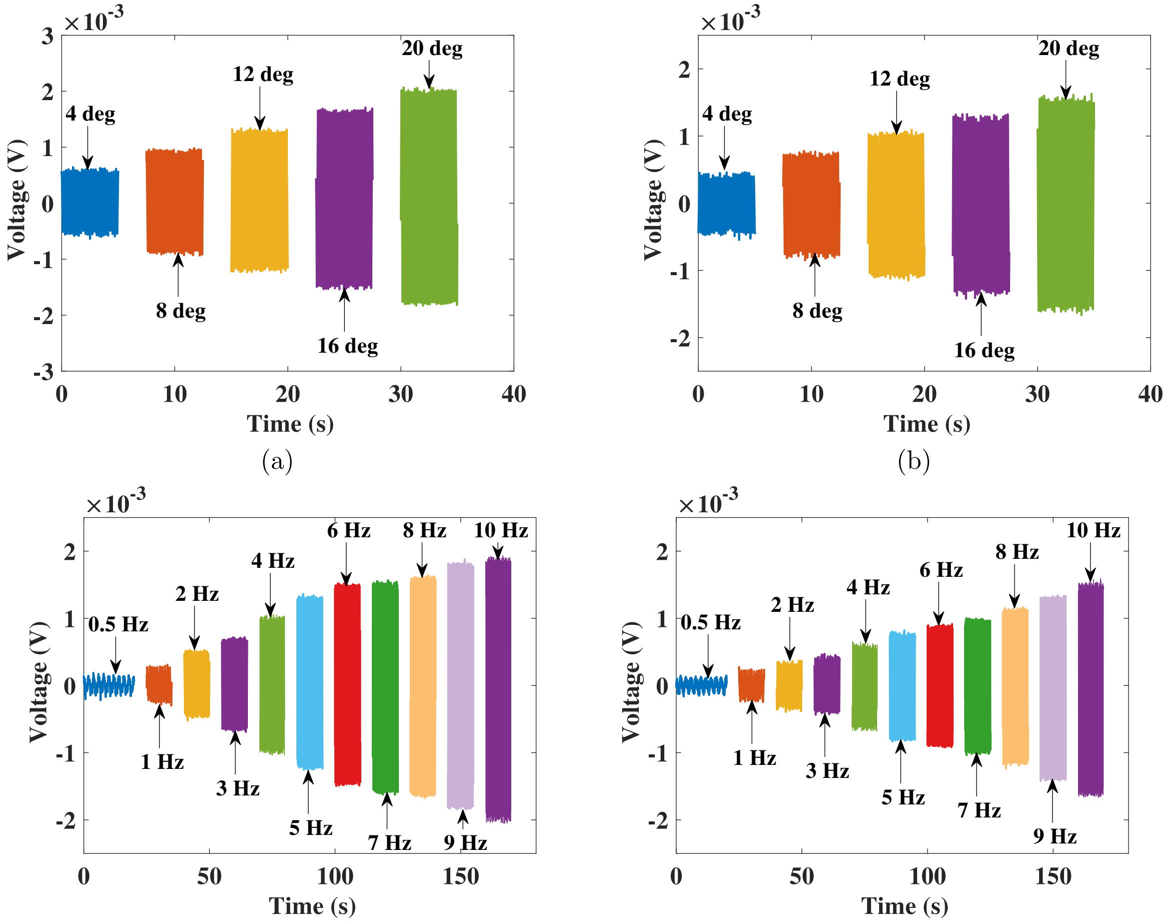

(a) (b)

(c) (d)

Figure 5.3: Effect of angular amplitude of excitation on open circuit voltage of the EMG component-double stack for ($\theta = 4, 8, 12, 16, 20$ degrees) (a) left coil (b) right coil; effect of triggering frequency on open circuit voltage of the EMG component-double stack (c) left coil (d) right coil

As evidenced by both figures, the highest open circuit voltage for the left coil is approximately 2 mV, and 1.5 mV for the right coil. Accordingly, a double stack of the EMG component can generate approximately 3.5 mV. A single stack of EMG component of the device can approximately deliver 1 mV open circuit voltage as depicted in Figure 5.2(b). It shows that adding one magnet and one coil to a single stack EMG unit and creating a double stack system results in increasing 250 % in the electrical output.

Figure 5.3(c) presents the effect of excitation frequency on the open circuit voltage of the left coil. As the figure shows, increasing the excitation frequency from 0.5 Hz to 10 Hz results in increasing the open circuit voltage from approximately 0.15 mV to 1.9 mV.

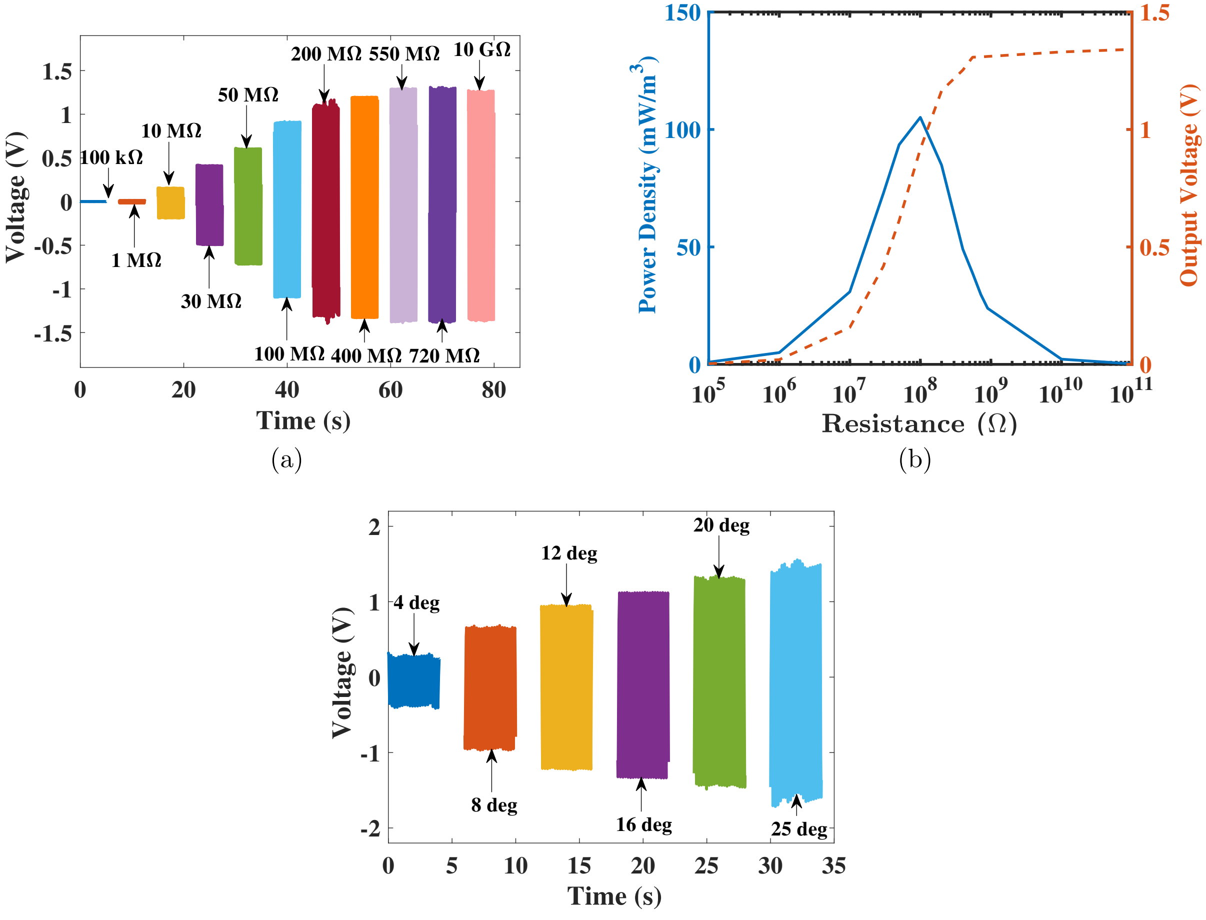

(a)

(b)

(c)

Figure 5.4: Electrical output of the TENG components, (a)effect of resistive loads on open circuit voltage between 10^5 to $10^{10}\Omega$, b) output power and open circuit voltage versus resistive loads, (c) effect of angular excitations ($\theta = 4, 8, 12, 16, 20, 25$ degrees) on TENG performance

Similarly, Figure 5.3(d) shows the influence of excitation frequency on the open circuit voltage of the right coil. As expected, increasing the frequency of excitation results in enhancing the open circuit voltage.

Figure 5.4(a) describes the effect of external resistive load on the output voltage of the TENG component of the device. As expected, by increasing the resistive load, the output voltage of the device increases to reach its open circuit voltage. Figure 5.4(b) shows the effect of external resistive load on the output voltage and power density of the TENG unit. As depicted by the figure, there is an optimum value for resistance in which the highest power can be harvested from the TENG unit. Figure 5.4(c) illustrates the effect of angular amplitude of excitation on open circuit voltage of TENG unit of the fabricated device. The angular amplitude of excitation varies between 4 to 25 degrees. As depicted by figure, increasing the angular amplitude enhances the open circuit voltage of the TENG component.

5.1.3 Hybridized Sensor II

This section investigates the performance of the Hybridized Sensor II considering the effect of the external resistive load, amplitude of the deflection, the frequency of excitation for all of the components of the sensor. The performance of the sensor has been studied in both general and also tire-condition monitoring application. In order to characterize the capability of the sensor, the electrical output of the sensor is experimentally obtained. In each set of experiments, EMG and TENG components, which are being tested, are shunted with a variable external resistance. All of the voltage data are collected via MATLAB Windows real time target toolbox using an NI-6221 DAQ. The displacement is measured using a Celessco SP2 string potentiometer. A LDS 722 shaker is employed to excite the sensor at different frequencies and amplitudes. The shaker is adjusted to apply sinusoidal displacement using a 33220 Agilent function generator. Figure 5.5 shows the electrical output of the EMG component of the sensor. Figure 5.5(a) represents the effect of frequency on the open circuit voltage of the EMG component. As indicted, increasing the frequency results in enhancing its open circuit voltage. Figure 5.5(b) represents the effect of amplitude of excitation. As the shaker amplitude of excitation increases, the voltage of the EMG component increases. Figure 5.5(c) depicts the effect of external resistance on the performance of the EMG components. As expected, increasing the external resistance results in increasing EMG component voltage.

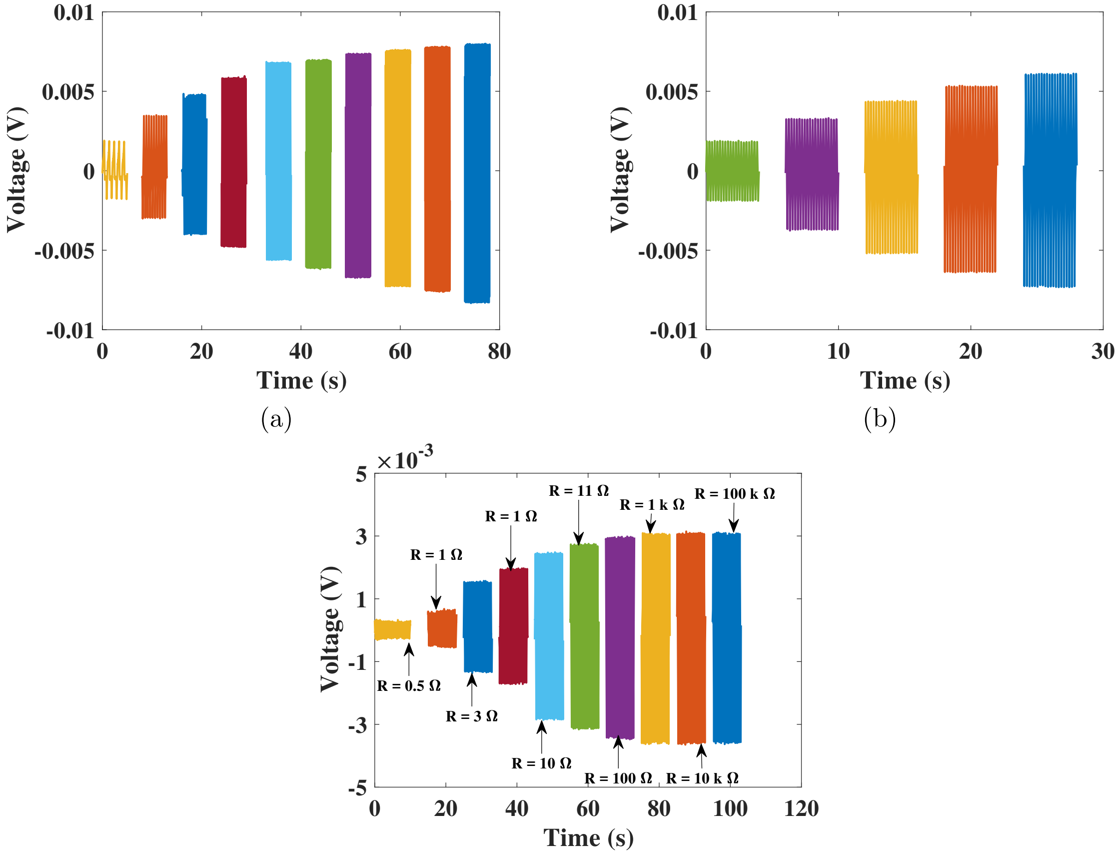

(a)

(b)

(c)

Figure 5.5: Electrical output of the sensor; round PM and coil: (a) the effect of frequency on open circuit voltage, (b) the effect of amplitude of excitation on open circuit voltage, (c) the effect of external resistance on open circuit voltage

A similar study is performed on the proposed self-powered sensing system with square shape coil and PM. Figure 5.6 (a) shows the influence of excitation frequency on the open circuit voltage of the sensor with square shape coil and PM. As the frequency of excitation increases, its corresponding voltage enhances. Figure 5.6 (b) represents the effect of excitation amplitude on the voltage of the system. As shown in Figure 5.6 (b), the open circuit voltage increases with increasing the excitation amplitude. The shaker is turned off and turned on to evaluate the sensor performance for this case, as indicated in Figure 5.6(c). What stands out in the Figure 5.6(c) is the durability of the EMG component. As presented, the sensor voltage comes back to its original performance after it is turned on again.

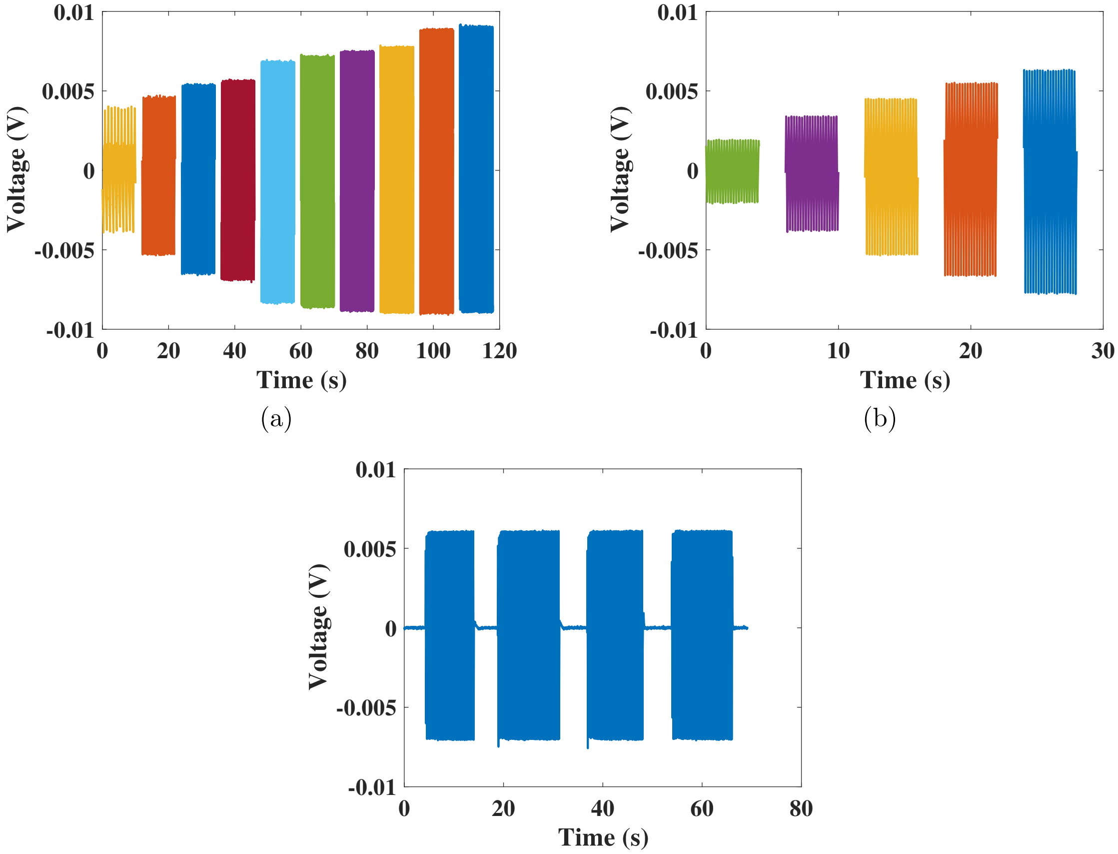

(a)

(b)

(c)

Figure 5.6: Electrical output of the sensor; square PM and Coil: (d) the effect of frequency on open circuit voltage, (e) the effect of amplitude of excitation on open circuit voltage, (f) durability test(Turn on-off)

Figure 5.7 (a) represents the effect of frequency on the maximum open circuit voltage for square shape coil and PM. As indicated in figure, by increasing the frequency from 1 Hz to 9 Hz, the open circuit voltage increases from 4 mV to 9.1 mV. Similar study is performed for the sensor with round shape coil and PM, as represented in Figure 5.7 (b). From the figures, it can be observed that the sensor with square shape has a higher electrical output comparing with the round shape. Figure 5.7(c) illustrates the variation of the power density for the EMG component. As depicted by Figure 5.7(c), the power density increases with increasing the external shunted resistance and reaches its zenith when the external shunted resistance equals to the coil resistance.

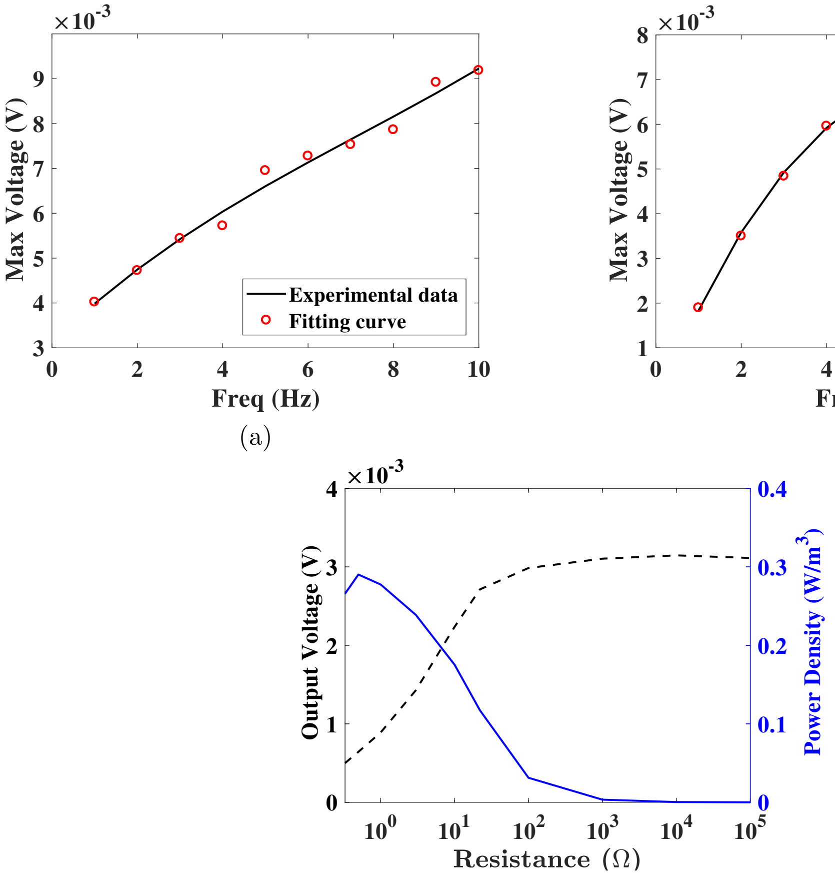

(a) (b)

(c)

Figure 5.7: The effect of frequency on maximum voltage of the EMG component:(a) with square PM and coil, (b) with round PM and coil, (c) power density and output voltage versus external resistance

Figure 5.8 shows the performance of TENG component of the sensor. In order to evaluate the durability of the TENG component, The shaker is turned off and turned on again to evaluate the sensor durability performance, as indicated in Figure 5.8(a). Figure 5.8(b) shows the effect of the amplitude of the shaker's excitation on the open circuit voltage of the sensor. As the shaker's excitation increases, the amplitude of open circuit voltage increases for the TENG component. Figure 5.8(c) represents the influence of the external shunted resistance on the performance of the TENG component. As depicted by Figure 5.8 (c), increasing the resistance results in enhancing the open circuit voltage of the TENG component.

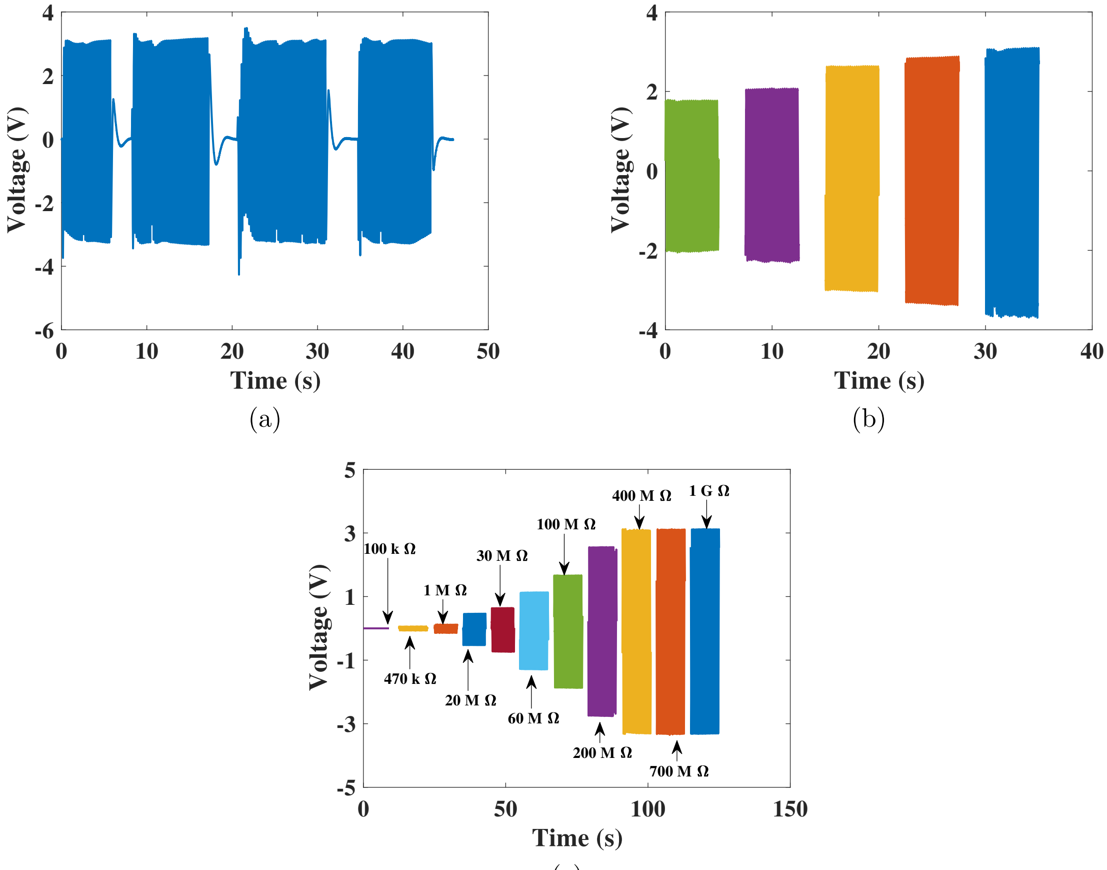

(a)

(b)

(c)

Figure 5.8: The electrical output of the sensor-TENG component (a) durability test (turn on-off) (b) effect of the amplitude of excitation on the open circuit voltage, (c) effect of external resistance on open circuit voltage

Figure 5.9(a)-(b) show the open-circuit voltage and current of TENG component. These two figures illustrate the effect of amplitude of oscillations on TENG performance. As depicted by figures, increasing the amplitude of oscillations enhances the open-circuit voltage and the electrical current. Figure 5.9(c) illustrates the variation of the power density for the TENG component. By increasing the external resistance, both output voltage and power density of the TENG component increase. Power density starts decreasing right after its maximum point at the optimal shunted resistance.

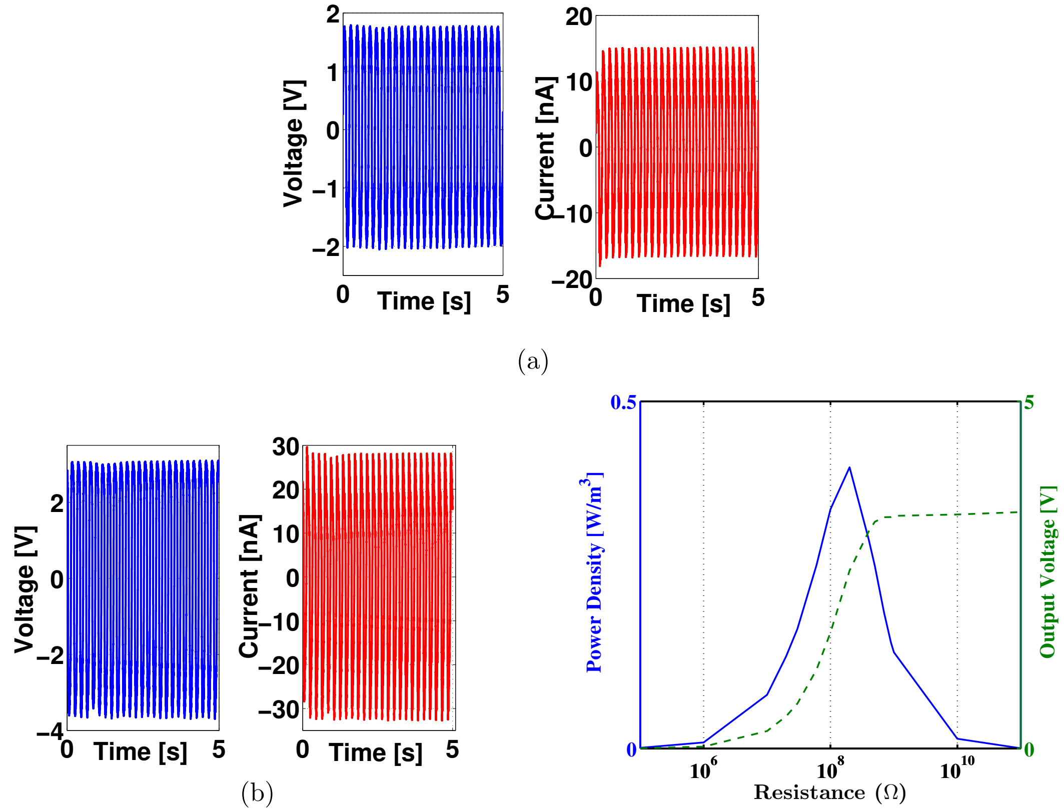

(a)

(b)

(c)

Figure 5.9: (a) Open circuit voltage and current-TENG component for the smallest and the highest amplitudes of excitation, respectively; (b) power density and open circuit voltage versus external resistive load

5.1.4 Tire Condition Monitoring

In this section, the performance of the proposed system is investigated as a sensor for tire condition monitoring. The sensor is attached to the sidewall of the tire, as shown in Figure 5.10(a). In order to trigger the attached sensor, a periodic force is applied with a crank-slider mechanism along with a rotating crank, a connecting rod and a reciprocating slide as represented in Figure 5.10(b). Figure 5.10(c) shows the open circuit voltage and electrical current of the EMG component of the attached sensor. As indicated, a clear and illustrative signal is obtained based on the EMG component. The peak-peak open circuit voltage and electrical current of the EMG component are about 5.2 mV and 10 mA, respectively. Figure 5.10(d) shows the open circuit voltage and electrical current obtained from the TENG component of the attached system. As illustrated in the figure, the peak-peak open circuit voltage and short circuit current for the TENG component is about 3.2 V and 25 nA. The results of these two figures represent a high potential of the fabricated sensor for tire condition monitoring.

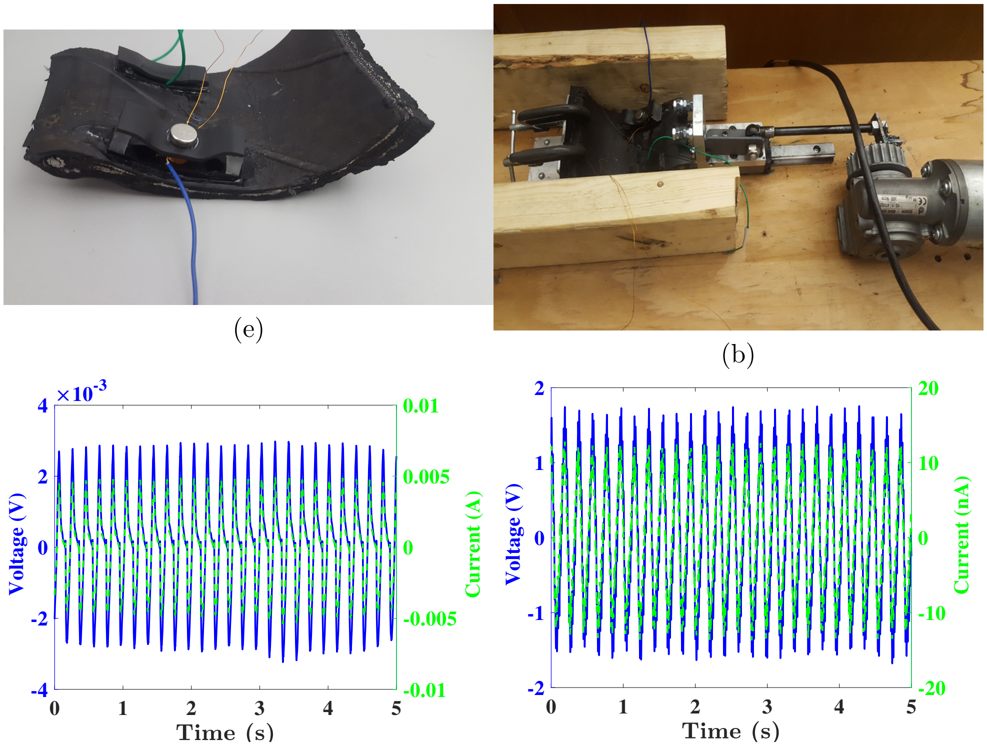

(e) (b)

(c) (d)

Figure 5.10: In tire: (a) side-wall of the tire along with the attached sensor, (b) experimental setup (c) open circuit voltage and current of the EMG component (d) open circuit voltage and current of the TENG component

Comparing with the previously published articles, the flexibility and also stiffness of the device comes from the structure of the system, and therefore, it does not require a spring to provide the stiffness. This helps to reduce the extra cost and also the weight of a spring [174]. Comparing with Refs. [175, 176], the proposed device of the present research operates based on the contact-separation mode. In addition, it has more flexibility in comparison with the proposed self-powered device in Ref. [175].

5.2 Flexible Generators

In this section of the chapter, the experimental results of the fabricated flexible generators are presented. In the next section, the developed experimental setup for the flexible sensors is illustrated. Then, the experimental results related to the Flexible Sensor I are shown in 5.2.2.

5.2.1 Experimental Setup

The experimental setup developed for the flexible sensors is based on a crank-slider mechanism. It contains a connecting rod with rotating crank and a reciprocating slider. To compress the tire sample, the slider contacts and compresses it. This will lead to the desired deformation. The implemented crank is actually a part of the 15:1 ratio worm gearbox assembly on the electric motor. Figure 5.11(b) shows a photograph of the testing machine with a tire sample. In order to have a parallel radial direction with respect to the reciprocating slider axis, the tire sidewall is cut as depicted in 5.11(b). Adhesive material is used to bond the flexible generators to the tire sidewalls. Figure 5.11(a) schematically represents the experimental setup for the flexible generators. It contains a crank slider mechanism, a power supply to adjust the frequency of actuation, and measurement apparatus similar to presented setup discussed in Section 5.1.1. Figure 5.11(c) represents a cut-cross section of a tire, and also, Flexible Sensor I attached to the the sample of tire side-wall. A similar configurations are used for Flexible Sensor II and Flexible Sensor III. It must be noted that a cut section of the well-used tire is used for the experiments. In fact, a well-used tire is used for all of the experiments, since it can be considered as a representative of typical tires on actual vehicles in highway service.

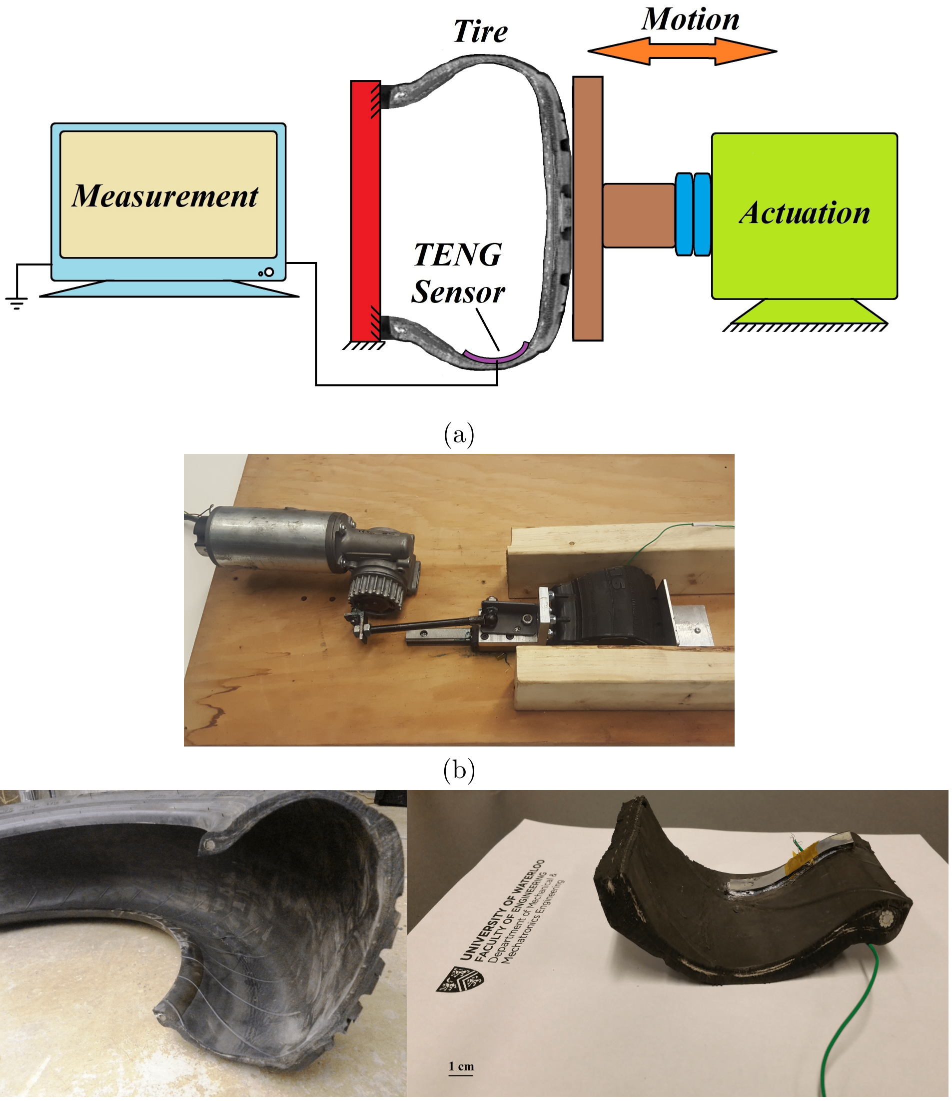

(a)

(b)

(c)

Figure 5.11: Experimental test setup: (a) schematic representation, (b) top view of bench testing machine with tire sample, (c) cross section of the used tire and its corresponding sidewall with the attached TENG sensor

5.2.2 Flexible Sensor I

Figure 5.12(a-b) show the side and top views of the side-wall of the tire with the attached Flexible Sensor I, respectively.

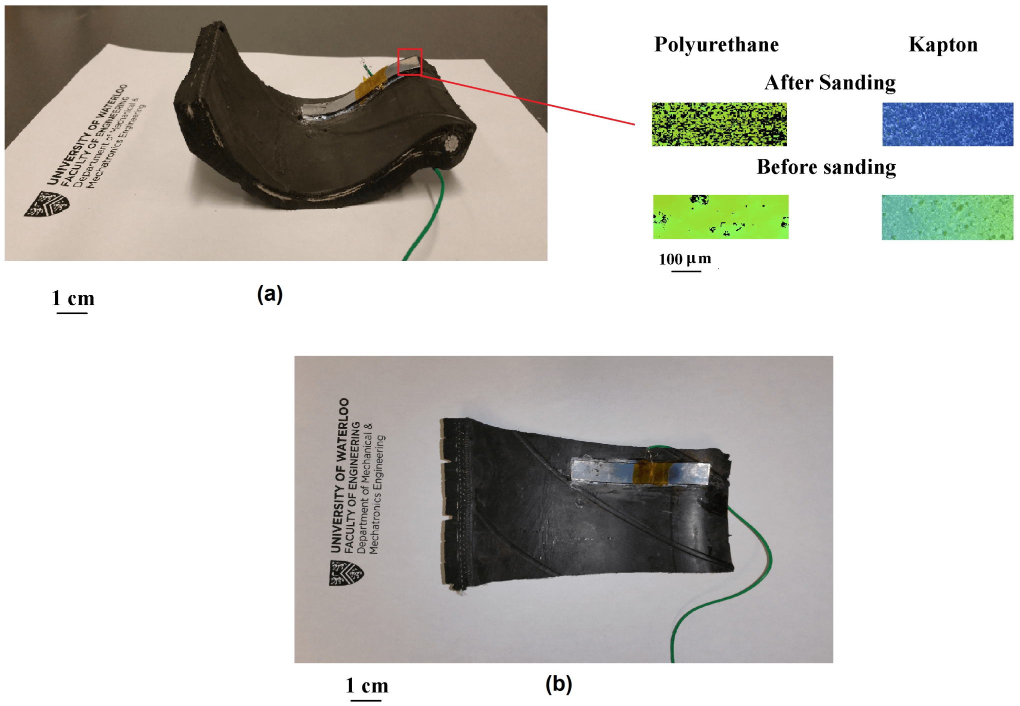

Figure 5.12: Sidewall of the tire with attached sensor (a) side view, (b) top view

The electrical output of the sensor is tested under different excitation condition. Its performance is investigated for different amplitudes of excitation, frequency and also external resistive load. Each set of experiment provides the electrical output of the sensor when it is shunted to an external resistance. All of the experimental data are collected via MATLAB windows real target toolbox using NI-6221 DAQ.

Figure 5.13 represents effect of the operating frequency of the rotation on the output voltage of the sensor. As indicated by Figure 5.13, increasing the frequency enhances the output voltage.

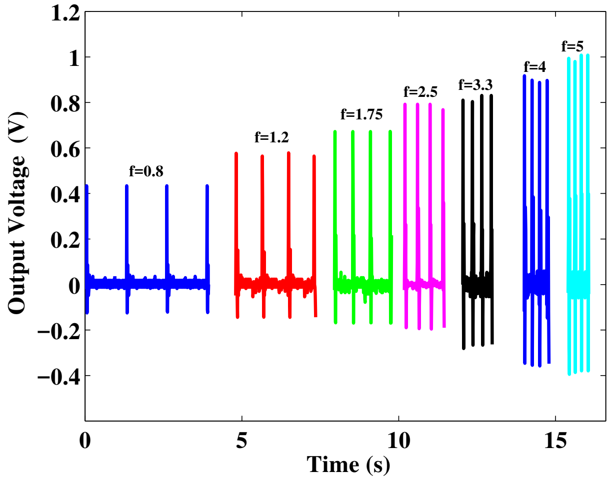

Figure 5.13: The effect of triggering frequency f (Hz) on output voltage of the sensor: the range of frequency variation is 0.8-5 Hz and the stroke displacement is 35 mm.

It must be noted that Figure 5.13 represents the output voltage when an external resistance is shunted to the circuit. The output voltage increases because it is equivalent to the shunted resistance times the electrical current. It is known that TENG's electrical current increases with increasing the frequency of excitation;so, the output voltage increases. This shows the high potential of the device for both energy harvesting and also sensing inside the tire. Therefore, when a driver increases the vehicle's speed, output voltage and generated power are increased. Figure 5.14(a) also depicts the effect of frequency on the peak to peak output voltage. As expected, increasing the triggering frequency results in increasing the output voltage. Figure 5.14(b) shows the effect of tire speed on the voltage. Again, an increase in the tire speed results in enhancing the output voltage. In order to convert the triggering frequency to the tire speed, the following mathematical formulation is used:

$$C = 2\pi R, \tag{5.1}$$

and

$$T = C/v, \tag{5.2}$$

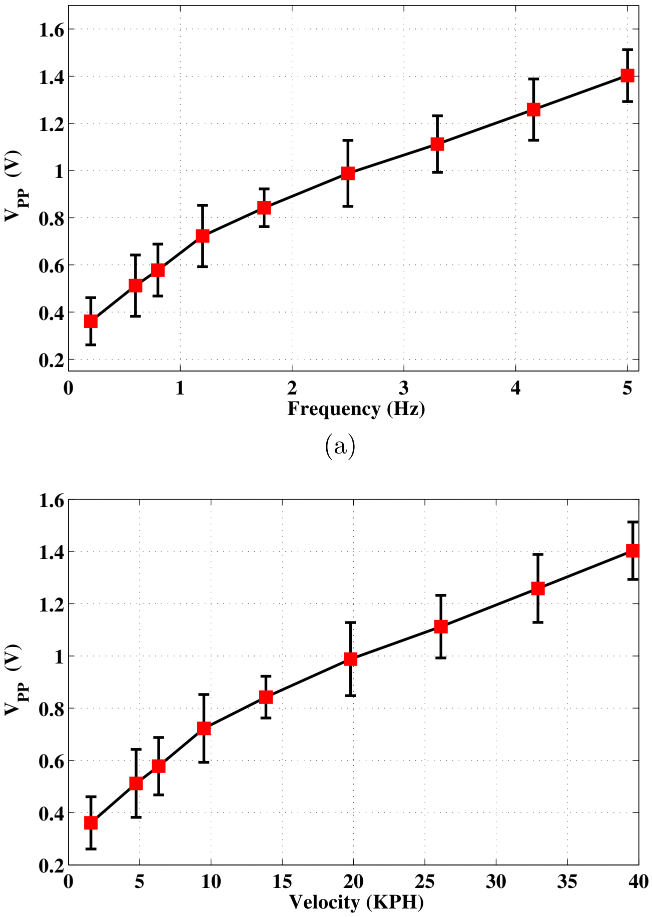

(a)

(b)

Figure 5.14: (a) The effect of operating frequency on the peak-peak voltage of the TENG sensor, (b) effect of the car velocity on the peak-peak voltage of the TENG sensor (stroke displacement of 35 mm).

where C refers to the circumference of the tire, and T is the time per wheel revolution. R is the radius of the tire. The variation of open circuit voltage with respect to the stroke displacement of the bench testing machine is shown in Figure 5.15. In fact, this figure can be considered as an indication of the normal force based on the open circuit voltage. Apparently, the higher normal force in tire results in more deformation in tire sidewall. Based on the experimental setup, the higher displacement in tire sidewall can be applied by increasing the stroke displacement of the bench testing machine. Accordingly, the more deformation in the tire sidewall occurs with the higher stroke displacement of the testing machine. In order to investigate the effect of pressure, a pre-deformation is applied to the sample test, which means that the tire has a lower pressure comparing to the case with higher pressure because of more deformation in the normal direction. As indicated in Figure 5.15, dashed blue line, a higher voltage is obtained when the system has a pre-deformation.

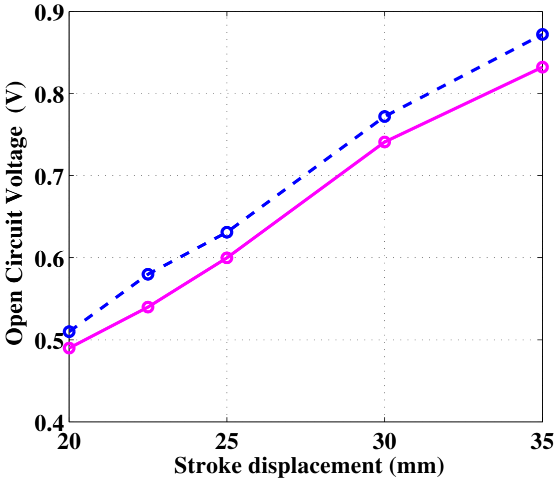

Figure 5.15: Open circuit voltage versus stroke displacement with frequency of 4 Hz

Figure 5.16 represents the influence of the external resistance on the generated output voltage and current. The output voltage of the self-powered sensing system rises, as the external resistance increases to reach a plateau, as indicated in Figure 5.16. There is an optimal resistance in which the system has the highest power density, which coincides with the intersection of output current and the voltage presented in Figure 5.16.

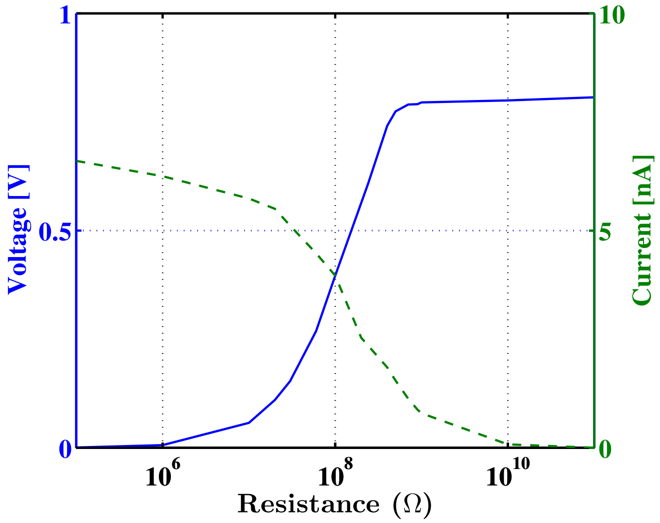

Figure 5.16: The effect of resistance on output voltage and output current

The durability of the fabricated sensor is also examined for 120 minutes, and an excellent durability and consistent output voltage are observed from the attached TENG sensor, as shown in Figure 5.17. In the durability experiment, 35 mm stroke displacement is considered for the testing machine, which is equivalent to 17 mm displacement for the sidewall of the tire based on Ref. [53]. After applying numerous cyclic loads on the sensor, it is observed that the output is highly stable even after number of excitation. Besides, the adhesion of thin film Aluminum to Kapton using physical vapor deposition method (PVD) is reliable enough. Accordingly, the aluminum can withstand against rupture even under high mechanical loads as illustrated in the reference [177].

The idea and the proposed concept of this section will be improved with developing two other flexible sensors, which will be discussed in the next sections.

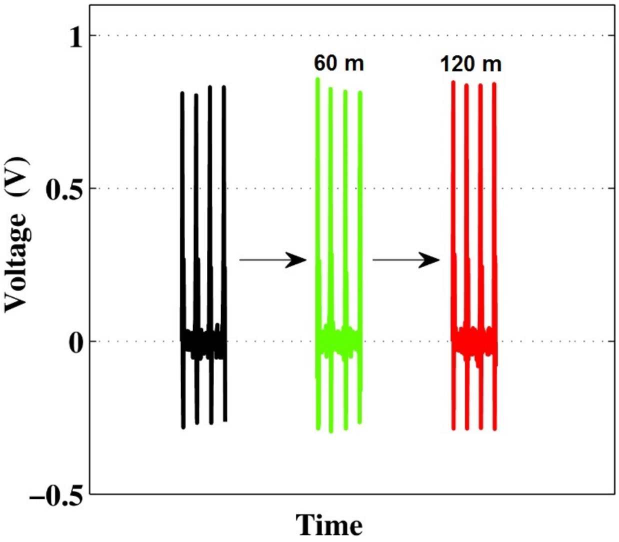

Figure 5.17: Durability test results of the sensor, (the figure shows the output signal of the sensor after 120 minutes of operation- triggering frequency of 4 Hz and stroke displacement of 35 mm)

5.2.3 Flexible Sensor II

The second flexible sensor, presented in previous chapter, contains the same layers as Flexible Sensor I with a heat shrink wrap as a cover. In addition, the size of the sensor is less than the Flexible Sensor I. With wrapping the sensor, it can be used under different loads to generate electrical voltage including bending, twisting and also pressing. The performance of the sensor is tested under different types of mechanical loads, as presented in Figure 5.19. The first test for this sensor is to show its sensitivity to the finger pressure. Three different pressing loads with finger is applied to the sensor to assess its performance under pressing loads. In Figure 5.19(a), from left to right signals, a finger load is applied to the sensor, and then released. As depicted by figure, by increasing the finger pressure, the generated electrical voltage increases. This shows the high potential of this sensor for pressure sensing. Figure 5.19(b) represent the effect of bending load to the electrical output generation of the sensor. As the figure shows, increasing the bending load increases the electrical voltage generation. In addition, the sensor is tested under twisting loads, and obtained a similar results are found as those obtained based on pressing and bending loads. With increasing the twisting loads, the electrical output of the sensor increases as presented in Figure 5.19(c). Based on the results presented in figures 5.19(b-c), peak to peak voltages of Flexible Sensor II for the bending and twisting loads can reach up to 8.5 Volts.

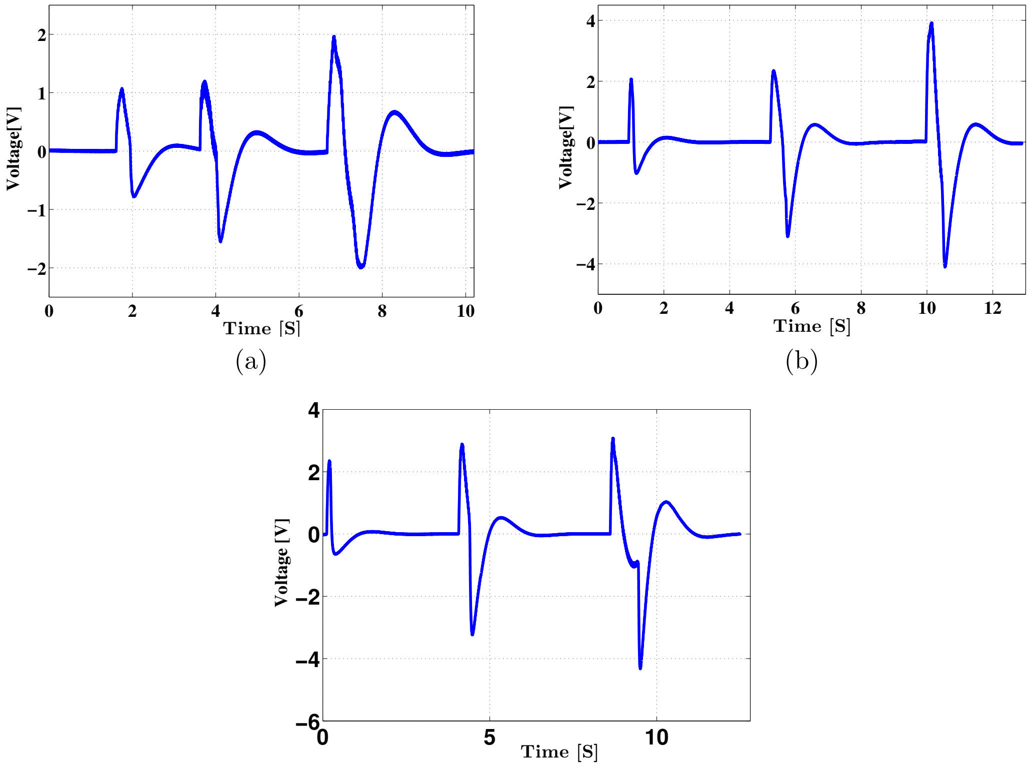

(a)

(b)

(c)

Figure 5.18: Different types of mechanical loads and their effects on the sensor performance (a) variation of finger pressure and its effect on the electrical output of the sensor, (b) electrical output when bending loads is applied to the sensor, (c) electrical output of the sensor under twisting excitation

The performance of the sensor is also investigated considering different mechanical stimuli with changing the excitation amplitude and frequency using the second experimental setup shown in Figure 5.11(b). Figure 5.19(a) shows the effect of frequency of excitations on the open circuit voltage of the Flexible Sensor II. As expected, increasing the frequency of excitations has no effect on the open circuit voltage of the proposed TENG-based sensor. The frequency of excitation is changed between 2 to 6 Hz. A durability test is also performed on the sensor. The sensor has shown a very solid behavior for about 80 minutes durability test as shown in Figure 5.19(b). Figure 5.19 (c) represents the effect of external resistance on the output voltage of the sensor. As the external resistance is increased from 10 $M\Omega$ to 1 $G\Omega$, the electrical output gradually increases to reach to the value of open circuit voltage. A set of thermal durability test was also conducted on this sensor, which will be presented in Appendix B.

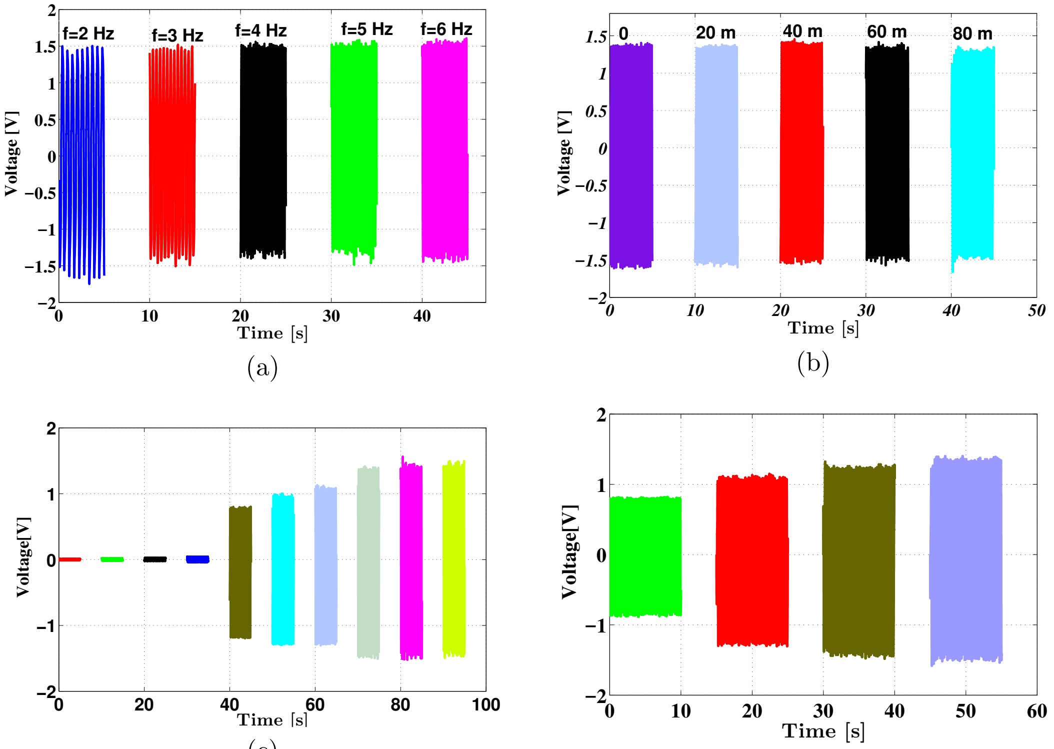

(a)

(b)

(c)

(d)

Figure 5.19: Sensor electrical performance: (a) the effect of the frequency of excitation on the sensor open circuit voltage, (b) sensor output in 80 minutes durability test, (c) the effect of external resistance on the electrical output of the sensor, (d) the effect of amplitude of excitation on the performance of the sensor

Figure 5.19(d) shows the effect of amplitude of excitations on the open circuit voltage of the Flexible Sensor II. As the figure represents, by enhancing the amplitude of excitations, the generated open circuit voltage of the sensor increases. It means that by increasing the bending load on the sensor, the generated voltage of the sensor increases. In terms of application in tire, as the force increases in the tire, the generated signal of the sensor enhances.

5.2.4 Flexible Sensor III

In order to enhance the electrical performance of the Flexible Sensor II, Flexible Sensor III is designed, modelled and fabricated. A similar set of tests are performed to evaluate the performance of the sensor under different types of mechanical loads. Figure 5.21 shows the performance of the sensor under different types of mechanical loads. From left to right signals, based on Figure 5.21(a), three pressing and releasing loads were applied to the sensor. As depicted by figure, as the finger pressure is enhanced, the generated electrical voltage enhances. This shows the high capability of this sensor for pressure sensing. Comparing with Flexible Sensor II, it has a higher electrical output, as it is expected. Figure 5.21(b) reveals the influence of bending loads to the electrical output generation of the sensor. Again for the bending load case, the output of the Flexible Sensor III, which is a double electrode sensor, is higher than the Flexible Sensor II, which is a single electrode TENG based sensor. For the twisting loads, by increasing the twisting loads, the electrical output of the sensor increases as presented in Figure 5.21(c). Similar to other load cases, Flexible Sensor III shows a higher electrical output for twisting type of external load.

In order to show the capability of the Flexible Sensor III, its performance is also studied under different types of mechanical loads with changing amplitude and frequency of excitations, and the external resistance, as presented in Figure 5.20. Figure 5.20(a) shows the effect of bending load on the generated open circuit voltage by the sensor. As the figure shows, increasing the amplitude of bending load increases the open circuit voltage. Figure 5.20(b) represents the effect of frequency of excitation on the open circuit voltage of the Flexible Sensor III. As depicted by figure, increasing the frequency of excitations has no effect on open circuit voltage.

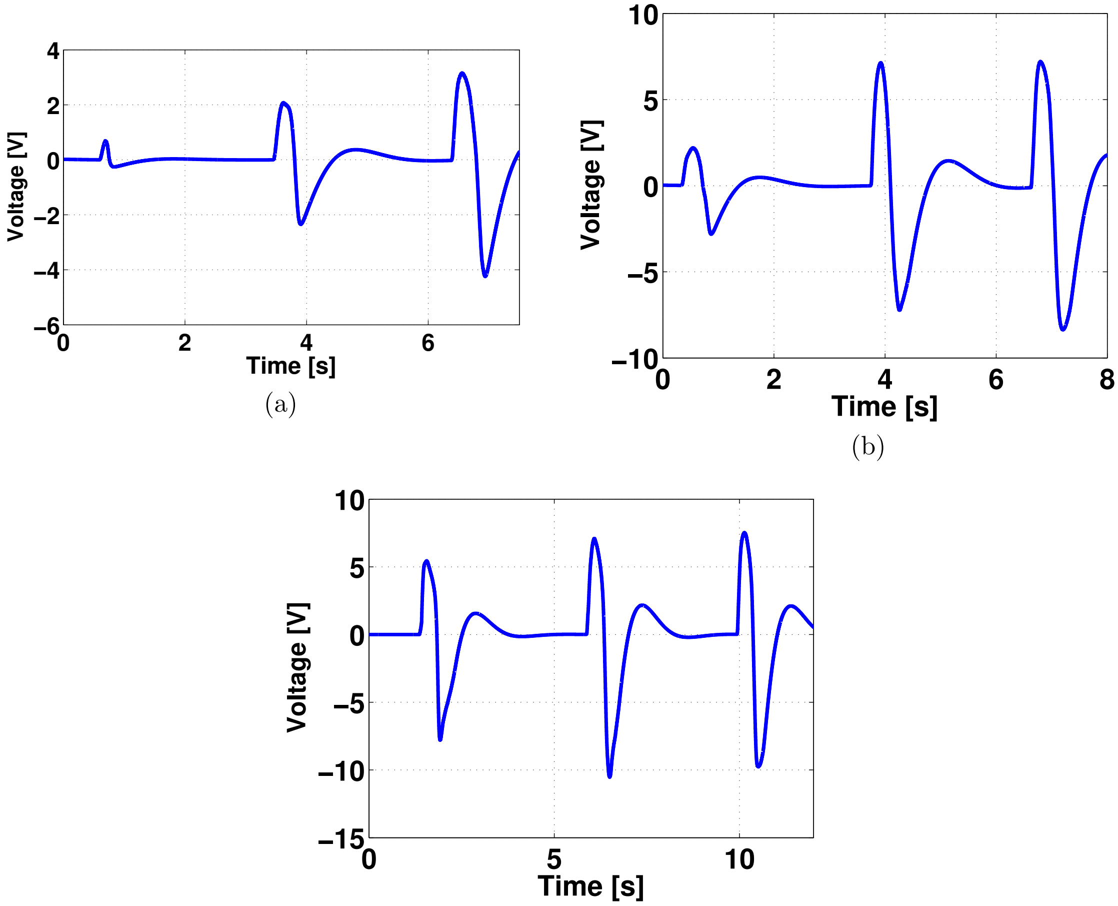

(a)

(b)

(c)

Figure 5.20: Different types of mechanical loads and their effects on the sensor performance (a) variation of finger pressure and its effect on the electrical output of the sensor, (b) electrical output when bending loads is applied to the sensor, (c) electrical output of the sensor under twisting excitations

Figure 5.21(c) reveals the effect of external resistance on the output voltage of the sensor. The external resistance is changed between $1M\Omega$ to $1G\Omega$. As the external resistance enhances, the output voltage of the sensor increases until reaching to open circuit voltage.

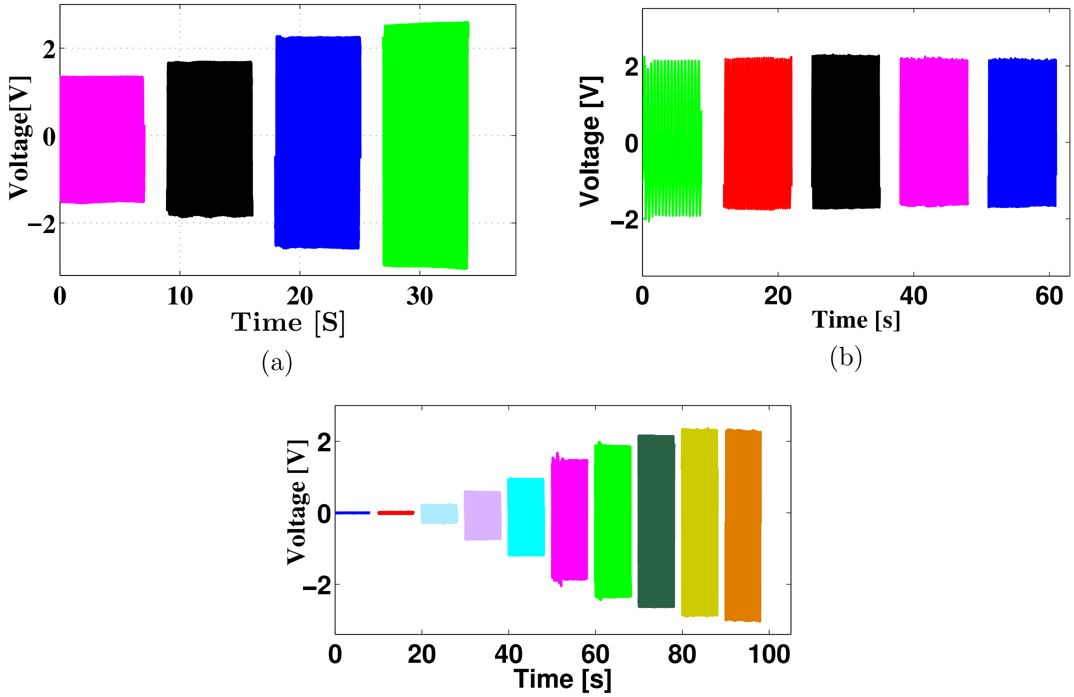

(a) (b)

(d)

Figure 5.21: Investigation of electrical output of the Flexible Sensor III (a) the effect of amplitude of oscillations, (b) the effect of frequency on the open circuit voltage, (c) the effect of external resistance on the output voltage of the flexible sensor III.

A few other tests are also conducted to investigate the performance of the sensor when it is installed into the tire. The test results and the related discussions are provided in Section 6.3.

5.2.5 Concluding Remarks

In this chapter, the laboratory-based experimental results were provided for all of as-fabricated sensors. The performance of hybridized generators was first presented for TCMS. In addition, the developed experimental setup was fully illustrated, and it was shown how it was used for investigating the electrical performance of the Hybridized Generator I and the Hybridized Generator II. For the Hybridized Sensor I, it was shown that the sensor is highly sensitive to the deformation, and it can generate electrical voltage even under a very small angular amplitude of oscillations. The capability of each unit of the sensor including both EMG and TENG parts was fully discussed. For the Hybridized Generator II, a similar study was performed and its potential for energy harvesting and self-powered sensing was scrutinized. The sensitivity of the sensor to resistive loads, amplitude and frequency of excitations was studied. Its general performance was shown under different exciting loads, and then, its capability for tire-condition monitoring was analyzed. However, these two fabricated sensors have shown a promising potential for energy harvesting and self-powered sensing, they cannot be considered as a very promising instrument for implementation in tire system due to their size and also flexibility. The weight of the sensor due to the their EMG units might be influential on the tire dynamics. Based on this conclusion, flexible sensors, based on the TENG unit, were developed for tire-condition monitoring. The first one, which is called "Flexible Sensor I", was tested on tire sidewall to investigate its potential under different mechanical loads. Its mechanical durability was also tested. The sensor shows a good performance for tire-condition monitoring, but there exist two different issues that are addressed with fabricating Flexible Sensor II and Flexible Sensor III. First, the Flexible Sensor I is not dust-free. It means that the tire rubber-dust would be effective on the surface of the materials used in the sensor. The second reason is the electrical output of the sensor, as it is not very high in terms of open circuit voltage. Thus, two encapsulated forms of the TENG-based sensor are developed. The second fabricated sensor is called Flexible Sensor II, which is a single electrode TENG-based device. As it was shown, this sensor is highly flexible and durable, which has a potential to be implemented in monitoring harsh environments such as tire. It has a higher electrical output in comparison with Flexible Sensor I, and the generated signal are more consistent. Furthermore, different types of mechanical loads can trigger the sensor to generate electrical voltage. It is a great feature of this device, which makes it suitable for a wide range of applications including tire-condition monitoring, vibration measurement, and human motion-based energy harvesting. In addition, rubber dusts in tires has no effect on the polymers surface used in the sensor as it is fully covered using the heat shrink wrap. In order to improve the capability of the Flexible Sensor II, it is promoted to a double electrodes TENG based sensor. Using the second experimental setup, an extensive experimental analysis is performed to show its output under different mechanical and electrical resistive loads. This sensor shows high output under different types of loads including bending, pressing, and twisting. It was shown that this sensor can generate up to 16 Volts peak-peak open-circuit voltage under bending load. Flexible Sensor III was tested under different frequency of excitation between 2-6 Hz, and a very slight change is observed in the amplitude of generated open circuit voltage. In comparison with Flexible Sensor II, it shows a better performance in terms of electrical output. Among all of the fabricated sensors, the Flexible Sensor III is chosen for implementing in the smart tire module due to following features:

- Higher electrical output in comparison with other fabricated sensors
- A "Dust-Free" shape, which makes it suitable for utilization in tires
- More durable in terms of lifetime comparing with other fabricated sensors
- Promising thermal durability for working in the tire's environment
- High potential to be used as a self-powered sensing system
- Easy installation and adjustable size for in tire installation

Chapter 6

Smart Tire Modules: Fabrication and Experimental Results

In this chapter, the fabrication procedure of the smart tire modules, the installation of sensors inside the smart tire, and road test results are presented. Section 6.1 presents the fabrication of smart tire module I, and the installation of the TENG-based sensors within tire. In addition, the electrical connection plus the information related to data acquisition for road tests are provided in Section 6.2. The experimental studies of the tire module I contain two main parts. First, a set of laboratory tests are done to ensure the correct installation of the sensors. Results of in laboratory tests are provided in Section 6.3. Road tests are also performed using the smart tire module I when it is installed as the right rear wheel of the vehicle. Results of the road tests and the related analysis are provided in Section 6.4. It was shown that the TENG sensor has a good potential for TCMS application due to its flexibility and independence from the tire velocity variation, however, it is necessary to have a more reliable and an identical process for the fabrication of this sensor, and also, a better data acquisition setup. Therefore, MFC sensors are used for developing another set of smart tire module. In Section 6.5, another module of smart tire is developed based on MFC sensor to investigate its potential for tire-condition monitoring, and proposed an effective strategy for moving towards smart tire system. The data collected from the road test of the second tire module are used for training a neural network presented in Section 6.8.1. This chapter ends with concluding remarks.

6.1 Smart Tire Fabrication: Module I

Two TENG-based sensors are installed (Flexible Sensor III) inside the tire. Their location and orientation are as follows: one sensor is located in the centerline of the tire, and the second one is located in the sidewall of tire.

(a)

(b)

Figure 6.1: Instrumented rim: (a) with modified valves, (b) with wiring

Figure 6.1(a) represents the image of modified rim with valves for wiring. Figure 6.1(b) shows the instrumented rim with wiring. Figure 6.2 shows the image of the sensors located in the centerline and right sidewall. Smart tire module implements a wired data transmission system in which the connecting wires from the triboelectric sensors routed through the rim to the data acquisition setup located within the car. Data from the smart tire module will be collected through the computer inside the car. As presented in Figure 6.2, two sensors are placed in the tire. One of them is located at the tire sidewall, and the second one is attached to the middle of circumference of the tire. This configuration of sensors would allow capturing information related to the tire forces.

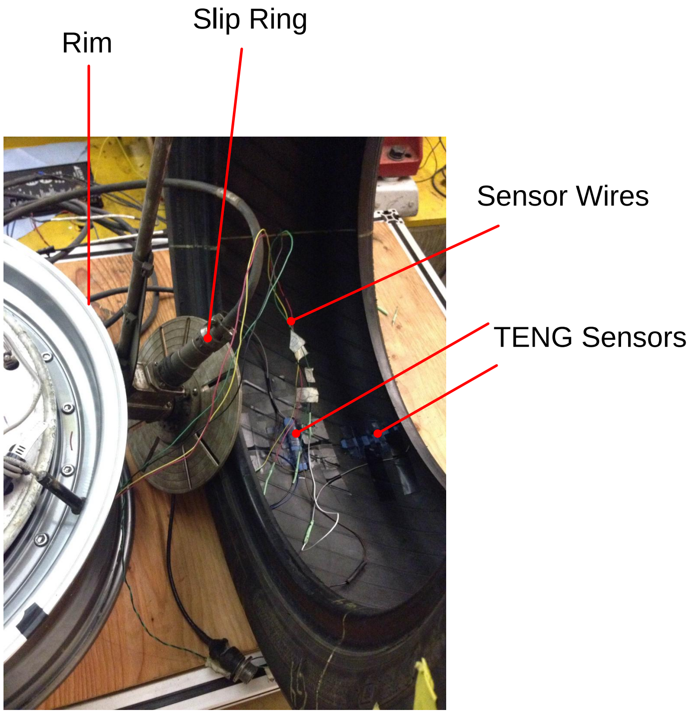

Figure 6.2: Configuration and location of the sensors in tire and slip ring for connecting the sensor wires to the data acquisition setup

Figure 6.3 shows the smart tire system installed to the vehicle ready for testing.

Figure 6.3: The installed smart tire

6.2 Electrical Connection and Data Acquisition

As shown in Figure 6.4, the electrical connection and the data acquisition setup includes a PC to run the Simulink for using the Windows real time target toolbox of MATLAB, a NI DAQ, toggle switches, slip ring connector, and wiring within the tire. In the developed tire-condition monitoring system, the TENG sensors experience deformation when car moves forward or backward. Therefore, a voltage is supplied from the sensors to the system that is representative of the causative deformation. The stranded wires are connected to the sensor terminals and are grouped and routed from the tire interior to a circular connector assembly mounted on the outer surface of the wheel as shown in Figure 6.5.

Figure 6.4: Completed in-vehicle data acquisition system

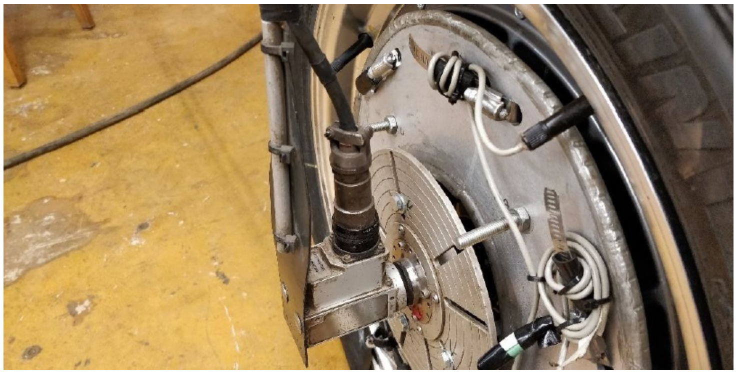

Figure 6.5: Connector assembly linking interior sensor wiring to exterior cable

6.2.1 Toggle switches

In order to accurately measure the data from the sensors, toggle switches are installed to control communication between each of the sensor channels and the DAQ. For a complete circuit to be controlled, the switch was required to close or open at two distinct points; one between DAQ power and one wire of the sensor channel of interest and the other between DAQ ground and the other channel wire. To adhere to this design consideration, the selected toggle switches were of the double-pole single-throw (DPST) designation. DPST switches are designed to simultaneously control two circuits with a single input/toggle.

By observation, a DPST switch functions in a manner analogous to that of a combination of two on-off switches in parallel.The addition of the toggle switches to the parallel junctions creates a control system capable of providing the Simulink program with access to individual data signal channels as per the operators requirement. Figure 6.6 shows a completed system overview including the discussed components.

Figure 6.6 illustrates the parallel junctions attached to the existing DAQ power and ground wires, denoted by POWER JUNCTION and GROUND JUNCTION, respectively. Each of the five DPST switches are labeled TSX where X represents the switch number solely for identification purposes within this graphic.

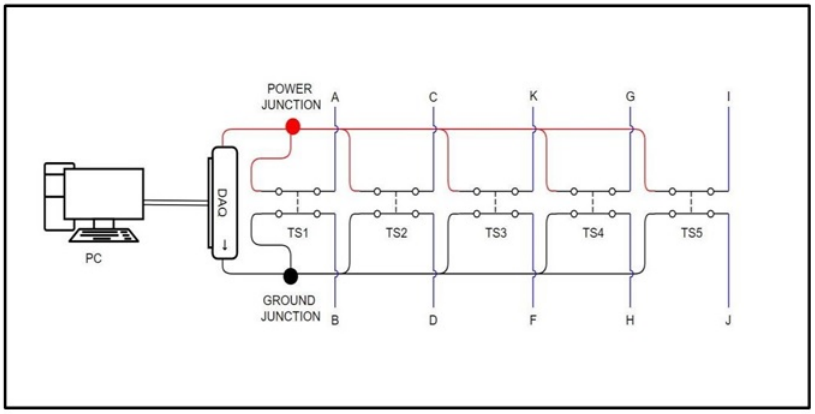

Figure 6.6: Control system diagram overview

The system diagram represents the switches as closed for uniformity. The direction of current flow is irrelevant to the overall operation of this system; however, the illustrated connection order has been followed to allow for simple diagnostics, where DAQ power is connected to sensor wires A and C, while DAQ ground is connected to sensor wires B and D. Figure 6.7 represents the whole assembly with connecting wires.

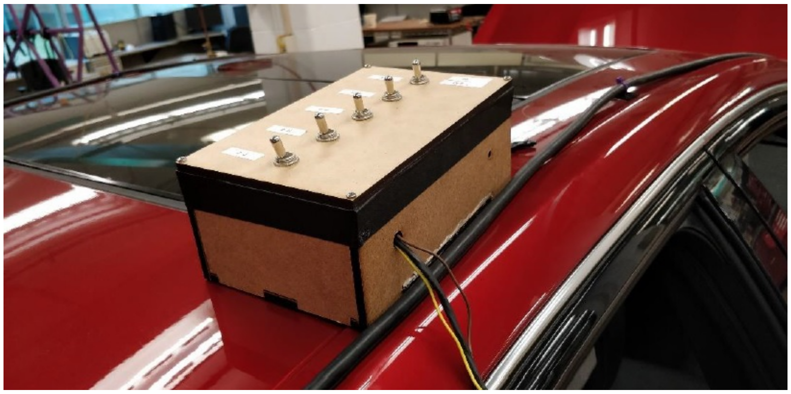

Figure 6.7: Whole assembly of the toggle switches

Figure 6.8 represents the operator using in-vehicle data acquisition setup.

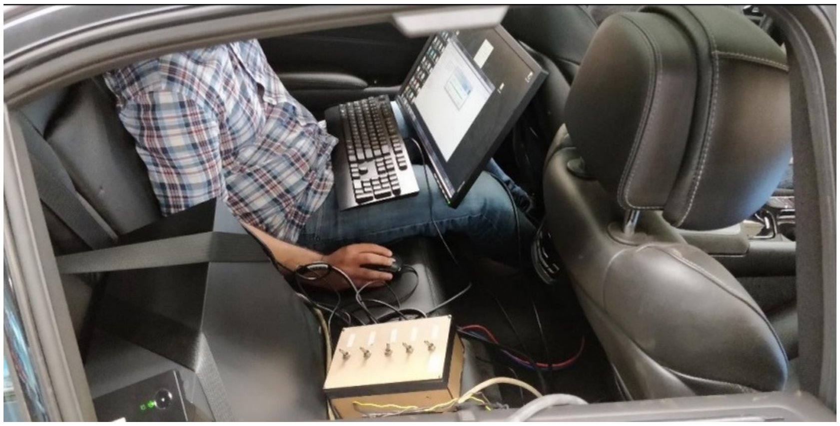

Figure 6.8: Operator using in-vehicle data acquisition setup

6.3 Laboratory Tests

Before starting road tests, a few laboratory tests are conducted to ensure that the sensors have been properly installed and they are ready for the final road testing. Before installation of the tire to the car, a set of dropping tests was performed to analyze the condition of the sensors inside the tire. The tire is dropped from different heights, h_1 and h_2 where $h_1 = 2h_2$. Figure 6.9 (a) represents the response of the sensor located in the sidewall of the tire when it drops to the ground from height h_2. Figure 6.9 (b) shows the response of the sensor after falling to ground from height h_1. As expected when the tire hits the ground from a higher altitude, the generated voltage of the sensor increases. In fact, force in contact surface of the tire with ground increases, which results in increasing tire deformation, and hence the generated voltage of the sensor attached to the sidewall of the tire. The damping behavior of the tire is also detected by the sensor as presented in both figures 6.9 (a-b).

Figures 6.10(a-b) show the response of the sensor located in the centerline of the inner surface of tire. When the tire hits the ground, the sensor starts generating signal until the tire motion is completely dissipated. Figure 6.10(b) displays response of the sensor when it is released from height h_1. As predicted, by increasing the height of tire release location, the generated voltage of the sensor increases.

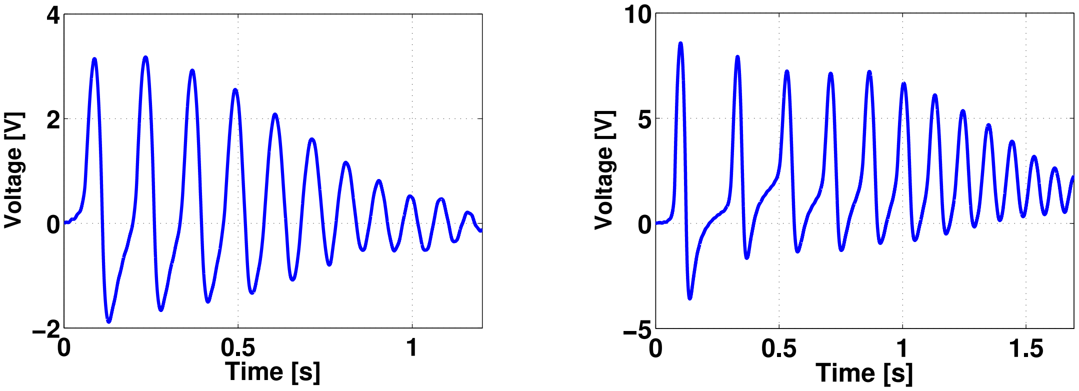

(a) (b)

Figure 6.9: Dropping test: response of the sensors attached to the sidewall of tire when (a) tire is released from height h_2, (b) tire is released from height h_1

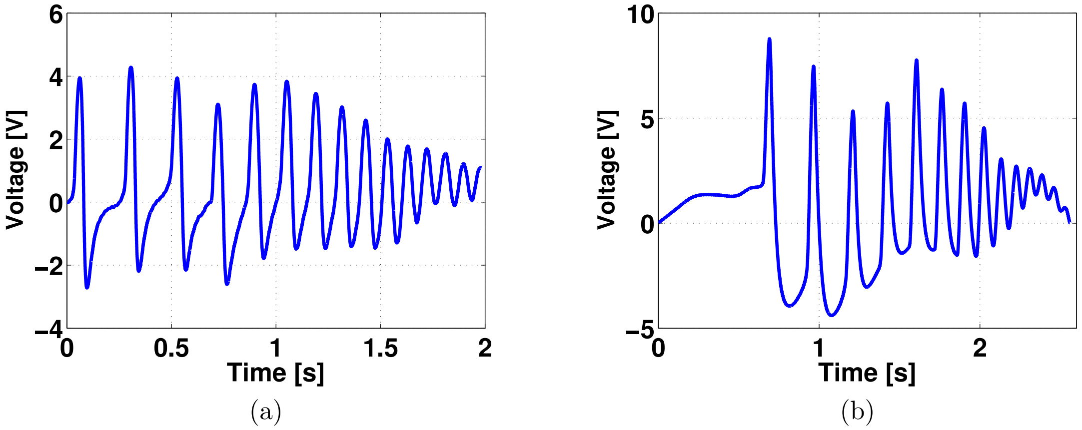

(a)

(b)

Figure 6.10: Dropping test: response of the sensor attached to the centerline of tire when (a) tire is released from height h_2 (b) tire is released from height h_1

Also, the effect of external resistance on the output voltage of the sensor is investigated after its installation to tire. The tire is dropped from height h_1 for 8 different cases of external resistance. As the figure shows, increasing the external resistance enhances the output voltage of the sensor.

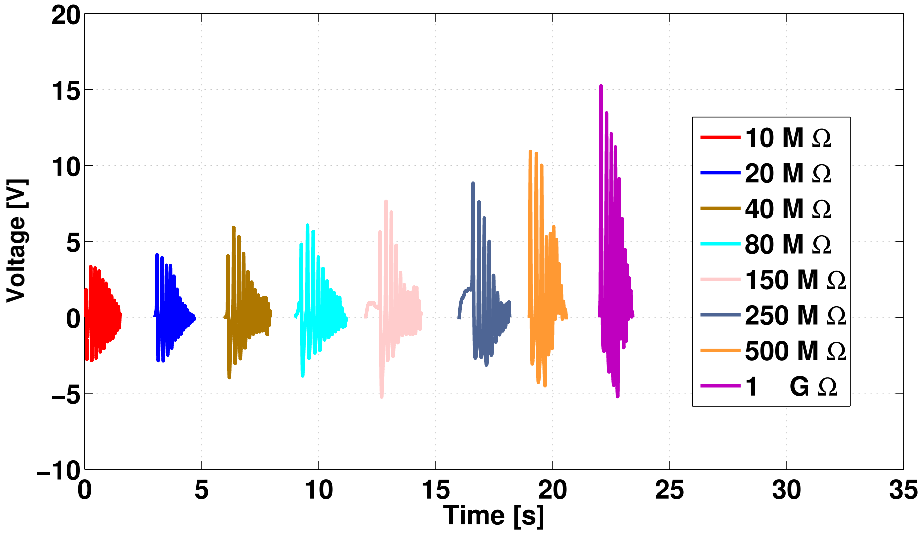

Figure 6.11: The effect of external resistance on the output of sensor

6.4 On Road Tests

A series of road tests were performed with the smart tire module, developed by using TENG-based sensors. The tire force data sets were gathered during specific vehicle acceleration, deceleration and steering maneuver procedures. In this section of thesis, the result related to the following testing scenario is presented:

a) maximum acceleration to 20-25 kph followed by a harsh break to decelerate to 0 kph

The data of sensors were collected using the described data acquisition setup in Section 6.2. A Michigan Scientific (MS) 6-axis wheel load transducer was used at the left rear corner for the sake of comparison and finding the correlation between obtained data of the TENG-based sensor with measured tire forces.

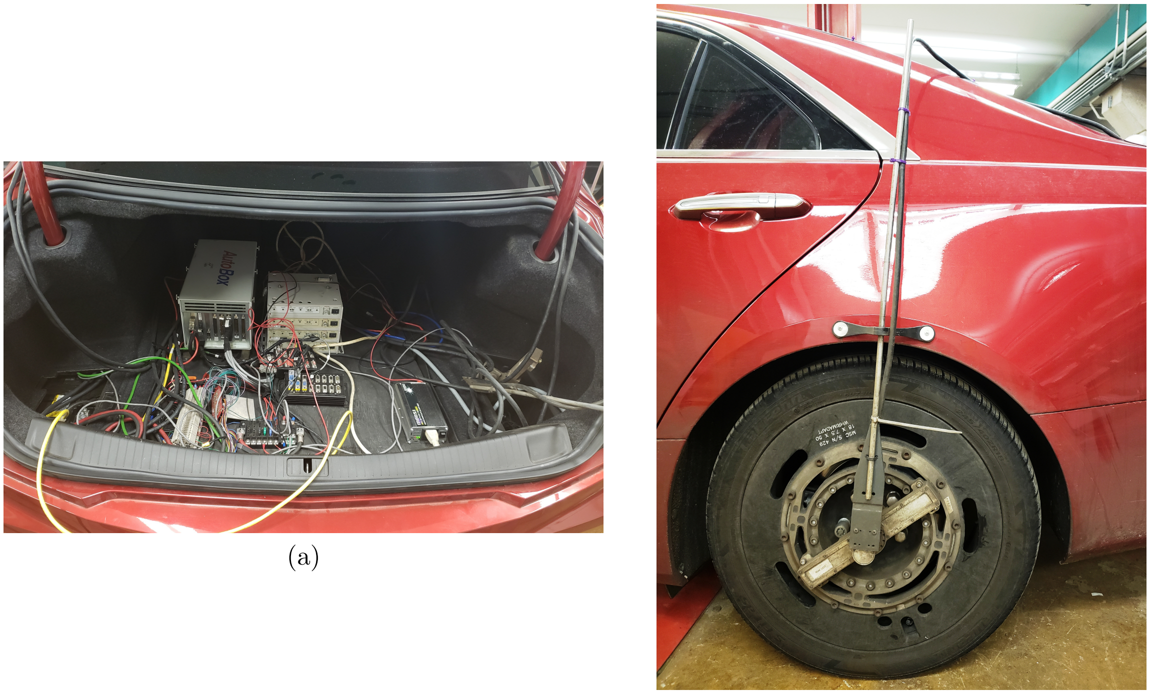

(a)

(b)

Figure 6.12: (a) Data acquisition setup for Michigan Scientific transducer, (b) Michigan Scientific 6-axis wheel installed on left corner-rear wheel

The wheel load transducer was capable of measuring all six tire forces and moments developed at the left rear wheel center, containing all three forces and three moments. Simultaneously, the data of rear tire on right side are obtained to have a comparison between the obtained data from the smart tire module and Michigan Scientific 6-axis wheel. Figure 6.12(a-b) represent the Michigan Scientific 6-axis wheel installed to rear tire at left corner, dSpace and related data acquisition setup.

The testing results are presented in Figure 6.13. A low pass filter is applied to the raw data to remove noises. Figure 6.13 shows the response of the TENG sensor to acceleration followed by a harsh braking. It shows two subsequent braking and acceleration cases. As the figure shows, the sensor can capture the force related to the tire deformation. As the longitudinal forces of tire increases during the acceleration, the generated voltage of TENG sensor increases. In order to match the output of these two systems of sensing, the measured signal of TENG is re-scaled with $\frac{Measured\ Force\ [N]}{1380}$. The generated signal by the TENG sensor is shown by red line. Based on the location of this sensor within the tire, the generated signal of this sensor is correlated to the longitudinal force. Therefore, the data of the sensor is compared with the measured longitudinal force using the Michigan Scientific 6-axis wheel transducer.

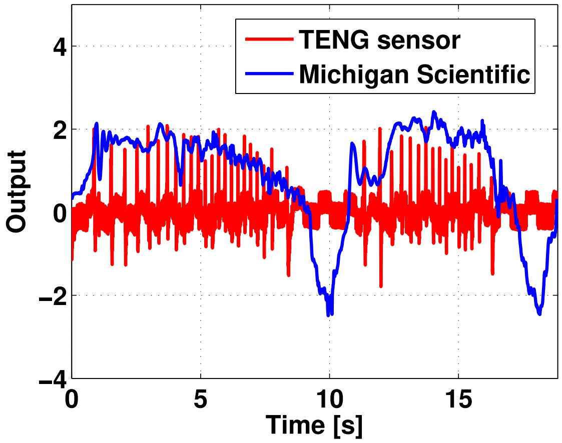

Figure 6.13: A comparison between the generated output of TENG sensor located on the centerline of tire and the output of Michigan Scientific transducer (F_x) (acceleration and harsh brake)

As the figure shows, a good agreement is obtained between the timing of signal generation of the TENG sensor and the Michigan Scientific transducer. Figure 6.14(a) shows different regions experienced by the sensor in each cycle of tire rotation. As the figure shows, there are three main regions, one of them is inside the contact patch, and others are before and after the contact patch of the tire. From the zoomed-view of signal, it is realized that the sensor generates two peaks as V_{max} and V_{min}, presented in 6.14(b).

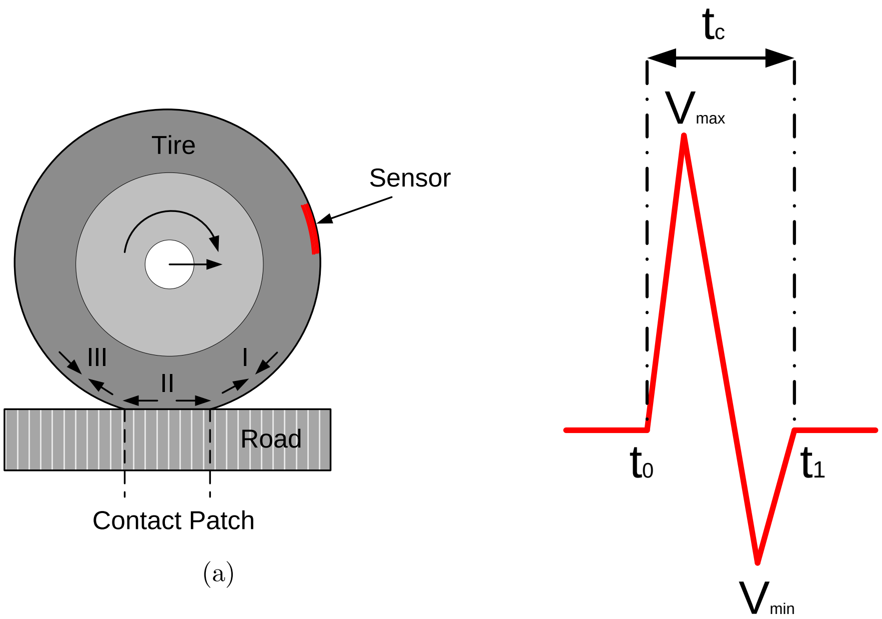

(a)

(b)

Figure 6.14: (a) Schematic of sensor's active and inactive regions in a tire (b) general shape of the generated signal by TENG sensor in the tire

Considering the defined regions in Figure 6.14(a), the first peak is generated when the sensor is entering the tire contact patch, and the second is observed when the sensor is leaving the contact patch. t_0 is the time of entering the contact patch and t_1 refers to the exit time of of the sensor from the contact patch. The period of electrical voltage generation is called t_c. As the size of the sensor and the velocity of the vehicle are known, the size of contact patch can be approximately obtained using the following equation:

$$2L_s + D_{cp} \approx V_c t_c, \tag{6.1}$$

where L_s is the length of the sensor, D_{cp} is the length of the contact patch, and V_c is the velocity of vehicle.

As it was stated earlier, two TENG-based sensors were installed inside the tire. The second one was located in the tire sidewall, and its position was unsuitable in terms of pre-deformation in sensor, and also attachment using glue. After starting the road test, it was observed that the noise to signal ratio was very high, and after a few seconds, it was not generating any meaningful signal. There could be two potential reasons for this unsuccessful set of testing. The first reason is attributed to the failure of sensor attachment to the tire, and therefore the used glue for this application. The basis of the second reason of this failure could be correlated to wiring disconnection.

In order to have a more reliable results using the TENG-based sensors for this critical application, the following items should be considered:

- A more robust fabrication procedure is needed to develop the TENG-based sensor for this specific application. Although, the flexibility and durability of the proposed sensor is promising, developing a set of TENG-based sensors with a complete similar functionality is very important in order to have an accurate analysis from tire dynamic parameters. Furthermore, the data acquisition setup should be improved to simultaneously extract the data from all TENG sensors within tire.
- A better adhesive material should be selected for attaching the TENG-based sensor to the tire. It is necessary to choose an adhesive material with high flexibility and durability for the hostile environment of a tire.
- At least two sensors should be installed in a tire to find different components of tire forces.

It should be highlighted that fabricating a new sensor with high thermal and mechanical durability for tire applications is a big project. The proposed sensory device in this thesis for TCMS, based on TENGs, can be further investigated and modified by future researchers and also graduate students at the MVS lab. Considering the above discussion and also one of the main objective of this work for online tire force identification using intelligent tire system, the commercially available MFC sensors were used to develop another set of smart tire for road testing, which will be presented in the next section of this chapter.

6.5 Smart Tire: Module II

In order to further investigate the possibility of developing a fully functional smart tire, an extensive research was conducted to find a commercial sensor with high durability to work in the harsh environment of a tire considering its wide temperature range and also its life cycle. Finally, Macro Fiber Composite type P2-HT, designed for temperature range between -35 C to 135 C, was found as a suitable candidate for this application [178]. This temperature range shows that MFC sensor suits this application. Based on the provided information about the sensor, its typical lifetime is 10^{11} cycles.

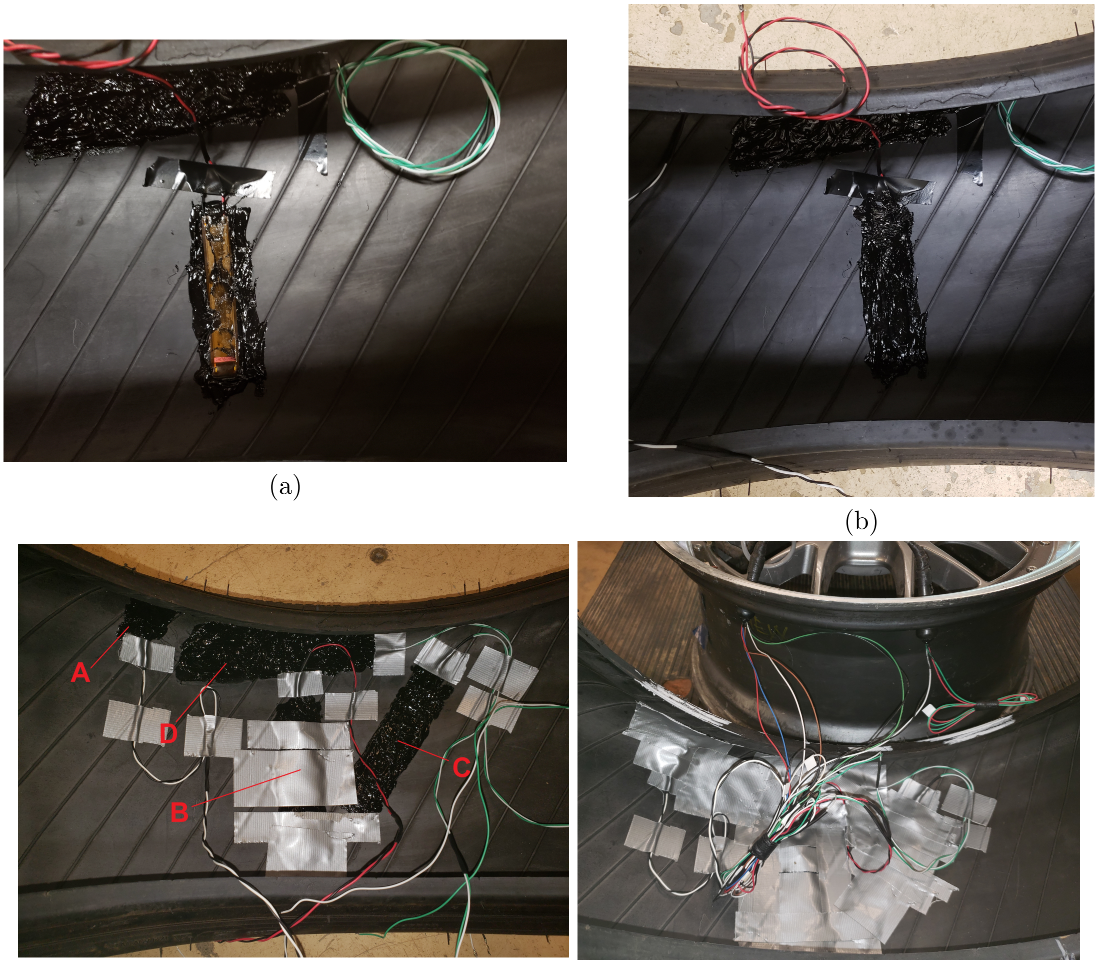

(a)

(b)

(c)

(d)

Figure 6.15: Installation of MFC sensor within tire: (a) covering sensor B with adhesive material, (b) sensor B fully covered with adhesive material, (c) fully attached and covered sensors inside the tire, (d) fully installed MFC sensor inside the tire

Similar to the fabricated TENG-based sensor, it can generate electrical signal under different mechanical loads including bending, expansion, and torsion. Although it does not have the flexibility similar to the TENG-based sensor, it has the potential to be used in tire-condition monitoring system. Two different sizes of MFC-P2-HT sensors were chosen for this applications. The smaller one is located in the sidewall of the tire, and the larger sensor is used in circumference of the tire. Specifications and optical images of the sensors are provided in Appendix C. In order to build the second module of smart tire, four MFC sensors are used and located inside the tire to ensure extracting enough data from tire deformation. To attach the sensor to the tire, black super silicon sealant is used, which is a very flexible adhesive material. The sensor is fully covered with this adhesive and flexible material to fix its position inside the tire. Figure 6.15(a-b) shows how the adhesive material is used to attach the sensor to the tire. Figure 6.15 (c) represents the location of all sensors attached to the tire. Figure 6.15 (d) shows the final packaging of the sensor within tire. As shown in Figure 6.15 (c), sensor C is attached to the tire, between the edges, to have the combined information of sensor B and D. Sensor A is located on the sidewall of the tire to get the information related to tire normal force.

For the second smart tire module, a more robust data acquisition setup is used. For logging the data of all sensors at the same time, PicoScope 2405A is utilized, which is capable of measuring data of four sensors simultaneously as it has four channels for data acquisition, and it is powered using USB port connected to a laptop. The PicoScope is compact enough to be easily connected to the laptop inside a vehicle for tire-condition monitoring system. Figure 6.16 shows the data acquisition setup, prepared for smart tire module II.

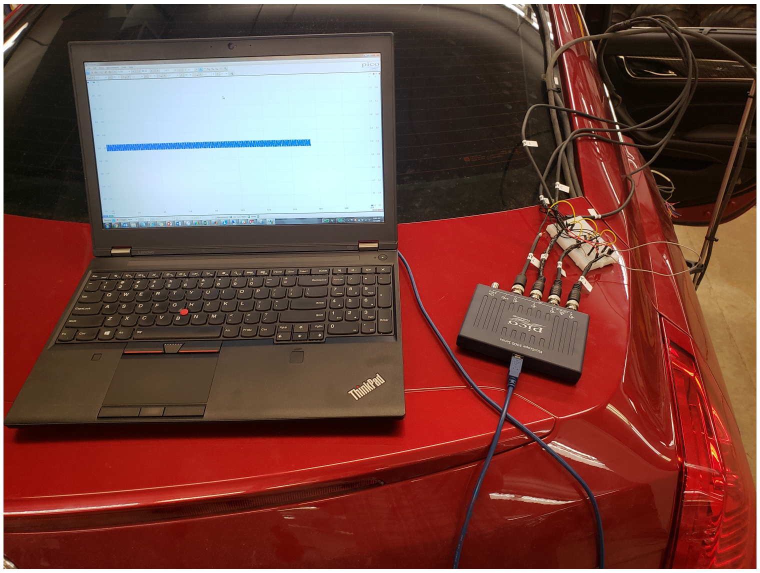

Figure 6.16: PicoScope with four wires coming from sensors inside the tire

6.6 Test Results

Several tests were performed using the smart tire module II. Different scenarios of testing were conducted including: a) regular straight driving; (b) driving in straight line with different accelerations and velocities; and c) sine steering to excite combined slip. In this thesis, the experimental results related to scenarios (a) and (b) are provided and analyzed. In order to evaluate the electrical performance and sensitivity of the sensors, a few preliminary tests were conducted as presented in Figures 6.17(a-d). This scenario is actually based on variation of tire longitudinal force. Basically the most effective dynamical parameter for this test is the variation of longitudinal force of the tire. Figures 6.17(a-d) provide a comparison between the generated signal of the installed MFC sensors and Michigan Scientific transducer.

The main results of this test are as follows:

- The MFC sensors are highly sensitive to tire deformation and they can generate higher than 40 Volts peak to peak voltage. The generated signal by these sensors exceeds the maximum measurable voltage of the data acquisition setup. Therefore, it is needed to add a voltage divider to the test setup to reach a measurable signal for the used Picoscope.

- Figure 6.17(a) represents the speed of vehicle, which is increased up 30 *kph*.

- Similar to TENG sensors, the sensor located on the sidewall of the tire, failed during the first test, and it could not generate a clean signal. This is probably because of the high deformation, exerted to the sidewall of the tire, and the hostile location of the sensor.

- Figure 6.17(b) represents the generated signal by sensor B. Blue line in Figure 6.17(b) shows the longitudinal force divided by 280 to have a similar scale between the generated voltage of the MFC sensor (red line) and Michigan Scientific transducer(blue line). The figure shows that the higher force between the road and tire contact patch results in higher generated voltage by the MFC sensor. A similar behavior is observed in the other sensors located within tire (See Figure 6.17(c-d)).

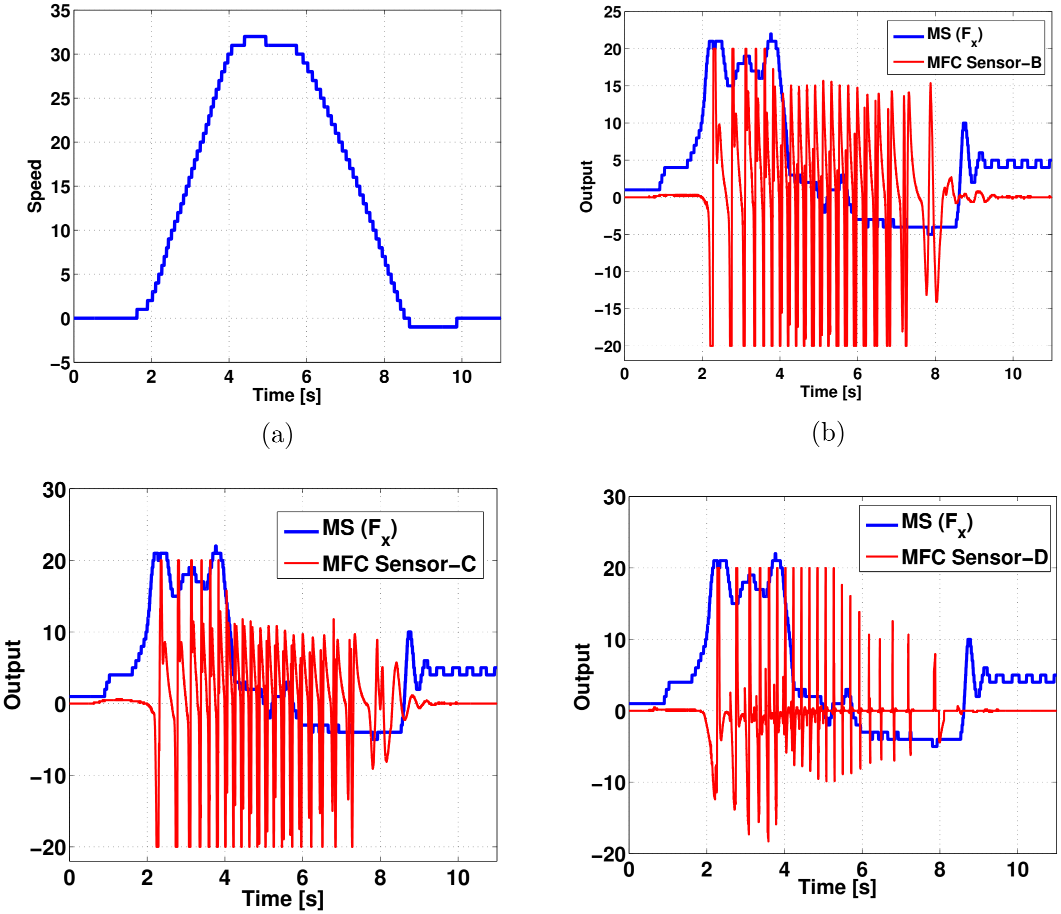

(a) (b)

(c) (d)

Figure 6.17: (a) Vehicle speed during acceleration and brake period; a comparison between the generated voltage by MFC sensors and Michigan Scientific Transducer: (b) sensor B, (c) sensor C, (d) sensor D

Based on the results of the first set of road testing, two similar resistors were added to the circuit, with resistive load of 10 $k\Omega$, in series with the MFC sensors to divide the generated voltage by the sensors. Then, a series of tests were performed to investigate the capability of the MFC device for both energy harvesting and tire-condition monitoring.

6.7 Preliminary Analysis: Sensing and Power Harvesting Potential

The main aim of this part is to show the power harvesting and sensing potential of MFC sesnor in TCMS after adding the resistors to the circuit. Figure 6.18 shows results of the sensor B for a gentle acceleration speeding up 28 [kph] in a straight line. Figure 6.18(a) and Figure 6.18(c) represent a comparison between the generated voltage by the sensor and measured longitudinal force and speed using MS transducer, respectively. The force, measured by MS transducer, is divided by 170 to show it in the same scale as the generated voltage by the sensor B.

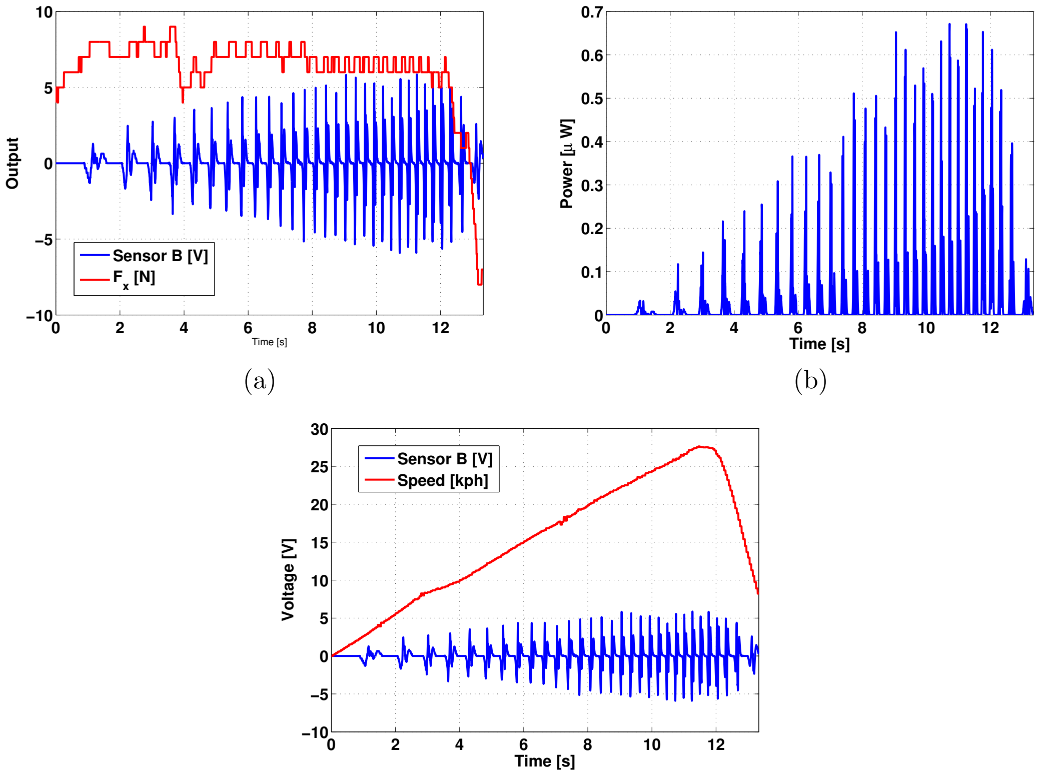

(a)

(b)

(c)

Figure 6.18: Results of sensor B: (a) a comparison between the generated voltage by MFC sensor vs measured force by MS transducer, ($\frac{F_x}{170}[N]$), (b) output power generated by MFC sensor, (c) generated voltage of MFC sensor with respect to the car speed

As the figure shows, for almost the same longitudinal force, the generated voltage of the sensor slightly increases by increasing the speed. As both velocity and longitudinal force decreases, the generated voltage of the sensor decreases. Two important points can be concluded from these two figures: (a) the generated voltage of the sensor B depends on the variation of longitudinal force in tire contact patch, (b) the speed of tire is effective on the generated voltage of the implemented sensor.

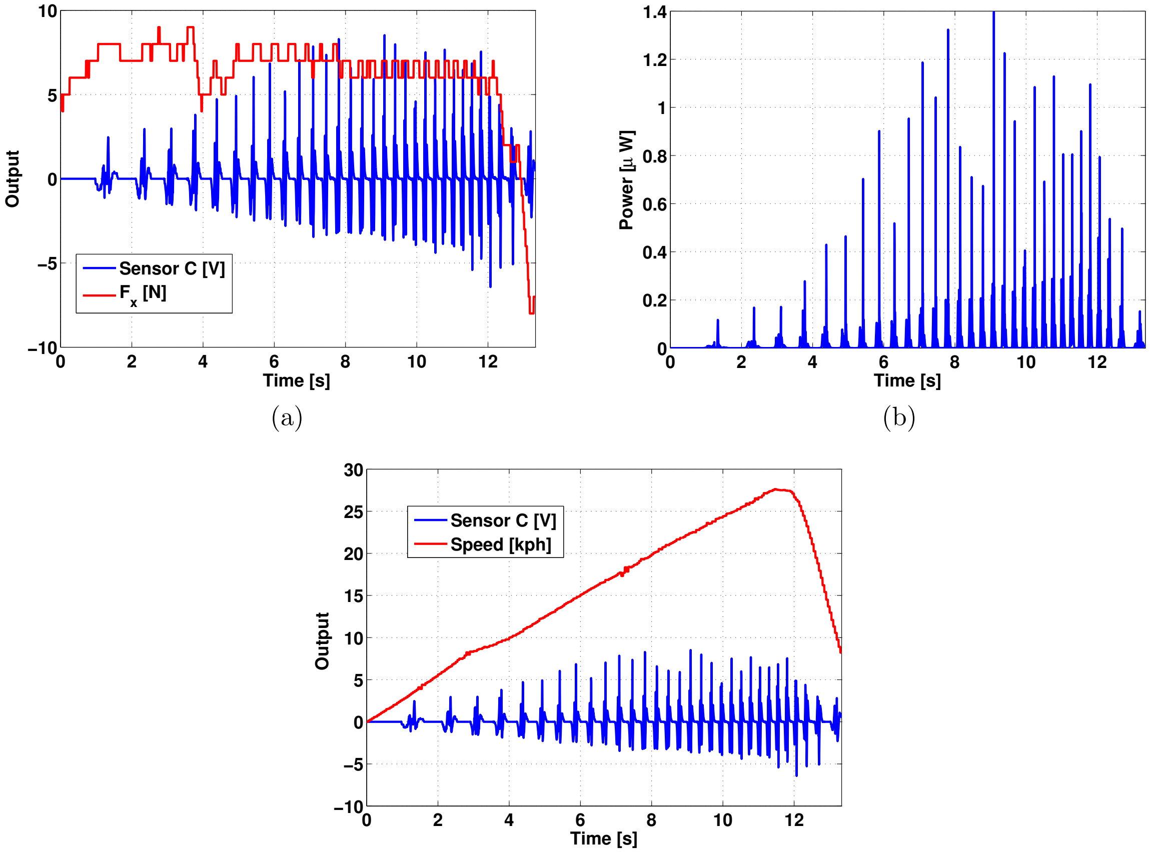

(a)

(b)

(c)

Figure 6.19: Results of sensor C: (a) a comparison between the generated voltage by MFC sensor vs measured force by MS transducer, ($\frac{F_x}{170}[N]$), (b) output power generated by MFC sensor, (c) generated voltage of MFC sensor taking into account the wheel speed

It should be noted that for this test, the variation of lateral and normal forces is very low, which can not be considered as an important factor for the variation of generated voltage by the sensor, however a robust algorithm should be designed to fully investigate the effect of all forces plus velocity on the generated voltage of MFC sensors installed in the tire. Figure 6.18(b) represents the output power generated by the sensor, which can reach 0.65 $[\mu W]$. Similarly, sensor C has a velocity and also longitudinal force dependent behavior as depicted by Figure 6.19 (a) and Figure 6.19(c). In addition, it generates higher voltage in comparison with sensor B. The maximum power generated by sensor C is about 1.4 $[\mu W]$, as presented in Figure 6.19 (b).

In the next section, a machine learning scheme is used to move towards an intelligent tire with the potential of online force identification.

6.8 Online Tire Forces Estimation

In order to have a trained model and online prediction from tire forces, based on the obtained experimental results, different learning methods and algorithms are investigated. Neural network (NN) is chosen for finding a trained package for tire force prediction [179]. Neural network is a powerful biologically-inspired programming paradigm for machine learning from observational data. In this section, the focus will be on the online identification of tire longitudinal forces. To do so, R, a potent statistical programming language, is exploited for finding a trained system to identify tire longitudinal forces. R contains a strong neural network package, which is called neuralnet [180]. This package uses the globally convergent algorithm based on the resilient backpropagation without weight backtracking. In the next section, the algorithm behind the R neural network package is briefly illustrated.

6.8.1 Resilient Backpropagation (Rprop) Algorithm

Several advanced algorithms have been developed for neural networks learning [181]. Broyden-Fletcher-Goldfarb-Shanno (BFGS) [182], Levenberg-Marquardt [183], and conjugate gradients [184] are classified as the well-known algorithms for training feedforward neural networks. Gradient descent methods (GDM) are also popular for supervised learning of neural networks. One of the most efficient techniques based on GDM is batch back-propagation, which minimizes the error function implementing steepest descent method [185].

Adaptive gradient-based algorithms have been also exploited for training neural networks. They are considered as one of the trendiest algorithms for optimization, and also machine learning. Among different Adaptive gradient-based algorithms, Resilient backpropagation (Rprop) algorithm, which is the basis of neural networks in R, is considered as one of the best methods in terms of convergence speed, accuracy, and the robustness considering the learning parameters and rate [186]. Using a sign-based technique, the Rprop algorithm updates the weights to avoid detrimental effects of derivative's magnitude on the updated weight. As this method can effectively tackle the noisy error, they are eminently proper for implementation in hardware. The following set of equations are used to find the size of the update step along a weight direction using a weight-specific, which is called update value: [181,186]:

$$\alpha(x) = \begin{cases} -\Delta_{ij}^{k} & \text{if } \frac{\partial E(w^k)}{\partial w_{ij}} > 0, \\ +\Delta_{ij}^{k} & \text{if } \frac{\partial E(w^k)}{\partial w_{ij}} < 0, \\ 0 & \text{otherwise,} \end{cases}$$

in which $\frac{\partial E(w^k)}{\partial w_{ij}}$ shows the partial derivative of the batch error. The second part of Rprop learning is finding the new update values as below:

$$\Delta_{ij}^{k} = \begin{cases} \eta^{+}\Delta_{ij}^{k} & \text{if } \frac{\partial E(w^{k-1})}{\partial w_{ij}}\frac{\partial E(w^k)}{\partial w_{ij}} > 0, \\ \eta^{-}\Delta_{ij}^{k} & \text{if } \frac{\partial E(w^{k-1})}{\partial w_{ij}}\frac{\partial E(w^k)}{\partial w_{ij}} < 0, \\ 0 & \text{otherwise,} \end{cases}$$

where $0 < \eta^{-} < 1 < \eta^{+}$. R neural network package uses a modified version of the above algorithm for training purposes. Further details about Rprop family algorithms can be found in ref. [181,186].

6.8.2 Tire Testing Data for Training Neural Network

In order to train the neural network for predicting the tire longitudinal forces, several road tests were performed. All of the collected data related to the tire longitudinal forces and velocity measured by the Michigan Scientific Transducer, and the corresponding generated voltage by sensor B and C are presented in this section. With observation of the collected experimental results, the following online measurable data are used as predictor variables: $X_1 = V_B$, which is the generated voltage of sensor B; $X_2 =$ Velocity, which is the vehicle velocity in kph; $X_3 = V_C$, which shows the the generated voltage of sensor C; $X_4 = X_1/X_2$ normalized voltage of sensor B with respect to vehicle's velocity; $X_5 = X_3/X_2$ normalized voltage of sensor C with respect to vehicle's velocity; and $X_6 =$ vehicle's acceleration/deceleration. The longitudinal force F_x is chosen as the output variable, Y. In addition, three hidden layers are considered for the neural network. It should be noted that both speed and acceleration used in the neural network training can be measured by speed and acceleration sensors in any commercially available cars. Three testing results are used for training the neural network, and then the trained NN is tested for two other experimental data to show its potential for developing an intelligent tire. The following diagram shows the training parameters of the neural network.

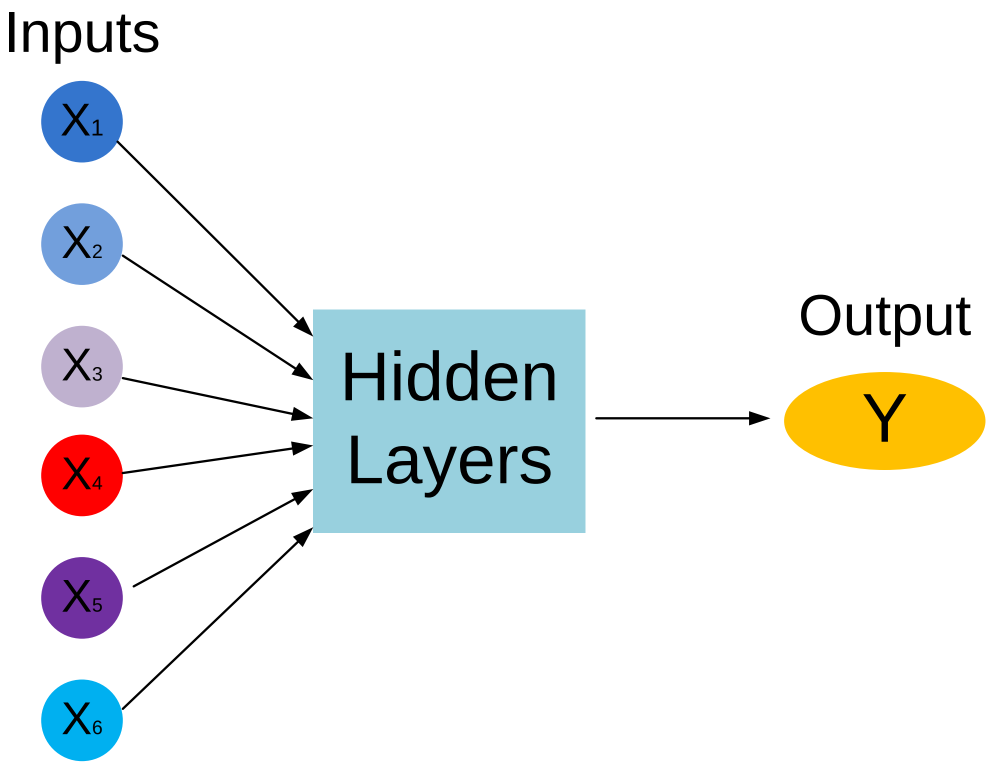

Figure 6.20: Layers of the implemented neural network for tire force identification

For the sake of training the neural network in R, three sets of testing are used, and the trained NN is implemented for two other tests in order to show its capability for the online identification of tire longitudinal force. It should be noted that for finding other tire parameters, it is necessary to have several testing data considering different scenarios of driving. The information of the first test used for training is presented in Figure 6.21. In this test, with a harsh acceleration, the car speed is increased, and then braking is applied. Figures 6.21(a-d) represent the tire longitudinal forces measured by MS transducer, car velocity measured by MS transducer, voltage of sensor B, and voltage of sensor C, respectively. It should be noted that all of these tests were performed in a straight line, and the principal and effective tire force is the longitudinal one.

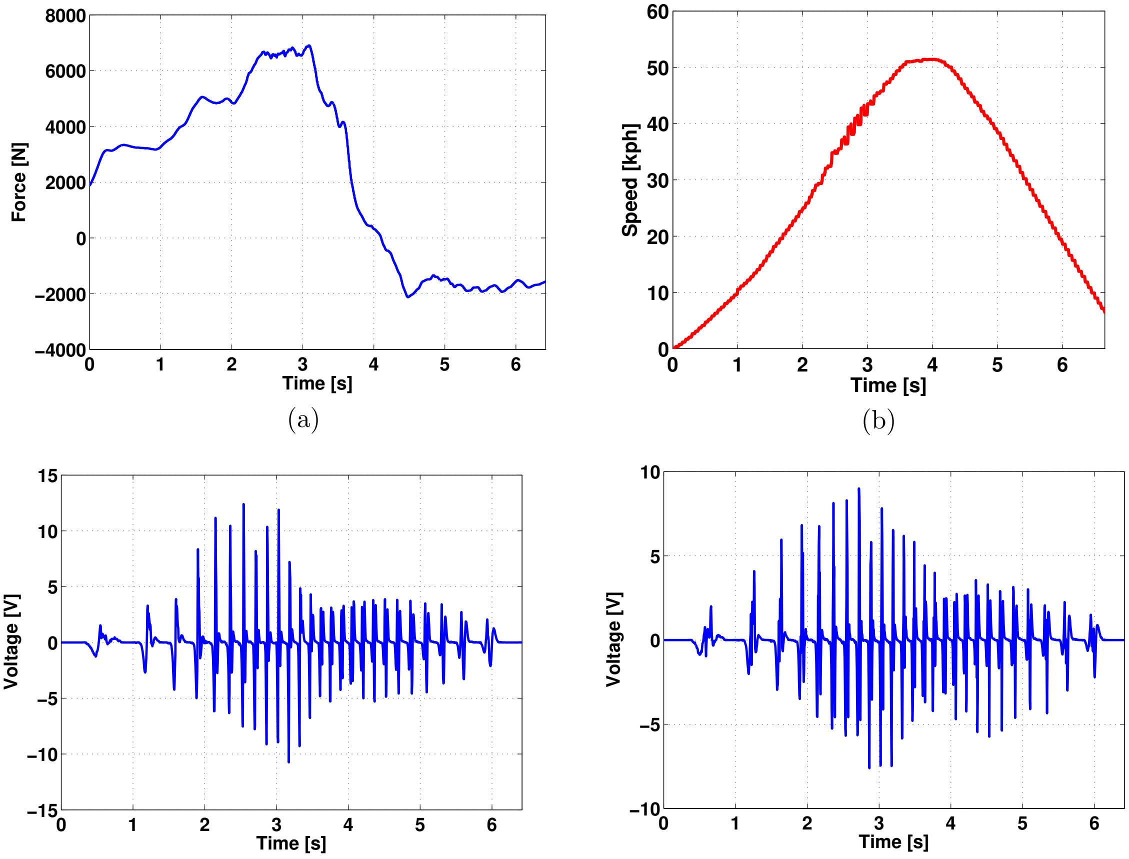

(a) (b)

(c) (d)

Figure 6.21: Testing data for the case of harsh acceleration for training NN: a) longitudinal force measured by MS transducer, b) vehicle's speed, c) voltage generated by Sensor B, d) voltage generated by Sensor C

The second test used for the training purpose is depicted in Figure 6.22. This test was actually performed to study the effect of initial longitudinal force and then driving at both constant force and speed on the sensors signal. Accordingly, the car was driven with increasing the speed to a certain value and then moved forward in a constant speed and longitudinal force. Two tests based on the above-mentioned scenario are used for training the neural network. In the first test, which its results are indicated in Figure 6.22, the speed of the car is increased to almost 20 [kph], and then, the vehicle is moved forward for about 11 seconds at the constant speed of 20 [kph].

In order to reach this speed, the longitudinal force is increased to 5000 [N] and then is decreased to an approximately a constant value as presented in Figure 6.22(a). Vehicle's speed, the generated voltage of sensor B, and the generated voltage of sensor C are presented in Figures 6.22(b-d), respectively.

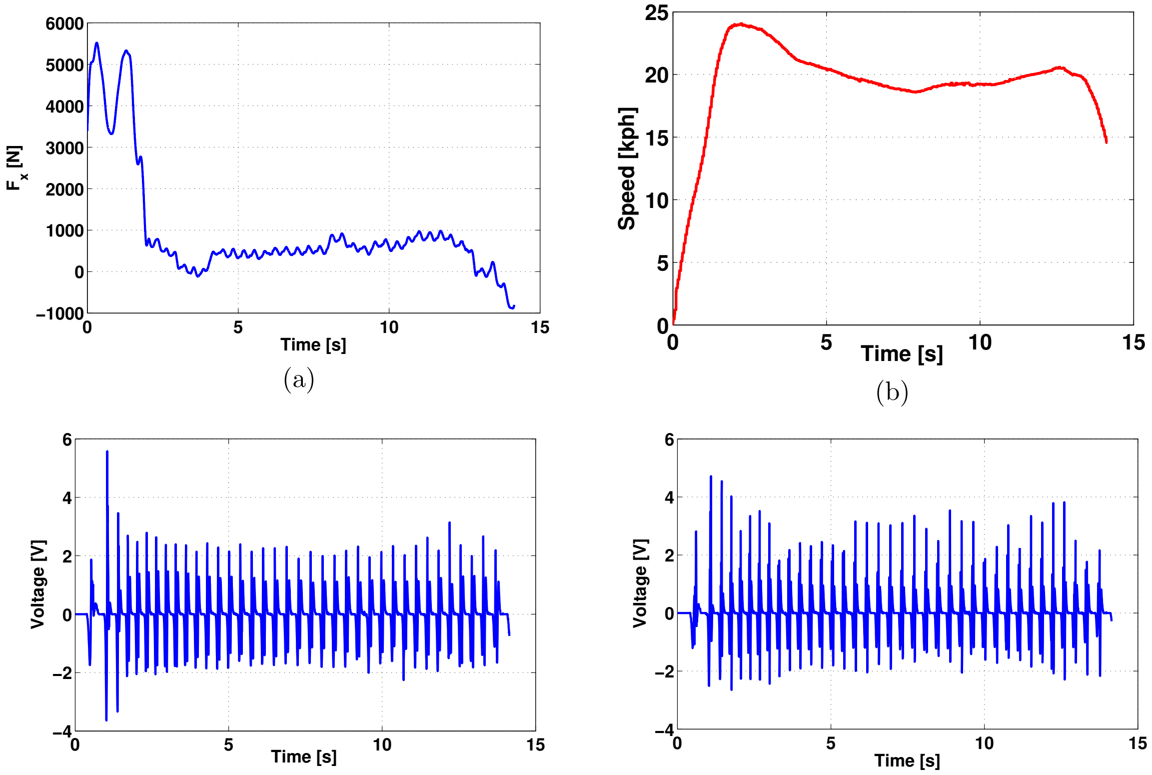

(a) (b)

(c) (d)

Figure 6.22: Testing data for the case of 20 kph for training NN: a) longitudinal force measured by MS transducer, b) vehicle's speed, c) voltage generated by Sensor B, d) voltage generated by Sensor C

The third test used for training the neural network is based on the scenario of reaching a constant speed and a constant force for a period of driving, similar to the previous case. As Figures 6.23 (a-b) show, the car was driven with increasing the speed to a certain value, for this test 7 kph, and then, moved forward with a constant speed and longitudinal force. As the figure shows, during the transient period, the longitudinal force is increased up to 1800

N, and then it is drastically reduced to reach the desired constant speed. Figures 6.23 (c-d) represent the voltage generated by sensor B and sensor C during this test, respectively.

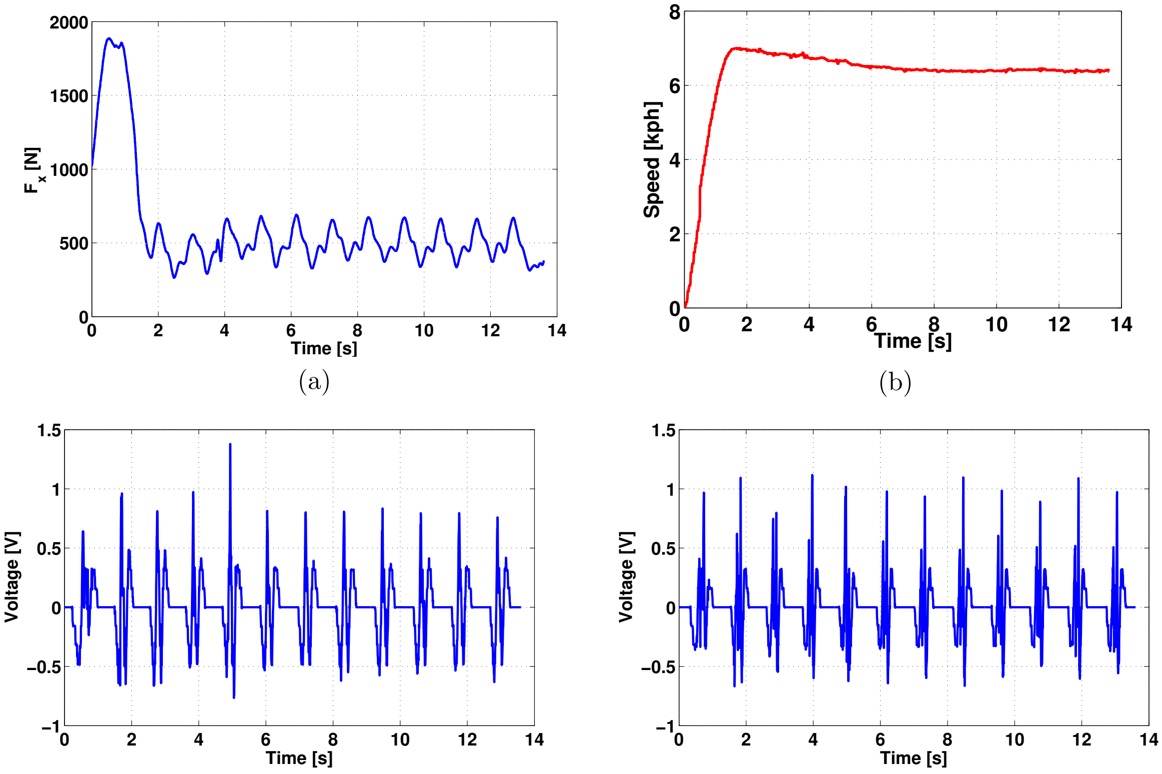

(a) (b)

(c) (d)

Figure 6.23: Testing data for the case of 7 kph for training NN: a) longitudinal force measured by MS transducer, b) vehicle's speed, c) voltage generated by Sensor B, d) voltage generated by Sensor C

In order to investigate the qualification of the trained neural networks, it is initially tested for the utilized testing data with investigating its Normalized Root Mean Square Error (NRSME) for online identification of the tire longitudinal forces. NRMSE is the normalized square root of the average of squared differences between predicted and the actual values , which can be found by the following equation:

$$NRMSE = 100 \times \frac{\sqrt{\frac{1}{m}\sum_{i=1}^{m}(F_{x_i} - \hat{F}_{x_i})^2}}{F_{x_{max}} - F_{x_{min}}}, \tag{6.2}$$

where m, F_{x_i}, and $\hat{F}_{x_i}$ show the number of samples, the actual value of the longitudinal force, and the predicted value of the longitudinal force, respectively. Using the above equation, the NRSME for harsh acceleration test presented in Figure 6.21 is obtained as 4.13 %. For the testing data, shown in Figure 6.22 (constant speed of 20 $[kph]$), NRSME of the identified force is calculated as 2.102 %. For the last test in which the car was driven with the speed of 7 $[kph]$ (see Figure 6.23), NRSME is obtained as 1.684 %. As the error analysis shows, the trained NN can accurately predict the testing data, and therefore, it can be used for the identification of tire longitudinal forces for other testing cases. Using the vehicle and sensors' measurable data as the predictory variables, the tire longitudinal force is identified. In the next section, it is shown how the trained NN can effectively identify the tire longitudinal force.

6.8.3 Online Force Identification Using the Trained NN

With the implementation of the trained NN, two different driving cases are selected for online longitudinal force identification. The first case is presented in Figure 6.24. As Figure 6.24 (a-b) show the driving test has two parts. In the first part, presented with number 1 in Figure 6.24 (a), tire longitudinal force is increased and then decreased to reach a constant force and a constant speed (presented in Figures 6.24(a-b)). The results show that the trained NN is accurate enough to identify tire longitudinal force in both regions 1 and 2. Comparison of the measured longitudinal force with MS transducer and identified forces using trained NN shows a very good agreement between them. With only using the defined predictory variables in Section 6.8.2, the response variable (F_x) has been identified with a good accuracy. The interesting point about the presented comparison in Figure 6.24(a) is the potency of the trained NN for almost accurately detection of region 1, and also identifying the peak value of tire longitudinal force. Figures 6.24(c-d) show the generated voltage of sensors B and C during this test.

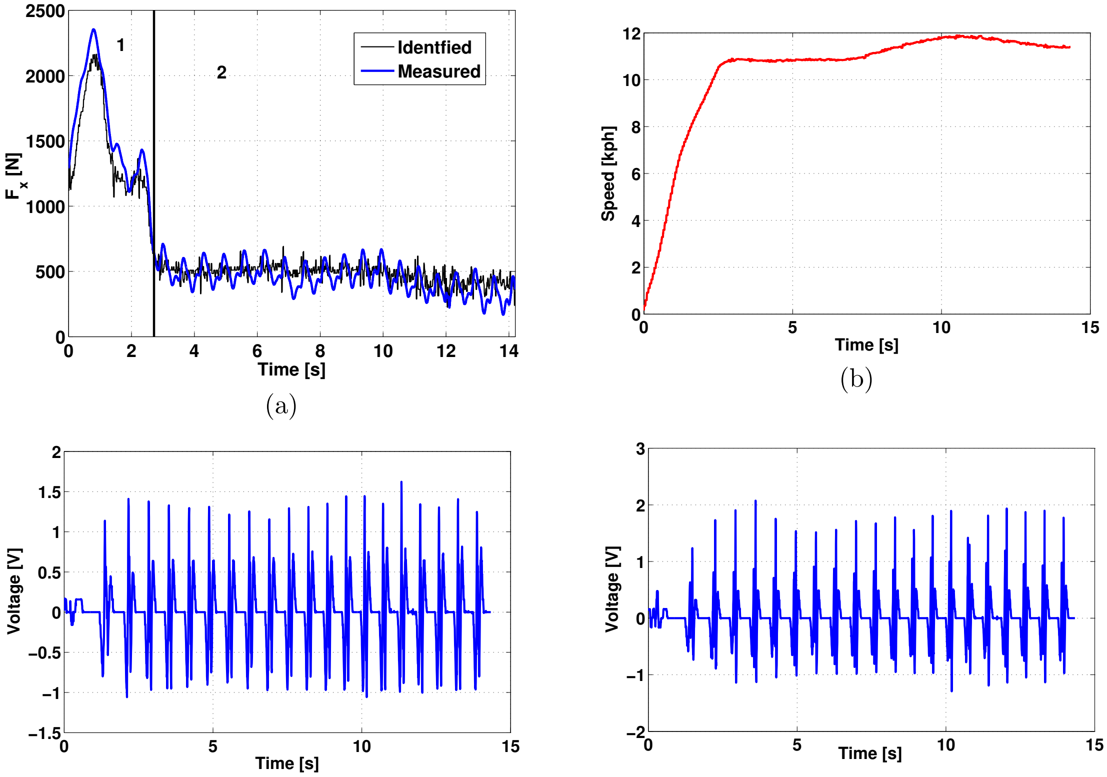

(a) (b) (c) (d)

Figure 6.24: Testing the trained neural network: (a) a comparison between tire identified force using trained NN and measured force by MS transducer, b) vehicle's speed, c) voltage generated by Sensor B, d) voltage generated by Sensor C

Another driving scenario is selected to further investigate the potential of the trained NN for tire force identification. In this case, depicted in Figure 6.25, the vehicle is driven with a modulated acceleration in which it experiences multiple acceleration and deceleration. Region presented with odd and even numbers in Figure 6.25(a) represent the acceleration and deceleration parts, respectively. Similar to the previous case, using the defined predictory variable in Section 6.8.2, the tire longitudinal force is identified.

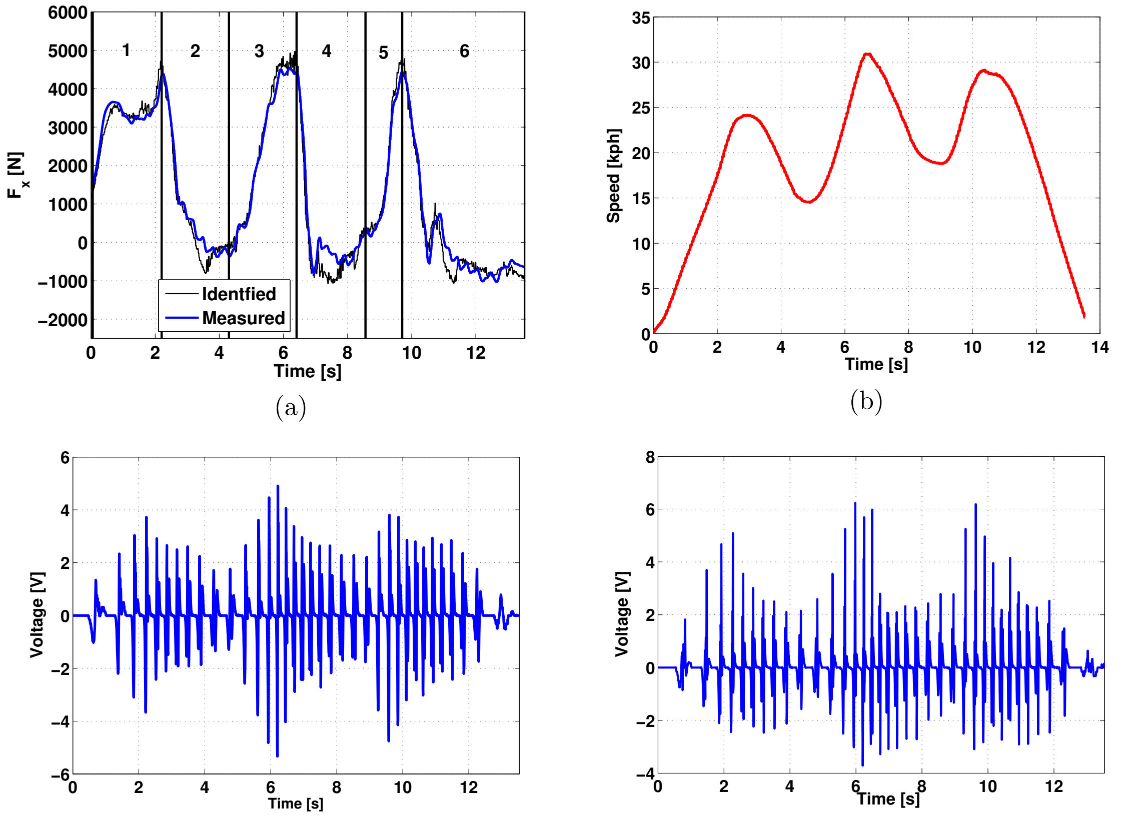

(a) (b)

(c) (d)

Figure 6.25: Testing the trained neural network for the case of modulated acceleration: (a) a comparison between tire identified force using trained NN and measured force by MS transducer, b) vehicle's speed, c) voltage generated by Sensor B, d) voltage generated by Sensor C

In addition, as Figure 6.25(a) reveals, the trained NN not only can identify all acceleration and deceleration parts accurately, but also, it can predict the value of the longitudinal force with a good accuracy. Figure 6.25(b-d) represent the vehicle's speed, generated voltage of sensors B and C, respectively. Figure 6.26 (a-b) show the normalized values of generated voltages by sensor B and sensor C with respect to speed for the case of modulated force. As the figure show, the normalized value of the voltage represent the sensitivity of the sensor to longitudinal force variation. Furthermore, looking at the time envelope of the normalized signal of the sensors can show the accelerating and decelerating regions and the corresponding variation of the force.

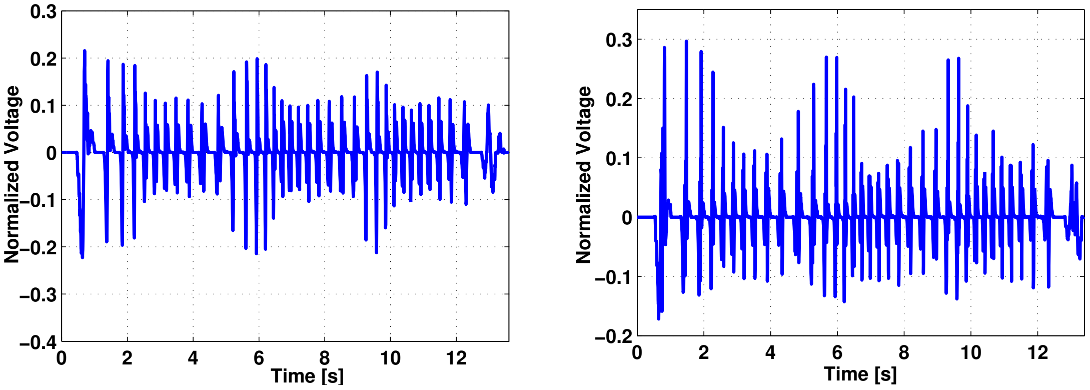

(a) (b)

Figure 6.26: Normalized values of voltages with respect to speed (a) sensor B, (b) sensor c

The presented force identification in this part shows that with implementation of a trained tire using a powerful machine learning algorithm, based on considered inputs, tire dynamical parameters can be identified with a good accuracy. This is an important step towards intelligent tire and also addressing open challenges in autonomous driving.

6.9 Concluding Remarks

In this chapter, two set of intelligent tire modules were designed, fabricated and tested. The first one was designed and fabricated based on the developed flexible TENG sensor. Several laboratory tests were performed after installing two TENG sensors within tire in order to study the performance of the sensors under different electrical and mechanical loads. In addition, an on-road data acquisition setup was developed in conjunction with Windows real time target in order to measure the data generated by TENG sensors during the actual driving test. The Michigan Scientific transducer was used to have a reference with regard to the forces in the tire. The smart tire was installed in Cadillac CTS and performed the road test to investigate the potential of flexible TENG sensor for smart tire system. The experimental results show that they are capable of detecting acceleration and braking periods. In addition, they are very sensitive to tire forces. The measured signals from the sensor can be also used for finding the length of tire contact patch. Although TENG sensors have shown a high potential for this application in terms of flexibility and high sensitivity to even low forces, based on the results of road tests, the following points should be addressed in the future research to actualize the proposed idea of implementation of TENG sensors in smart tire systems:

- A more robust and identical approach should be chosen in order to fabricate the TENG sensor for this hostile environment.
- The flexibility of TENG sensor is very appealing for this application. A more robust sensor is needed for tire application based on the provided framework in the present thesis.
- With a better data acquisition setup and also on-board circuit, TENG sensors could provide a reliable solution for the tire of future in terms of tire forces measurement and road conditions.
- TENG sensors are in their early-stage for this real-world application. Experimental works conducted in this PhD research delineate triboelectric nanogenerators, taking into account their flexibility, and different operating modes can be considered as a promising technology for developing smart tires.

The second tire module was built using the MFC sensors. The second smart tire module was designed, tested and fabricated based on the experience obtained from previous smart tire tests using TENGs. Using a flexible adhesive material, one of the main challenges was addressed for attaching the sensors into a tire for real-world testing.

In addition, a very robust data acquisition setup was developed, which allows performing different testing and maneuvers using the second smart tire module.

MFC sensors have shown a very good candidate for smart tire applications. Although two of the installed sensors have shown no signal after the harsh sine steering tests, the other MFC sensors worked in a good condition in six different days of testing. Numerous testing scenarios were conducted to analyze the behavior of the MFC sensors and their potential for tire-condition monitoring systems. It was observed that MFC sensors can detect the variation of longitudinal and lateral forces in the tire contact patch. Furthermore, they have sensitivity to the tire speed. The data provided based on the extensive experimental analysis using the second tire module can be used as a framework for future research on the smart tire to develop a fully trained machine learning algorithm based on generated voltage of the sensors and measured forces, acceleration and velocities signal using the Michigan Scientific transducer. A short durability test was also conducted with driving about 30 minutes in the University of Waterloo Ring-road with the speed in the range of

$0-50[kph]$. The MFC sensors have shown no degradation during this short durability test. The following important points should be highlighted based on the tests using the MFC sensors:

- MFC sensors can pave the way for tire companies towards the smart tire as they have shown reliable and distinctive signals under different testing scenarios of driving.
- They have a good potential for energy harvesting to power embedded circuits for sending the signal to driver's cabin.
- The trained NN shows a high potential for detection of tire longitudinal forces. It is the first and principal step towards intelligent tire systems. In order to have a fully trained NN, it is necessary to have several testing cases to identify all tire dynamical parameters including forces and moments. With adding more experimental data to train the neural network, a robust and fully functional intelligent tire can be actualized.
- On-board circuit should designed for both sensing and energy harvesting to send the generated signal of the sensors for the post-processing.

Chapter 7

Conclusions and Future Works

In this thesis, a comprehensive study was provided on the implementation of different sensing technologies for tire-condition monitoring systems. A detailed review was provided on the current technologies used for this application, then developed five different sensing devices for tire-condition monitoring system. The developed devices includes two hybridized electromagnetic-triboelectric nanogenerators and three flexible triboelectric nanogenerators. The main conclusions of this thesis related to the hybridized EMG-TENG are as follows:

- Development of two hybridized electromagnetic-triboelectric nanogenerators for the targeted application is one of the main contributions of this thesis. The whole design, modelling, optimization and fabrication procedures for each of the hybridized generators were fully discussed and presented. The complimentary roles of each sensing mechanism in the developed hybridized generator was discussed. The sensitivity of the fabricated devices was investigated with respect to amplitude and frequency of excitation. The optimal resistor in order to reach the highest power density for both of the fabricated devices were shown. In addition, the potential of hybridized TENG-EMG devices was fully investigated for tire-condition monitoring, presented in Chapter 5.
- The working mechanisms and also the finite element simulation pertinent to both hybridized devices were fully discussed.
- It was shown that the Hybridized Sensor I has a great potential for detection of angular deformation, which makes it an excellent candidate for rotational motion and bending sensing.

- A discussion was provided on the potential of Hybridized Sensor II for TCMS.

Although these two hybridized devices have represented a great potential for energy harvesting and self-powered sensing system, they cannot be considered as an ideal choice for implementation in tire system due to their size and also flexibility. One of the main challenges for the use of hybridized sensors is the weight because of the their EMG units, which can be effective on the tire dynamics. Consequently, flexible sensors were designed based on the TENG unit. In Chapter 4, the development of three different types of flexible triboelectric nanogenerators was presented for tire-condition monitoring applications. Modelling, working mechanism and the finite element simulations of these sensors were fully discussed in Chapter 4. The following are the main highlights based on the developed flexible TENG-based sensors for tire-condition monitoring applications:

- Three flexible nanogenerators with the potential of being used in tire-condition monitoring system were developed. Flexible Sensor I operates based on the single-electrode mode of TENGs and has a very good flexibility for the utilization in tire systems. The sensor was tested on the sidewall of a tire to study its potential for tire-condition monitoring application. However, the sensor have shown a stable signal generation during a few hours of testing and has a good performance in terms of durability, there were two issues which disqualify this sensor for tire-condition monitoring system: a) This sensor is not a dust-free device, and the environment of tire with rubber dust would have a negative effect on its performance in terms of electrical output; b) it is not capable of generating high open-circuit voltage as it is required for implementation in tire system in order to have a high signal to noise ratio.

- In order to address the above issues, Flexible Sensor II was designed, modelled and fabricated. The Flexible Sensor II has a flexible structure and materials similar to the first one, but it has a heat shrink wrap as a cover, which makes it a fully encapsulated sensor.

- The experimental results show that this sensor has a higher electrical output in comparison with Flexible Sensor I, and it is capable of generating a more consistent signal in comparison with the first design.

- A very exciting feature of this encapsulated sensor is its sensitivity to different types of mechanical loads including bending, twisting and pressing. The testing results show that this sensor can generate more than 5 Volts peak to peak voltage under strong finger pressure, more than 8 Volts peak to peak voltage under bending load, and more than 6 Volts under twisting load. This feature makes it an ideal candidate for different applications including tire-condition monitoring and vibration measurement. Furthermore, rubber dusts in tires were not effective on the sensor performance, as it was fully covered using the heat shrink wrap.

In order to enhance the electrical output of the second flexible sensor, two copper electrodes were used in Flexible Sensor III. Based on this double electrode encapsulated TENG sensor, the performance of the sensor was analyzed under different electrical and mechanical loads. It was shown that Flexible Sensor III has a high electrical output under different types of loads including bending, pressing, and twisting. For example, under bending excitation, it can generate up to 16 Volts. Furthermore, it generates a consistent and stable open circuit voltage with a very slight change under different frequencies of excitation between 2-6 Hz. Comparing to other fabricated sensors, Flexible Sensor III shows a better performance in terms of electrical output and mechanical durability. Also, it can be easily installed inside the tire and can be adjusted with different sizing. Among all of the fabricated sensors, the Flexible Sensor III was chosen for real-world testing and in-tire implementation. A smart tire module was built using this sensor, and then, the smart tire was installed into the car for a few on-road testing scenarios. The used sensors have shown a high sensitivity to lower tire forces, but they were not able to fully detect the variation of higher forces. The following remarks are the main conclusions of using TENG-based sensor for tire-condition monitoring:

- The flexibility of fabricated TENG sensor is very appealing for tire-condition monitoring system, and with a better fabrication procedure, it can be considered as an ideal candidate for this application.
- With a better circuit design and energy harvesting module, TENG based flexible sensor has a high potential to be used as the measurement tool inside the tire.
- They can be also used for finding the length of tire contact patch and tire rotational velocity.
- Using a machine learning algorithm plus with having several testing results, a fully intelligent tire can be developed based on TENG-based sensors.

In order to further study the feasibility of intelligent tire and tire-condition monitoring systems, the second smart tire module was tested using the commercially available, thermally and mechanically durable MFC sensors. An extensive on-road testing was conducted to investigate the potential of MFC sensor for this application. The experimental results show that MFC sensors have a promising potential for detecting variation of tire forces and in-tire power harvesting. Following points are the main concluding remarks based on testing of the second smart tire module:

- MFC sensors can be used for the detection of the variation of tire longitudinal force, and the selected location for sensor inside the tire is appropriate for measuring this force.
- The experimental studies show that MFC sensors have high sensitivity to both the variation of tire forces and speed.
- They can show the tire deformation profile as the sensor enters to the tire contact patch and leaves it.
- MFC sensors generates higher electrical output in higher velocity and forces, therefore, its higher generated voltage can be used for energy harvesting. It actually paves the way for developing the self-powered sensing package for tire-condition monitoring system.
- A novel strategy based on the MFC sensors, velocity and acceleration of the vehicle was presented using the neural network package in R for online identification of tire longitudinal force.
- The trained neural network was capable of online identification of tire longitudinal force with high accuracy, as presented in Section 6.8.3. It can be considered as a principal step towards developing the intelligent tire of future.
- The extensive experimental data provide a very informative and valuable source for further research in the area of tire-condition monitoring system, and the use of MFC sensors for measuring tire forces.

The very last important point should be highlighted based on the cost of TENG-based sensors. Considering the proved conceptual design of the TENG-based sensor in this thesis, the use of self-powered flexible TENG sensor with high thermal and mechanical durability inside a tire would have slight impact on the cost of a tire in comparison with other commercially available sensors. This advantage of TENG-based sensor would make the actualization of the future intelligent tire more possible. In the next section, a few ideas and suggestions based on this PhD thesis for future works in the areas of tire-condition monitoring are presented.

7.1 Future Works

In order to use TENG-based sensor for real-world testing and tire-condition monitoring, the following works should be considered as the future works:

- A better fabrication procedure should be used in order to develop the flexible TENG-based sensor for this specific application. In this thesis, it was shown that TENG-based sensor has a good potential for tire-condition monitoring system, but a set of identical flexible TENG sensors should be developed using a fully machine-based fabrication and packaging.
- An on-board circuit should be designed to collect the data measured from the TENG sensor, and wirelessly send it to the control unit of a vehicle.
- Instead of installing the TENG sensors on the tire surface using adhesive materials, they should be embedded into the tire body. This would reduce the uncertainty related to the use of adhesive materials in the generated signal of TENG sensors.
- A robust filter should be designed to avoid noises and increase the SNR of the TENG sensor for this applications.
- It should be noted that TENG-based sensors are in their early-stage of development. As the material scientists are exploring different aspects of this novel technology for self-powered sensing system, new doors would be opened for choosing even better materials with higher durability for the harsh environment of tire.

The second module of smart tire has shown the capability of MFC sensor for tire-condition monitoring. The following steps should be taken into account to fully actualize the intelligent tire of the future using MFC sensor:

- All of the testing was performed for velocities less than 50 [kph]. A set of testing should be done for higher velocity to investigate its impact on the performance of the MFC sensors for this case.
- The effect of high forces on the durability of the MFC sensor inside the tire should be investigated. It was shown that MFC sensors can generate reliable electrical voltage for forces about 7000 [N]. A few tests should be performed to ensure the potential of this sensor for forces higher than the above value.

- A preliminary machine learning analysis and results were provided in this thesis. In order to have a fully intelligent tire, it is necessary to have experimental data for several months of testing to cover all possible cases for tire forces. Then, the obtained data of those tests can be utilized for further training of the implemented neural network algorithm of this thesis. Furthermore, the obtained experimental data plus machine learning techniques can be used for other vehicle states.

- To have a more accurate comparison, both MFC sensors and Michigan Scientific transducer should be installed in the same tire. It is needed to develop a fully new rim for the smart tire, which can fit to Michigan Scientific transducer.

- An on-board circuit, which can be installed inside the tire, should be designed for both power harvesting and sending the data to the desired location. The harsh environment of tire should be taken into account for developing such circuit.

Bibliography

[1] H. Askari, Z. Saadatnia, A. Khajepour, M. B. Khamesee, J. Zu, A triboelectric self-powered sensor for tire condition monitoring: Concept, design, fabrication, and experiments, Advanced Engineering Materials 19 (12) (2017) 1700318.

[2] L. Gu, C. Livermore, Passive self-tuning energy harvester for extracting energy from rotational motion, Applied Physics Letters 97 (8) (2010) 081904.

[3] X. Xie, Q. Wang, N. Wu, A ring piezoelectric energy harvester excited by magnetic forces, International Journal of Engineering Science 77 (Supplement C) (2014) 71 – 78.

[4] Y.-J. Wang, C.-D. Chen, C.-C. Lin, J.-H. Yu, A nonlinear suspended energy harvester for a tire pressure monitoring system, Micromachines 6 (3) (2015) 312–327.

[5] G. Hatipoglu, H. Urey, Fr4-based electromagnetic energy harvester for wireless tyre sensor nodes, Procedia Chemistry 1 (1) (2009) 1211 – 1214, proceedings of the Eurosensors XXIII conference.

[6] D.-A. Wang, C.-Y. Chiu, H.-T. Pham, Electromagnetic energy harvesting from vibrations induced by kármán vortex street, Mechatronics 22 (6) (2012) 746–756.

[7] P. Li, S. Gao, H. Cai, Modeling and analysis of hybrid piezoelectric and electromagnetic energy harvesting from random vibrations, Microsystem Technologies 21 (2) (2015) 401–414.

[8] Y. Hu, C. Xu, Y. Zhang, L. Lin, R. L. Snyder, Z. L. Wang, A nanogenerator for energy harvesting from a rotating tire and its application as a self-powered pressure/speed sensor, Advanced Materials 23 (35) (2011) 4068–4071.

[9] Y. Mao, D. Geng, E. Liang, X. Wang, Single-electrode triboelectric nanogenerator for scavenging friction energy from rolling tires, Nano Energy 15 (2015) 227–234.

[10] J. Chen, H. Guo, G. Liu, X. Wang, Y. Xi, M. S. Javed, C. Hu, A fully-packaged and robust hybridized generator for harvesting vertical rotation energy in broad frequency band and building up self-powered wireless systems, Nano Energy 33 (Supplement C) (2017) 508 – 514.

[11] J. Qian, D.-S. Kim, D.-W. Lee, On-vehicle triboelectric nanogenerator enabled self-powered sensor for tire pressure monitoring, Nano Energy 49 (2018) 126 – 136.

[12] Y. Gao, Z. L. Wang, Electrostatic potential in a bent piezoelectric nanowire. the fundamental theory of nanogenerator and nanopiezotronics, Nano Letters 7 (8) (2007) 2499–2505.

[13] R. Matsuzaki, A. Todoroki, Wireless monitoring of automobile tires for intelligent tires, Sensors 8 (12) (2008) 8123–8138.

[14] A. E. Kubba, K. Jiang, A comprehensive study on technologies of tyre monitoring systems and possible energy solutions, Sensors 14 (6) (2014) 10306–10345.

[15] A. Consortium, et al., Intelligent tyre systems-state of the art and potential technologies, APOLLO Deliverable D7 for Project IST-2001-34372.

[16] R. Matsuzaki, A. Todoroki, Wireless flexible capacitive sensor based on ultra-flexible epoxy resin for strain measurement of automobile tires, Sensors and Actuators A: Physical 140 (1) (2007) 32–42.

[17] C. Bowen, M. Arafa, Energy harvesting technologies for tire pressure monitoring systems, Advanced Energy Materials 5 (7) (2015) 1401787.

[18] R. G. Longoria, R. Brushaber, A. Simms, An in-wheel sensor for monitoring tire-terrain interaction: Development and laboratory testing, Journal of Terramechanics 82 (2019) 43–52.

[19] M. Sergio, N. Manaresi, M. Tartagni, R. Canegallo, R. Guerrieri, On a road tire deformation measurement system using a capacitive–resistive sensor, Smart materials and structures 15 (6) (2006) 1700.

[20] R. Matsuzaki, A. Todoroki, Passive wireless strain monitoring of actual tire using capacitance resistance change and multiple spectral features, Sensors and Actuators A: Physical 126 (2) (2006) 277–286.

[21] D. Garcia-Pozuelo, O. Olatunbosun, S. Strano, M. Terzo, A real-time physical model for strain-based intelligent tires, Sensors and Actuators A: Physical 288 (2019) 1–9.

[22] H. Toplar, Experimental analysis of smart tires, Master's thesis, University of Waterloo, Waterloo, Canada (2014).

[23] J. Cullen, N. Arvanitis, J. Lucas, A. Al-Shammaa, In-field trials of a tyre pressure monitoring system based on segmented capacitance rings, Measurement 32 (3) (2002) 181–192.

[24] G. Breglio, A. Irace, L. Pugliese, M. Riccio, M. Russo, S. Strano, M. Terzo, Cost-effective wireless sensing system for an intelligent pneumatic tire, in: The International Conference of IFToMM Italy, Springer, 2018, pp. 158–164.

[25] J. Dakhlallah, S. Glaser, S. Mammar, Y. Sebsadji, Tire-road forces estimation using extended kalman filter and sideslip angle evaluation, in: American Control Conference, 2008, IEEE, 2008, pp. 4597–4602.

[26] G. Erdogan, L. Alexander, R. Rajamani, Estimation of tire-road friction coefficient using a novel wireless piezoelectric tire sensor, IEEE Sensors Journal 11 (2) (2011) 267–279.

[27] Y. Leng, D. Wenfeng, S. Peng, X. Ge, G. J. Nga, S. Liu, Study on electromagnetic wave propagation characteristics in rotating environments and its application in tire pressure monitoring, IEEE Transactions on Instrumentation and Measurement 61 (6) (2012) 1765–1777.

[28] O. Yilmazoglu, M. Brandt, J. Sigmund, E. Genc, H. Hartnagel, Integrated inas-gasb 3d magnetic field sensors for the intelligent tire, Sensors and Actuators A: Physical 94 (1) (2001) 59 – 63.

[29] R. Hinchet, W. Seung, S.-W. Kim, Recent progress on flexible triboelectric nanogenerators for self-powered electronics, ChemSusChem 8 (14) (2015) 2327–2344.

[30] M. Wang, Q. Wang, J. G. McDaniel, et al., Real-time wireless dynamic tire pressure sensor and energy harvesting system, US Patent 9, 315, 078 (Apr. 19 2016).

[31] A. C. Lesesky, S. B. DiMauro, Energy harvesting device, US Patent 8, 829, 696 (Sep. 9 2014).

[32] Z. Gao, M.-L. Sham, C. H. Chung, Piezoelectric module for energy harvesting, such as in a tire pressure monitoring system, US Patent 8, 011, 237 (Sep. 6 2011).

[33] Q. Yang, Y. Liu, C. Pan, J. Chen, X. Wen, Z. L. Wang, Largely enhanced efficiency in zno nanowire/p-polymer hybridized inorganic/organic ultraviolet light-emitting diode by piezo-phototronic effect, Nano Letters 13 (2) (2013) 607–613.

[34] A. Erturk, D. J. Inman, Piezoelectric energy harvesting, John Wiley & Sons, 2011.

[35] C. R. Bowen, V. Y. Topolov, H. A. Kim, Modern piezoelectric energy-harvesting materials, Vol. 238, Springer, 2016.

[36] R. Yu, C. Pan, J. Chen, G. Zhu, Z. L. Wang, Enhanced performance of a zno nanowire-based self-powered glucose sensor by piezotronic effect, Advanced Functional Materials 23 (47) (2013) 5868–5874.

[37] F. Khameneifar, S. Arzanpour, Energy harvesting from pneumatic tires using piezoelectric transducers, in: ASME Conference Proceedings of SMASIS, 2008, pp. 333–339.

[38] S. Sadeqi, S. Arzanpour, K. Hajikolaei, Broadening the frequency bandwidth of a tire-embedded piezoelectric-based energy harvesting system using coupled linear resonating structure, IEEE/ASME Transactions on Mechatronics 20 (5) (2015) 2085–2094.

[39] L. Pinna, M. Valle, G. M. Bo, Experimental results of piezoelectric bender generators for the energy supply of smart wireless sensors, in: Sensors And Microsystems, World Scientific, 2009, pp. 450–455.

[40] Q. Tang, X. Xia, X. Li, Non-contact frequency-up-conversion energy harvester for durable & broad-band automotive TPMS application, in: Micro Electro Mechanical Systems (MEMS), 2012 IEEE 25th International Conference on, IEEE, 2012, pp. 1273–1276.

[41] L. Wu, Y. Wang, C. Jia, C. Zhang, Battery-less piezoceramics mode energy harvesting for automobile TPMS, in: 2009 IEEE 8th International Conference on ASIC, IEEE, 2009, pp. 1205–1208.

[42] M. Keck, A new approach of a piezoelectric vibration-based power generator to supply next generation tire sensor systems, in: Sensors, 2007 IEEE, IEEE, 2007, pp. 1299–1302.

[43] Q. Zheng, H. Tu, A. Agee, Y. Xu, Vibration energy harvesting device based on asymmetric air-spaced cantilevers for tire pressure monitoring system, Proceedings of Power MEMS (2009) 403–406.

[44] L. Gu, C. Livermore, Compact passively self-tuning energy harvesting for rotating applications, Smart materials and structures 21 (1) (2011) 015002.

[45] L. Gu, Low-frequency piezoelectric energy harvesting prototype suitable for the mems implementation, Microelectronics Journal 42 (2) (2011) 277 – 282.

[46] L. Pinna, Vibration-based energy scavenging for power autonomous wireless sensor systems, School of Science and Technology for Information and Knowledge, Ph. D. Thesis, University of Genoa: Genoa, Italy (2010) 141.

[47] S. Roundy, J. Tola, Energy harvester for rotating environments using offset pendulum and nonlinear dynamics, Smart Materials and Structures 23 (10) (2014) 105004.

[48] K. B. Singh, V. Bedekar, S. Taheri, S. Priya, Piezoelectric vibration energy harvesting system with an adaptive frequency tuning mechanism for intelligent tires, Mechatronics 22 (7) (2012) 970 – 988.

[49] X. Xie, Q. Wang, A mathematical model for piezoelectric ring energy harvesting technology from vehicle tires, International Journal of Engineering Science 94 (Supplement C) (2015) 113 – 127.

[50] N. Makki, R. Pop-Iliev, Battery-and wire-less tire pressure measurement systems (TPMS) sensor, Microsystem technologies 18 (7-8) (2012) 1201–1212.

[51] J. Lee, B. Choi, Development of a piezoelectric energy harvesting system for implementing wireless sensors on the tires, Energy Conversion and Management 78 (2014) 32–38.

[52] Y. Zhang, R. Zheng, K. Shimono, T. Kaizuka, K. Nakano, Effectiveness testing of a piezoelectric energy harvester for an automobile wheel using stochastic resonance, Sensors 16 (10) (2016) 1727.

[53] J. Bastiaan, Design of a smart tire sensor system, Ph.D. thesis, University of Waterloo, Waterloo, Canada (2015).

[54] Z. Lin, J. Chen, X. Li, J. Li, J. Liu, Q. Awais, J. Yang, Broadband and three-dimensional vibration energy harvesting by a non-linear magnetoelectric generator, Applied Physics Letters 109 (25) (2016) 253903.

[55] B. Zhang, J. Chen, L. Jin, W. Deng, L. Zhang, H. Zhang, M. Zhu, W. Yang, Z. L. Wang, Rotating-disk-based hybridized electromagnetic–triboelectric nanogenerator

for sustainably powering wireless traffic volume sensors, ACS Nano 10 (6) (2016) 6241–6247.

[56] E. Asadi, H. Askari, M. B. Khamesee, A. Khajepour, High frequency nano electromagnetic self-powered sensor: Concept, modelling and analysis, Measurement 107 (Supplement C) (2017) 31 – 40.

[57] S. J. Roundy, Energy scavenging for wireless sensor nodes with a focus on vibration to electricity conversion, Ph.D. thesis, University of California, Berkeley Berkeley, CA (2003).

[58] B. Mann, N. Sims, On the performance and resonant frequency of electromagnetic induction energy harvesters, Journal of Sound and Vibration 329 (9) (2010) 1348–1361.

[59] D. Spreemann, Y. Manoli, Electromagnetic vibration energy harvesting devices: Architectures, design, modeling and optimization, Vol. 35, Springer Science & Business Media, 2012.

[60] S. H. Choi, D. P. Chun, D. H. Kwon, S. K. Kim, H. K. Na, W. J. Lee, Power supply using static magnetic field of tire pressure monitoring system, US Patent 7,541,916 (Jun. 2 2009).

[61] S. Lee, D.-H. Kim, Durable and sustainable strap type electromagnetic harvester for tire pressure monitoring system, Journal of Magnetics 18 (4) (2013) 473–480.

[62] S. Tornincasa, M. Repetto, E. Bonisoli, F. Di Monaco, Energy harvester for vehicle tires: Nonlinear dynamics and experimental outcomes, Journal of Intelligent Material Systems and Structures 23 (1) (2012) 3–13.

[63] D. Younesian, H. Askari, Z. Saadatnia, M. KalamiYazdi, Analytical approximate solutions for the generalized nonlinear oscillator, Applicable Analysis 91 (5) (2012) 965–977.

[64] M. Daeichin, M. Ahmadpoor, H. Askari, A. Yildirim, Rational energy balance method to nonlinear oscillators with cubic term, Asian-European Journal of Mathematics 6 (02) (2013) 1350019.

[65] L. Cveticanin, M. KalamiYazdi, H. Askari, Z. Saadatnia, Vibration of a two-mass system with non-integer order nonlinear connection, Mechanics Research Communications 43 (2012) 22–28.

[66] D. Younesian, E. Esmailzadeh, H. Askari, Vibration analysis of oscillators with generalized inertial and geometrical nonlinearities, in: Nonlinear Approaches in Engineering Applications, Springer, 2018, pp. 147–166.

[67] G. Hatipoglu, H. Ürey, Fr4-based electromagnetic energy harvester for wireless sensor nodes, Smart Materials and Structures 19 (1) (2009) 015022.

[68] X. Tang, L. Zuo, Vibration energy harvesting from random force and motion excitations, Smart Materials and Structures 21 (7) (2012) 075025.

[69] Y. J. Wang, C. D. Chen, C. K. Sung, Design of a frequency-adjusting device for harvesting energy from a rotating wheel, Sensors and Actuators A: Physical 159 (2) (2010) 196 – 203.

[70] Y. Wang, C. Chen, C. Sung, System design of a weighted-pendulum-type electromagnetic generator for harvesting energy from a rotating wheel, IEEE/ASME Transactions on Mechatronics 18 (2) (2013) 754–763.

[71] Z. L. Wang, J. Song, Piezoelectric nanogenerators based on zinc oxide nanowire arrays, Science 312 (5771) (2006) 242–246.

[72] Y. Zi, Z. L. Wang, Nanogenerators: An emerging technology towards nanoenergy, APL Materials 5 (7) (2017) 074103.

[73] Z. L. Wang, T. Jiang, L. Xu, Toward the blue energy dream by triboelectric nanogenerator networks, Nano Energy 39 (2017) 9 – 23.

[74] Y. Xi, H. Guo, Y. Zi, X. Li, J. Wang, J. Deng, S. Li, C. Hu, X. Cao, Z. L. Wang, Multifunctional TENG for blue energy scavenging and self-powered wind-speed sensor, Advanced Energy Materials 7 (12) (2017) 1602397.

[75] Z. Saadatnia, E. Asadi, H. Askari, J. Zu, E. Esmailzadeh, Modeling and performance analysis of duck-shaped triboelectric and electromagnetic generators for water wave energy harvesting, International Journal of Energy Research 41 (14) (2017) 2392–2404.

[76] J. Chen, G. Zhu, W. Yang, Q. Jing, P. Bai, Y. Yang, T.-C. Hou, Z. L. Wang, Harmonic-resonator-based triboelectric nanogenerator as a sustainable power source and a self-powered active vibration sensor, Advanced Materials 25 (42) (2013) 6094–6099.

[77] W. Yang, J. Chen, Q. Jing, J. Yang, X. Wen, Y. Su, G. Zhu, P. Bai, Z. L. Wang, 3d stack integrated triboelectric nanogenerator for harvesting vibration energy, Advanced Functional Materials 24 (26) (2014) 4090–4096.

[78] A. Ahmed, I. Hassan, M. Hedaya, T. A. El-Yazid, J. Zu, Z. L. Wang, Farms of triboelectric nanogenerators for harvesting wind energy: A potential approach towards green energy, Nano Energy 36 (Supplement C) (2017) 21 – 29.

[79] L. Zhang, B. Zhang, J. Chen, L. Jin, W. Deng, J. Tang, H. Zhang, H. Pan, M. Zhu, W. Yang, et al., Lawn structured triboelectric nanogenerators for scavenging sweeping wind energy on rooftops, Advanced Materials 28 (8) (2016) 1650–1656.

[80] Y. Yang, G. Zhu, H. Zhang, J. Chen, X. Zhong, Z.-H. Lin, Y. Su, P. Bai, X. Wen, Z. L. Wang, Triboelectric nanogenerator for harvesting wind energy and as self-powered wind vector sensor system, ACS Nano 7 (10) (2013) 9461–9468.

[81] H. Askari, E. Asadi, Z. Saadatnia, A. Khajepour, M. B. Khamesee, J. Zu, A hybridized electromagnetic-triboelectric self-powered sensor for traffic monitoring: concept, modelling, and optimization, Nano Energy 32 (Supplement C) (2017) 105 – 116.

[82] R. Liu, X. Kuang, J. Deng, Y.-C. Wang, A. C. Wang, W. Ding, Y.-C. Lai, J. Chen, P. Wang, Z. Lin, et al., Shape memory polymers for body motion energy harvesting and self-powered mechanosensing, Advanced Materials (2018) 1705195.

[83] N. Zhang, J. Chen, Y. Huang, W. Guo, J. Yang, J. Du, X. Fan, C. Tao, A wearable all-solid photovoltaic textile, Advanced Materials 28 (2) (2016) 263–269.

[84] J. Chen, Y. Huang, N. Zhang, H. Zou, R. Liu, C. Tao, X. Fan, Z. L. Wang, Microcable structured textile for simultaneously harvesting solar and mechanical energy, Nature Energy 1 (10) (2016) 16138.

[85] L. Jin, J. Chen, B. Zhang, W. Deng, L. Zhang, H. Zhang, X. Huang, M. Zhu, W. Yang, Z. L. Wang, Self-powered safety helmet based on hybridized nanogenerator for emergency, ACS Nano 10 (8) (2016) 7874–7881.

[86] W. Yang, J. Chen, G. Zhu, J. Yang, P. Bai, Y. Su, Q. Jing, X. Cao, Z. L. Wang, Harvesting energy from the natural vibration of human walking, ACS Nano 7 (12) (2013) 11317–11324.

[87] Z. Wang, Piezotronics and Piezo-Phototronics, Microtechnology and MEMS, Springer Berlin Heidelberg, 2013.

[88] S. Xu, Y. Qin, C. Xu, Y. Wei, R. Yang, Z. L. Wang, Self-powered nanowire devices, Nature Nanotechnology 5 (5) (2010) 366.

[89] Z. L. Wang, J. Chen, L. Lin, Progress in triboelectric nanogenerators as a new energy technology and self-powered sensors, Energy & Environmental Science 8 (8) (2015) 2250–2282.

[90] J. Chen, Z. L. Wang, Reviving vibration energy harvesting and self-powered sensing by a triboelectric nanogenerator, Joule 1 (3) (2017) 480 – 521.

[91] G. Zhu, J. Chen, T. Zhang, Q. Jing, Z. L. Wang, Radial-arrayed rotary electrification for high performance triboelectric generator, Nature Communications 5 (2014) 3426.

[92] S. Wang, Z. L. Wang, Y. Yang, A one-structure-based hybridized nanogenerator for scavenging mechanical and thermal energies by triboelectric–piezoelectric–pyroelectric effects, Advanced Materials 28 (15) (2016) 2881–2887.

[93] Y. Yang, S. Wang, Y. Zhang, Z. L. Wang, Pyroelectric nanogenerators for driving wireless sensors, Nano Letters 12 (12) (2012) 6408–6413.

[94] Z. Wang, L. Lin, J. Chen, S. Niu, Y. Zi, Triboelectric Nanogenerators, Green Energy and Technology, Springer International Publishing, 2016.

[95] N. Zhang, C. Tao, X. Fan, J. Chen, Progress in triboelectric nanogenerators as self-powered smart sensors, Journal of Materials Research 32 (9) (2017) 1628–1646.

[96] Y. Hu, J. Yang, Q. Jing, S. Niu, W. Wu, Z. L. Wang, Triboelectric nanogenerator built on suspended 3d spiral structure as vibration and positioning sensor and wave energy harvester, ACS Nano 7 (11) (2013) 10424–10432.

[97] J. Yang, J. Chen, Y. Liu, W. Yang, Y. Su, Z. L. Wang, Triboelectrification-based organic film nanogenerator for acoustic energy harvesting and self-powered active acoustic sensing, ACS Nano 8 (3) (2014) 2649–2657.

[98] X. Fan, J. Chen, J. Yang, P. Bai, Z. Li, Z. L. Wang, Ultrathin, rollable, paper-based triboelectric nanogenerator for acoustic energy harvesting and self-powered sound recording, ACS Nano 9 (4) (2015) 4236–4243.

[99] Z. Lin, J. Yang, X. Li, Y. Wu, W. Wei, J. Liu, J. Chen, J. Yang, Large-scale and washable smart textiles based on triboelectric nanogenerator arrays for self-powered sleeping monitoring, Advanced Functional Materials 28 (1) (2018) 1704112.

[100] Y. Zi, L. Lin, J. Wang, S. Wang, J. Chen, X. Fan, P.-K. Yang, F. Yi, Z. L. Wang, Triboelectric–pyroelectric–piezoelectric hybrid cell for high-efficiency energy-harvesting and self-powered sensing, Advanced Materials 27 (14) (2015) 2340–2347.

[101] E. R. Westby, E. Halvorsen, Design and modeling of a patterned-electret-based energy harvester for tire pressure monitoring systems, IEEE/ASME Transactions On Mechatronics 17 (5) (2012) 995–1005.

[102] M. O. F. Emon, J.-W. Choi, Flexible piezoresistive sensors embedded in 3d printed tires, Sensors 17 (3) (2017) 656.

[103] F. Coppo, G. Pepe, N. Roveri, A. Carcaterra, A multisensing setup for the intelligent tire monitoring, Sensors 17 (3) (2017) 576.

[104] H. Guo, Z. Yin, D. Cao, H. Chen, C. Lv, A review of estimation for vehicle tire-road interactions toward automated driving, IEEE Transactions on Systems, Man, and Cybernetics: Systems (99) (2018) 1–17.

[105] A. Farhat, D. Koenig, D. Hernandez-Alcantara, R. Morales-Menendez, Tire force estimation using a proportional integral observer, in: Journal of Physics: Conference Series, Vol. 783, IOP Publishing, 2017, p. 012014.

[106] Y.-H. J. Hsu, Estimation and control of lateral tire forces using steering torque, Ph.D. thesis, Stanford University, Stanford, California, USA (2009).

[107] M. Doumiati, A. C. Victorino, A. Charara, D. Lechner, Onboard real-time estimation of vehicle lateral tire–road forces and sideslip angle, IEEE/ASME Transactions on Mechatronics 16 (4) (2011) 601–614.

[108] K. Nam, S. Oh, H. Fujimoto, Y. Hori, Estimation of sideslip and roll angles of electric vehicles using lateral tire force sensors through RLS and Kalman filter approaches, IEEE Transactions on Industrial Electronics 60 (3) (2013) 988–1000.

[109] A. Albinsson, F. Bruzelius, M. Jonasson, B. Jacobson, Tire force estimation utilizing wheel torque measurements and validation in simulations and experiments, in: 12th International Symposium on Advanced Vehicle Control (AVEC'14), Tokyo Japan, 2014, pp. 294–299.

[110] G. Baffet, A. Charara, D. Lechner, Estimation of vehicle sideslip, tire force and wheel cornering stiffness, Control Engineering Practice 17 (11) (2009) 1255–1264.

[111] R. Rajamani, G. Phanomchoeng, D. Piyabongkarn, J. Y. Lew, Algorithms for real-time estimation of individual wheel tire-road friction coefficients, Mechatronics, IEEE/ASME Transactions on 17 (6) (2012) 1183–1195.

[112] J. Yu, J. Chen, Y. Peng, H. Liu, Nonlinear observer for longitudinal and lateral velocities of vehicles based on the estimation of longitudinal tire forces, in: American Control Conference (ACC), 2016, pp. 6887–6892.

[113] J. V. Alcantar, F. Assadian, Longitudinal tire force estimation using youla controller output observer, IEEE Control Systems Letters 2 (1) (2018) 31–36.

[114] Y. Wang, D. M. Bevly, S.-k. Chen, Longitudinal tire force estimation with unknown input observer, in: ASME 2012 5th Annual Dynamic Systems and Control Conference joint with the JSME 2012 11th Motion and Vibration Conference, American Society of Mechanical Engineers, 2012, pp. 523–530.

[115] Y. Wang, D. M. Bevly, S.-k. Chen, Lateral tire force estimation with unknown input observer, in: ASME 2012 5th Annual Dynamic Systems and Control Conference joint with the JSME 2012 11th Motion and Vibration Conference, American Society of Mechanical Engineers, 2012, pp. 531–538.

[116] W. Cho, J. Yoon, S. Yim, B. Koo, K. Yi, Estimation of tire forces for application to vehicle stability control, Vehicular Technology, IEEE Transactions on 59 (2) (2010) 638–649.

[117] F. Sun, K. Lolenko, J. Rudolph, Nonlinear observer design for state estimation during antilock braking, Proceedings of the Institution of Mechanical Engineers, Part I: Journal of Systems and Control Engineering 228 (2) (2014) 78–86.

[118] M. Doumiati, A. Victorino, D. Lechner, G. Baffet, A. Charara, Observers for vehicle tyre/road forces estimation: experimental validation, Vehicle System Dynamics 48 (11) (2010) 1345–1378.

[119] R. A. Cordeiro, A. C. Victorino, P. A. Ferreira, E. C. de Paiva, S. S. Bueno, Tire-ground forces estimation in a 4-wheel vehicle using a delayed interconnected cascade-observer structure, IFAC 49 (15) (2016) 139–144.

[120] S. Muller, M. Uchanski, K. Hedrick, Estimation of the maximum tire-road friction coefficient, Journal of Dynamic Systems, Measurement, and Control 125 (4) (2003) 607–617.

[121] L. Alvarez, J. Yi, R. Horowitz, L. Olmos, Dynamic friction model-based tire-road friction estimation and emergency braking control, Journal of Dynamic Systems, Measurement, and Control 127 (1) (2005) 22–32.

[122] Y. Peng, J. Chen, J. Yu, Y. Ma, H. Zheng, Nonlinear observer for vehicle velocity and tire-road friction coefficient estimation, in: American Control Conference (ACC), 2017, IEEE, 2017, pp. 2606–2611.

[123] J. Rath, K. C. Veluvolu, M. Defoort, Simultaneous estimation of road profile and tire road friction for automotive vehicle, IEEE Transactions on Vehicular Technology 64 (10) (2015) 4461–4471.

[124] N. Patel, C. Edwards, S. Spurgeon, Tyreroad friction estimationa comparative study, Proceedings of the Institution of Mechanical Engineers, Part D: Journal of Automobile Engineering 222 (12) (2008) 2337–2351.

[125] J. Yi, L. Alvarez, R. Horowitz, Adaptive emergency braking control with underestimation of friction coefficient, Control Systems Technology, IEEE Transactions on 10 (3) (2002) 381–392.

[126] C. Lee, K. Hedrick, K. Yi, Real-time slip-based estimation of maximum tire-road friction coefficient, IEEE/ASME Transactions on Mechatronics 9 (2) (2004) 454–458.

[127] R. Ghandour, A. Victorino, M. Doumiati, A. Charara, Tire/road friction coefficient estimation applied to road safety, in: Control & Automation (MED), 2010 18th Mediterranean Conference on, IEEE, 2010, pp. 1485–1490.

[128] J. Villagra, B. DAndréa-Novel, M. Fliess, H. Mounier, A diagnosis-based approach for tire–road forces and maximum friction estimation, Control Engineering Practice 19 (2) (2011) 174–184.

[129] F. Gustafsson, Slip-based tire-road friction estimation, Automatica 33 (6) (1997) 1087–1099.

[130] K. Yi, K. Hedrick, S.-C. Lee, Estimation of tire-road friction using observer based identifiers, Vehicle System Dynamics 31 (4) (1999) 233–261.

[131] J. Wang, L. Alexander, R. Rajamani, Friction estimation on highway vehicles using longitudinal measurements, Journal of Dynamic Systems, Measurement, and Control 126 (2) (2004) 265–275.

[132] M. Choi, J. J. Oh, S. B. Choi, Linearized recursive least squares methods for real-time identification of tire–road friction coefficient, IEEE Transactions on Vehicular Technology 62 (7) (2013) 2906–2918.

[133] K. Nam, Application of novel lateral tire force sensors to vehicle parameter estimation of electric vehicles, Sensors 15 (11) (2015) 28385–28401.

[134] L. Chen, M. Bian, Y. Luo, Z. Qin, K. Li, Tire–road friction coefficient estimation based on the resonance frequency of in-wheel motor drive system, Vehicle System Dynamics 54 (1) (2016) 1–19.

[135] K. Han, E. Lee, M. Choi, S. B. Choi, Adaptive scheme for the real-time estimation of tire-road friction coefficient and vehicle velocity, IEEE/ASME Transactions on Mechatronics 22 (4) (2017) 1508–1518.

[136] Y.-H. J. Hsu, S. M. Laws, J. C. Gerdes, Estimation of tire slip angle and friction limits using steering torque, IEEE Transactions on Control Systems Technology 18 (4) (2010) 896–907.

[137] C. Ahn, H. Peng, H. E. Tseng, Robust estimation of road frictional coefficient, IEEE Transactions on Control Systems Technology 21 (1) (2013) 1–13.

[138] G. Baffet, A. Charara, G. Dherbomez, An observer of tire-road forces and friction for active security vehicle systems, Mechatronics, IEEE/ASME Transactions on 12 (6) (2007) 651–661.

[139] L. R. Ray, Nonlinear tire force estimation and road friction identification: Simulation and experiments, Automatica 33 (10) (1997) 1819–1833.

[140] A. E. Kubba, M. Behroozi, O. A. Olatunbosun, C. Anthony, K. Jiang, Modeling of strain energy harvesting in pneumatic tires using piezoelectric transducer, Tire Science And Technology 42 (1) (2014) 16–34.

[141] D. Van den Ende, H. Van de Wiel, W. Groen, S. Van der Zwaag, Direct strain energy harvesting in automobile tires using piezoelectric PZT–polymer composites, Smart materials and structures 21 (1) (2011) 015011.

[142] J. Lee, J. Oh, H. Kim, B. Choi, Strain-based piezoelectric energy harvesting for wireless sensor systems in a tire, Journal of Intelligent Material Systems and Structures 26 (11) (2015) 1404–1416.

[143] D. A. Wang, H. T. Pham, C. W. Chao, J. M. Chen, A piezoelectric energy harvester based on pressure fluctuations in karman vortex street, in: World Renewable Energy Congress, 2011, Ping, Sweden, Linköping University Electronic Press, 2011, pp. 1456–1463.

[144] P. D. Mitcheson, E. M. Yeatman, G. K. Rao, A. S. Holmes, T. C. Green, Energy harvesting from human and machine motion for wireless electronic devices, Proceedings of the IEEE 96 (9) (2008) 1457–1486.

[145] C. X. Lu, C. B. Han, G. Q. Gu, J. Chen, Z. W. Yang, T. Jiang, C. He, Z. L. Wang, Temperature effect on performance of triboelectric nanogenerator, Advanced Engineering Materials 19 (12) (2017) 1700275.

[146] C. Xu, Y. Zi, A. C. Wang, H. Zou, Y. Dai, X. He, P. Wang, Y.-C. Wang, P. Feng, D. Li, et al., On the electron-transfer mechanism in the contact-electrification effect, Advanced Materials 30 (15) (2018) 1706790.

[147] J. C. Maxwell, Viii. a dynamical theory of the electromagnetic field, Philosophical Transactions of the Royal Society of London 155 (1865) 459–512.

[148] Z. L. Wang, On Maxwell's displacement current for energy and sensors: the origin of nanogenerators, Materials Today 20 (2) (2017) 74 – 82.

[149] M. J. Caruso, L. S. Withanawasam, Vehicle detection and compass applications using AMR magnetic sensors, in: Sensors Expo Proceedings, Vol. 477, 1999, p. 39.

[150] C. Treutler, Magnetic sensors for automotive applications, Sensors and Actuators A: Physical 91 (1-2) (2001) 2–6.

[151] D. L. Striker, R. J. Hampo, Method of position sensing utilizing giant magneto resistance elements and solid state switch array, US Patent 5, 929, 631 (Jul. 27 1999).

[152] D. Nachtigal, G. Bergmann, Multi-pole magnetic encoders for active speed-measurement systems, Tech. rep., SAE Technical Paper (1999).

[153] T. Wang, Z. Jiao, L. Yan, Design and comparative study of dual magnet array for linear load simulation system, in: Vehicle Power and Propulsion Conference (VPPC), 2016 IEEE, IEEE, 2016, pp. 1–5.

[154] K. Mohri, Review on recent advances in the field of amorphous-metal sensors and transducers, IEEE Transactions on Magnetics 20 (5) (1984) 942–947.

[155] G. R. Kohut, J. Y. Yoon, M. D. Murphy, D. L. Hartley, D. B. Purdie, Seat belt tension sensor, US Patent 6, 554, 318 (Apr. 29 2003).

[156] Z. L. Wang, Triboelectric nanogenerators as new energy technology for self-powered systems and as active mechanical and chemical sensors, ACS Nano 7 (11) (2013) 9533–9557.

[157] F. R. Fan, W. Tang, Z. L. Wang, Flexible nanogenerators for energy harvesting and self-powered electronics, Advanced Materials 28 (22) (2016) 4283–4305.

[158] H. Guo, Z. Wen, Y. Zi, M.-H. Yeh, J. Wang, L. Zhu, C. Hu, Z. L. Wang, A waterproof triboelectric–electromagnetic hybrid generator for energy harvesting in harsh environments, Advanced Energy Materials 6 (6) (2016) 1501593.

[159] S. Niu, Z. L. Wang, Theoretical systems of triboelectric nanogenerators, Nano Energy 14 (2015) 161–192.

[160] H. Askari, Z. Saadatnia, E. Asadi, A. Khajepour, M. B. Khamesee, J. Zu, A flexible hybridized electromagnetic-triboelectric multi-purpose self-powered sensor, Nano Energy 45 (2018) 319–329.

[161] Z. Saadatnia, E. Asadi, H. Askari, E. Esmailzadeh, H. E. Naguib, A heaving point absorber-based triboelectric-electromagnetic wave energy harvester: An efficient approach toward blue energy, International Journal of Energy Research 42 (7) (2018) 2431–2447.

[162] Y. Bian, T. Jiang, T. Xiao, W. Gong, X. Cao, Z. Wang, Z. L. Wang, Triboelectric nanogenerator tree for harvesting wind energy and illuminating in subway tunnel, Advanced Materials Technologies 3 (3) (2018) 1700317.

[163] H. Askari, E. Hashemi, A. Khajepour, M. B. Khamesee, Z. L. Wang, Tire condition monitoring and intelligent tires using nanogenerators based on piezoelectric, electromagnetic, and triboelectric effects, Advanced Materials Technologies 4 (1) (2019) 1800105.

[164] H. Askari, E. Hashemi, A. Khajepour, M. B. Khamesee, Z. L. Wang, Towards self-powered sensing using nanogenerators for automotive systems, Nano energy 53 (2018) 1003–1019.

[165] H. Askari, A. Khajepour, M. B. Khamesee, Z. Saadatnia, Z. L. Wang, Piezoelectric and triboelectric nanogenerators: Trends and impacts, Nano Today 22 (2018) 10–13.

[166] S. Wang, L. Lin, Z. L. Wang, Triboelectric nanogenerators as self-powered active sensors, Nano Energy 11 (2015) 436–462.

[167] X. Wang, Piezoelectric nanogeneratorsharvesting ambient mechanical energy at the nanometer scale, Nano Energy 1 (1) (2012) 13–24.

[168] B. Kumar, S.-W. Kim, Energy harvesting based on semiconducting piezoelectric zno nanostructures, Nano Energy 1 (3) (2012) 342–355.

[169] S. Niu, Y. Liu, S. Wang, L. Lin, Y. S. Zhou, Y. Hu, Z. L. Wang, Theoretical investigation and structural optimization of single-electrode triboelectric nanogenerators, Advanced Functional Materials 24 (22) (2014) 3332–3340.

[170] P. M. Hergenrother, The use, design, synthesis, and properties of high performance/high temperature polymers: An overview, High Performance Polymers 15 (1) (2003) 3–45.

[171] C. Prisacariu, Polyurethane Elastomers: From Morphology to Mechanical Aspects, SpringerLink : Bücher, Springer Vienna, 2011.

[172] Z. Quan, C. Han, T. Jiang, Z. Wang, Robust thin films-based triboelectric nanogenerator arrays for harvesting bidirectional wind energy, Advanced Energy Materials 6(2016) (5).

[173] L. Xu, Y. Pang, C. Zhang, T. Jiang, X. Chen, J. Luo, W. Tang, X. Cao, Z. L. Wang, Integrated triboelectric nanogenerator array based on air-driven membrane structures for water wave energy harvesting, Nano Energy 31 (2017) 351 – 358.

[174] K. Zhang, X. Wang, Y. Yang, Z. L. Wang, Hybridized electromagnetictriboelectric nanogenerator for scavenging biomechanical energy for sustainably powering wearable electronics, ACS Nano 9 (4) (2015) 3521–3529.

[175] K. Zhang, Y. Yang, Linear-grating hybridized electromagnetic-triboelectric nanogenerator for sustainably powering portable electronics, Nano Research 9 (4) (2016) 974–984.

[176] R. Cao, T. Zhou, B. Wang, Y. Yin, Z. Yuan, C. Li, Z. L. Wang, Rotating-sleeve triboelectricelectromagnetic hybrid nanogenerator for high efficiency of harvesting mechanical energy, ACS Nano 11 (8) (2017) 8370–8378.

[177] N. L. Silva, L. Gonçalves, H. Carvalho, Deposition of conductive materials on textile and polymeric flexible substrates, Journal of Materials Science: Materials in Electronics 24 (2) (2013) 635–643.

[178] T. P. Daue, J. Kunzmann, A. Schönecker, Energy harvesting systems using piezoelectric macro fiber composites, in: IEEE International Symposium on Electrets (ISE13), paper, Vol. 27, 2008.

[179] S. Haykin, Neural Networks, Vol. 2, Prentice Hall, New York, 1994.

[180] S. Fritsch, F. Guenther, Package neuralnet, 2019.

[181] A. D. Anastasiadis, G. D. Magoulas, M. N. Vrahatis, New globally convergent training scheme based on the resilient propagation algorithm, Neurocomputing 64 (2005) 253–270.

[182] P. E. Gill, W. Murray, M. H. Wright, Practical optimization, Academic Press, The University of Michigan, USA, 1981.

[183] M. T. Hagan, M. B. Menhaj, Training feedforward networks with the marquardt algorithm, IEEE transactions on Neural Networks 5 (6) (1994) 989–993.

[184] M. F. Møller, A scaled conjugate gradient algorithm for fast supervised learning, Neural Networks 6 (4) (1993) 525–533.

[185] D. E. Rumelhart, Parallel distributed processing: Explorations in the microstructure of cognition, Learning Internal Representations by Error Propagation 1 (1986) 318–362.

[186] M. Riedmiller, H. Braun, A direct adaptive method for faster backpropagation learning: The rprop algorithm, in: Proceedings of the IEEE international conference on neural networks, Vol. 1993, San Francisco, 1993, pp. 586–591.

APPENDICES

Appendix A

Electromagnetic Principal Equations

The following set of equations, known as Maxwell's equation, are the basis of many different technologies varying from macro- to nano-systems:

$$\nabla \times H = J + \frac{\partial D}{\partial t}, \tag{A.1}$$

$$\nabla \cdot B = 0, \tag{A.2}$$

$$\nabla \times E = -\frac{\partial B}{\partial t}, \tag{A.3}$$

$$\nabla \cdot D = \rho, \tag{A.4}$$

in which J $[\frac{A}{m^2}]$ and $\rho[\frac{C}{m^3}]$ are the current and electric charge density, H (magnetic field strength $[\frac{A}{m}]$), B (magnetic flux density T), E (electric field $[\frac{V}{m}]$), and D (Electric flux density $\frac{C}{m^3}$). The system of equations consists 12 unknown field components. In order to have a complete form for theory of field equations, the following constitutive equations should be considered:

$$B = \mu_0(H + M), \tag{A.5}$$

$$D = \varepsilon_0 E + P, \tag{A.6}$$

and

$$J = \sigma E, \tag{A.7}$$

where $P[\frac{C}{m^2}]$ is the polarization, $\mu_0 = 4\pi \times 10^7[\frac{T.m}{A}]$ is the permeability, $M[A/m]$ is the magnetization, and $\sigma(A/Vm)$ is the conductivity. The following forms can be also considered for Eq. (A.1) to Eq. (A.3) by taking the surface integral of the curl and applying the Stoke's theorem to the left hand side. Furthermore, divergence of Eq. (A.2) to Eq. (A.4) is integrated, and then the divergence theorem is applied to the left-hand side.

$$\int_c H\, dl = \int_s (J + \frac{\partial D}{\partial t})\, ds, \tag{A.8}$$

$$\int_c E\, dl = \int_s \frac{\partial B}{\partial t}\, ds, \tag{A.9}$$

$$\int_s B\, ds = 0, \tag{A.10}$$

$$\oint_s D\, ds = \int_\Gamma \rho\, d\Gamma, \tag{A.11}$$

Eq. (A.8) represents the general form of Ampere's law, and Faraday's law is formulated in Eq. (A.9). Eq. (A.10) shows that the outward flux over a closed surface is zero, i.e., there are no magnetic monopoles (isolated sinks or sources). The Gausss law is described by Eq. (A.11), and it is concluded from it that the total outward electric flux over a closed surface equals the free charges enclosed by the surface.

Appendix B

Thermal Durability Test

In order to asses the thermal durability of the Flexible Sensor II, series of tests were conducted with the implementation of experimental setup 2, YIHUA 858D SMD rework station, (Figure C.1(a)), as the heat gun, and HHM290 TrueRMS Supermeter , (Figure C.1(b)).


(a) (b)

Figure B.1: (a) YIHUA 858D SMD rework station (b) HHM290 TrueRMS Supermeter

While the sensor was attached to the sidewall of the tire and was tested with the experimental setup 2, using the heat gun, heating load is applied to the sensor, and at the same time, temperature is measured on the top surface of the sensor by using Supermeter-Infrared temperature sensor. The output voltage of the sensor was measured while an external resistive load of $10M\Omega$ is shunted to the sensor, considering temperature variation.

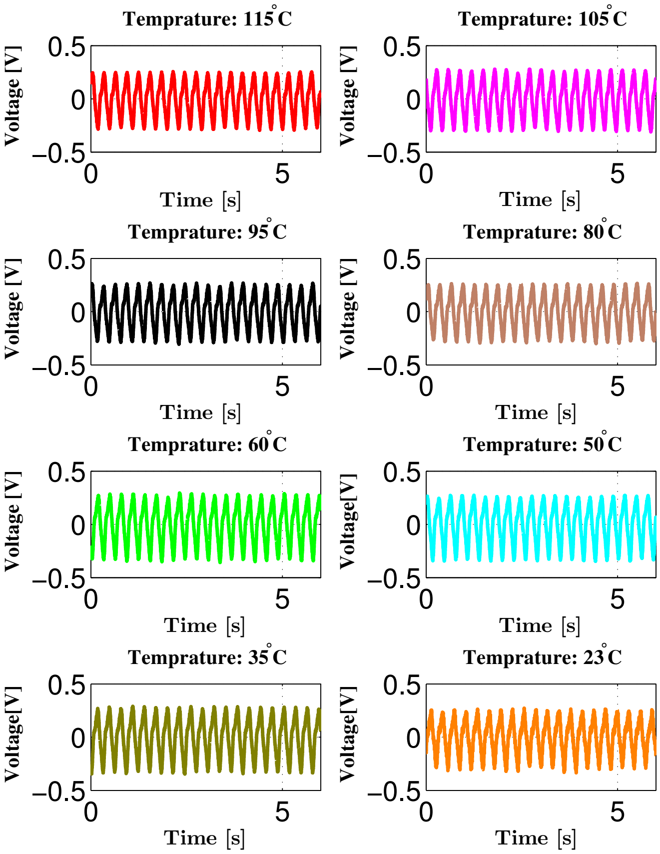

Figure B.2: The effect of temperature on the sensor output voltage

As the figure shows, sensor output voltage has shown a consistent behavior between temperature range of 23 to 115 degrees of Centigrade. This shows the potential of the sensor for working in a wide temperature range.

Appendix C

Specification of MFC Sensors

The following images shows our selected MFC sensors for tire condition monitoring system.

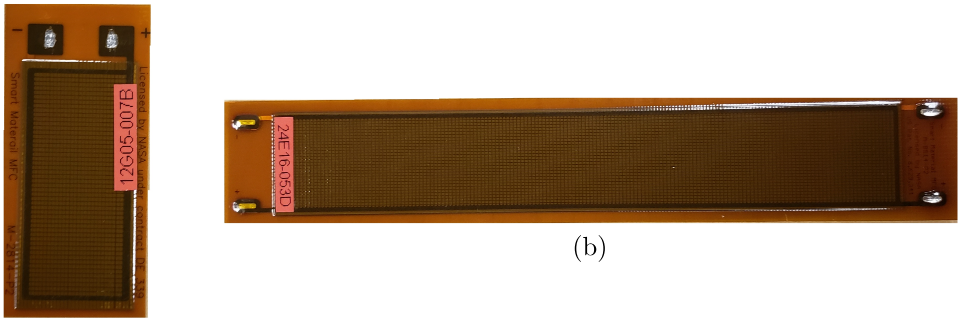
(a)

(b)

Figure C.1: (a) MFC-HT-P2-small size (b) MFC-HT-P2-large size

The specifications of the above sensors are provided in Table C.1.

Table C.1: Types of the used MFC sensors

Type	**Effective Area**	**Overall Area**	**Capacitance**(nF)
M8514P2-HT	1190 mm^2	1800 mm^2	84.04
M2814P2-HT	392 mm^2	666 mm^2	30.78